JEOL news
Volume 38 number 2, 2003
ISSN 0385-4426

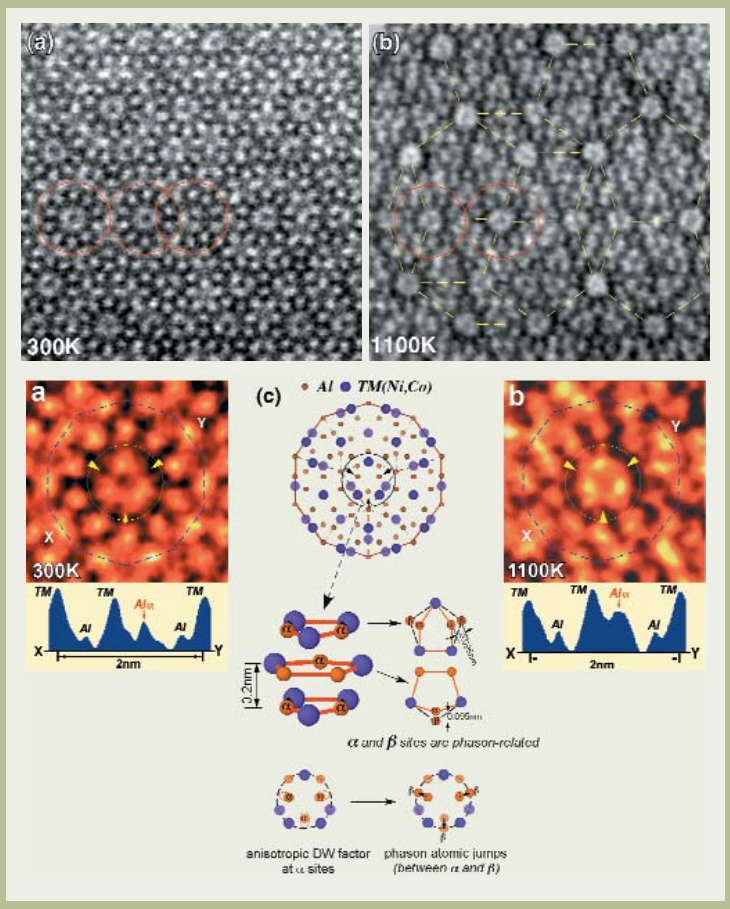

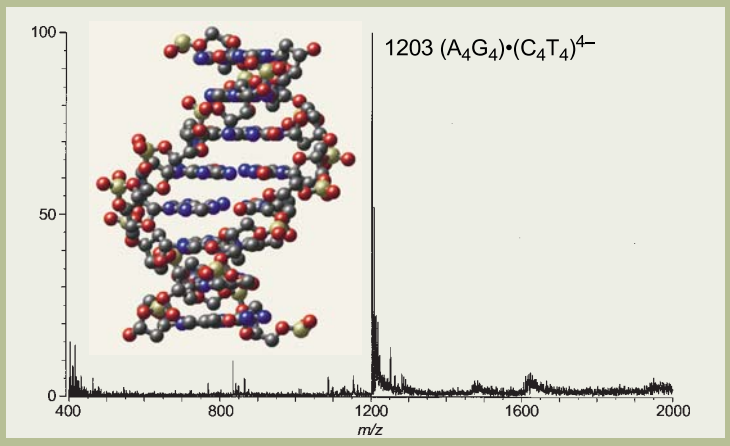

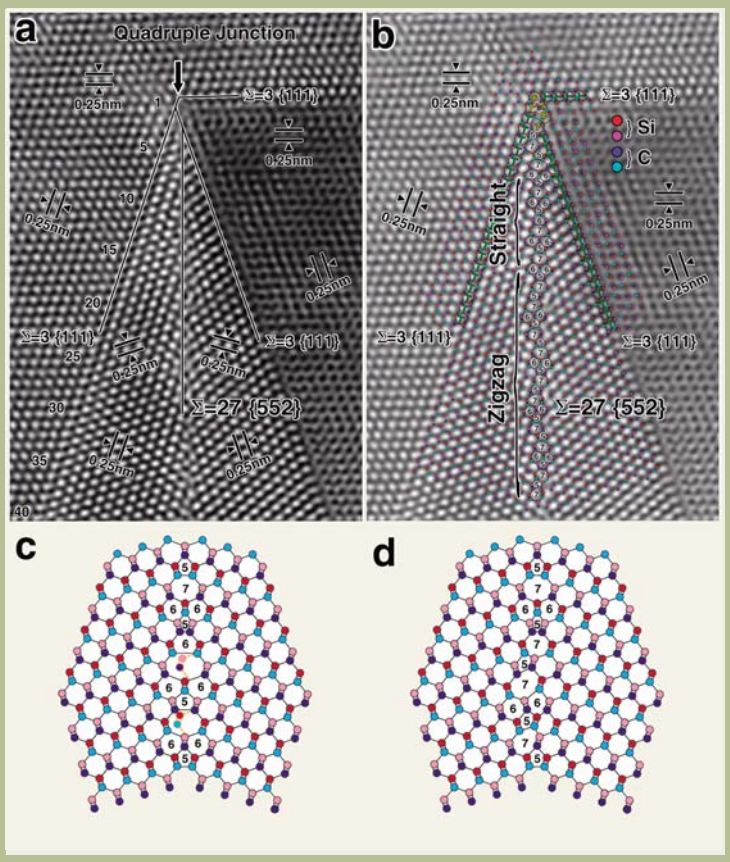

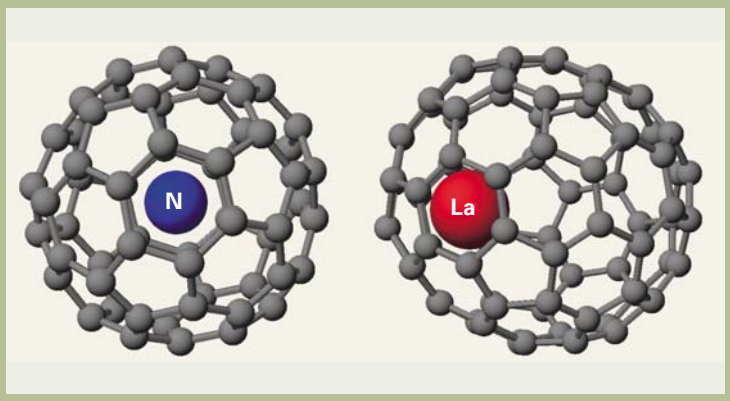

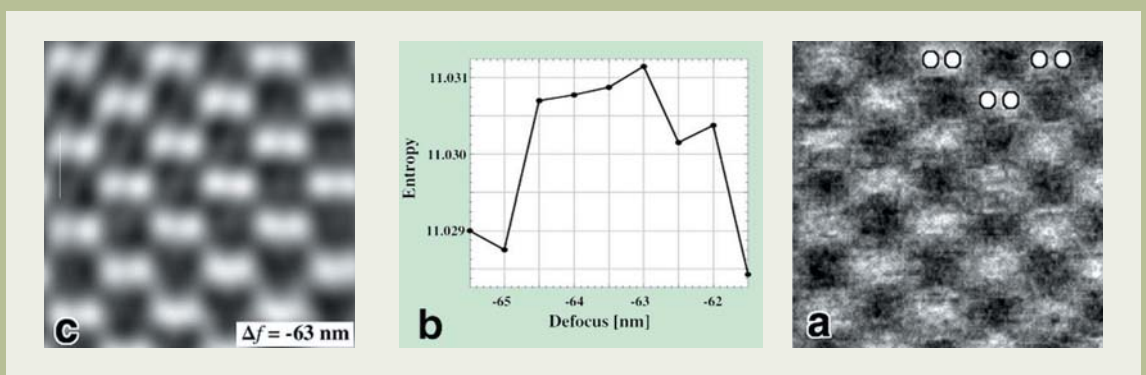

JEOL news

Volume 38 Number 2
November 10, 2003

Atomic Resolved HAADF-STEM for Composition Analysis

Makoto Shiojiri[†],[††], [†††] and Takashi. Yamazaki[††††]

[††]Kanazawa Medical University, Ishikawa 920-0293, Japan
[†††]Kyoto Institute of Technology, Kyoto 606-8585, Japan
[††††]Department of Physics, Tokyo University of Science, Tokyo 162-8601, Japan

Introduction

Atomic-resolution high-angle annular dark-field (HAADF) scanning transmission electron microscopy (STEM) is a quite new technique developed in this decade and has been used to characterize the structure of grain boundaries and precipitates as well as perfect crystals [1]. Although the electron beams run in reverse between STEM microscope and conventional transmission electron microscope (CTEM) (**Fig. 1**), coherent bright field (BF) STEM imaging using a point detector is the same with the CTEM imaging, according to the reciprocity rule [2]. But HAADF STEM is completely different from CTEM and its imaging mechanism is quite complicated. The first part of this paper devotes to physics to understand HAADF STEM. Then, we show a new scheme of HAADF-STEM image simulation, which is available to a routine work, and also the deconvolution processing which provides structural images for intuitive structural and compositional analysis. Some applications that we have made are also demonstrated.

Why are HAADF-STEM Images Incoherent?

It is a fundamental concept of quantum physics that a quantum particle also behaves as wave. Its waves passed through different holes can interfere with each other to show Young's fringes. The interference occurs between the waves scattered by different atoms (exactly, electrostatic potential around atoms) for an electron. But it is caused only between elastically scattered waves or between inelastically scattered waves with the same wavelength. The former gives Bragg reflections. We call, hereafter, the scattering that causes Bragg reflections Bragg scattering. The elastic scattering is no energy-loss scattering. According to quantum mechanism interference between the different electrons never occurs. Thus, interference occurs only between the waves with the same wavelength incorporated with 'a single electron', which may be considered to constitute a wave packet. The electron is observed in terms of the intensity I, which gives a probability of the appearance. The observed electron does not indicate the position $\boldsymbol{r}$ where it locates, but indicates only a place where it is accidentally captured, since it can exist at any place, probably in its wave packet (with any wavelength by inelastic scattering). For the visualization of the most probable position we need the detection of many electrons that are captured at a place assigned with the same interference condition. These electrons are 'coherent' with each other, and show a physically valuable intensity distribution (such as interference fringes or diffraction spots) as a result of the cooperation. Thus, interference is a term for the intra-electron relation of waves, while the term of 'coherent' or 'incoherent' can be used for the inter-electron relation between the waves that belong to the different electrons.

Coherent electrons must have the same birth-place (the source and scattered positions) and the same energy. A field-emission gun can supply a coherent electron beam because it provides the same source at the top of the tip and gives the same energy to the emitting electrons.

The atoms thermally vibrate around their equilibrium positions in the specimen. As mentioned above, interference can occur between elastically scattered waves by different atoms. The electrons whose waves are scattered from the atoms at their thermal equilibrium positions and interfered with each other are completely coherent among them and the resultant intensity forms so-called Bragg reflections. In contrast, the electrons whose waves are scattered from atoms differently displaced from the equilibrium positions are 'incoherent' with each other and also the electrons giving the Bragg

[†]1-297 Wakiyama, Enmyoji Kyoto 618-0091, Japan
[†]E-mail : shiojiri@pc4.so-net.ne.jp

Contents

reflections. The frequency of the thermal lattice vibration ~10^{13} Hz is the fifth power of 10 times as small as a frequency of incident electron wave ~10^{18} Hz, so that the displacements are observable using the electron beam. The scattering from the displaced atoms gives diffuse intensity distribution in a diffraction pattern, and is called thermal diffuse scattering (TDS), accordingly. We assume Einstein model where the atoms moving independently, and take the mean of displacement, which leads to Debye-Waller factor [3]. Frozen phonon method is one of the approaches, where numerical calculations are made by summing up the intensities at several moments [4]. Bragg scattering and TDS are simultaneously included in this method. The lattice vibration may be quantized as phonon. The incident electrons must interact with the phonons, losing or gaining energy ΔE, during the collision. The energy of phonons is in the order of 10^{-1} eV or less (~infrared radiation) and that of the incident electrons is 10^5 eV so that ΔE is negligibly small. In any case, the Bragg scattering is elastic, coherent scattering, while TDS is treated as elastic, incoherent scattering. Then, their intensities are given by the formulae shown in **Fig. 2**.

In STEM, an incident convergent electron probe scans on the surface of the specimen. A STEM image is thus a focal signal recorded on the detector as a function of the probe position. BF-STEM is explained to be equivalent to CTEM in terms of the reciprocity rule (strictly in case of use of an ideal point detector), and then is largely influenced by the imaging condition; defocus, thickness and so on. Howie [5] proposed to use a detector to high-angle range, so-called Howie detector, which excludes Bragg scattering in order to eliminate this phase problem. As seen in Fig. 2a, Bragg reflections within a scattering angle of 2α, where α is a semiangle of probe, cross with one of Ewald spheres in the zero-order Laue zone (ZOLZ). In a high angle range, reflections not only in ZOLZ but also in low higher-order Laue zone (HOLZ) do not cross with any Ewald sphere. Furthermore, the intensity of the Bragg scattering reduces largely with high-angle range as shown in Fig. 2b, comparing with TDS intensity. Therefore Bragg reflections scarcely influence HAADF-STEM imaging. TDS is an origin of unfavorable background, particularly in a high angle range, in electron diffraction and X-ray diffraction. In contrast, HAADF-STEM uses actively this incoherent TDS.

In atomically resolved HAADF STEM, the contrast of an atomic column is obtained as the integrated intensity over the illuminating time, since the scatterings that yield TDS might be incoherent at different moments. This is one of the reasons why HAADF-STEM image is incoherent, and may be called 'laterally incoherent'. Another reason of the incoherent imaging is ascribed to scanning of the convergent beam since the electrons scattered from an atomic column are naturally incoherent with those scattered from different atomic columns in different time. Therefore columns separated laterally are imaged incoherently, that is, STEM image is also transversally incoherent.

The above-argument about 'coherency' is based on quantum physics. However, according to classic wave optics the waves that can interfere with each other are defined as being coherent. When different objects (atoms) are illuminated with a plane wave, the scattered waves from the atoms which are considered to be resources are coherent because they have a definite phase relationships. A perfect incoherent image results from a self-luminous object. Therefore, the incoherent imaging can be obtained when the convergent beam illuminates only a single object, because it emits the scattered wave as a self-luminous resource. In case of atomic-resolved STEM, applying the concept of Lord Rayleigh, whether it is coherent or incoherent imaging depends on whether the Airy discs of neighboring atomic columns have permanent and definite phase relationships between them or not [1]. This is another and prevailing answer for why (HAADF) STEM is incoherent imaging. This definition may be correlated with the transversally incoherent imaging due to the beam scanning mentioned above. Since the behavior of the re-emitted wave is independent from this definition of coherency, both Bragg scattering and TDS in the crystal may be considered to make incoherent images [6]. And, according to this definition even BF-STEM should be regarded as incoherent imaging if it is taken with the probe satisfying the condition of incoherent imaging

Why Does the Simulation Need for HAADF-STEM?

–Effect of the beam probe, detection angle range and thickness of crystal–

It had been believed that HAADF-STEM images exhibit strong atomic number (Z) contrast and can be directly inverted to the object without the need for image simulation, because the phase problem is omitted. However, we found experimentally and theoretically that bright spots appear on channels between the atomic columns in [110] Si images [7] and extraordinary intensity of spot contrasts occurs on light columns in [001] $SrTiO_3$ images [8], when the incident probe is focused to have strong subsidiary tails around a sharp central peak. **Fig. 3** reproduces some of simulated images of [110] Si crystals. 'Total' means STEM images to be observed at given imaging conditions shown by parameters; detection range D, defocus value Δf and thickness t. Those images were calculated for a probe of a semiangle α =12 mrad in a 200 keV-microscope with a spherical aberration coefficient

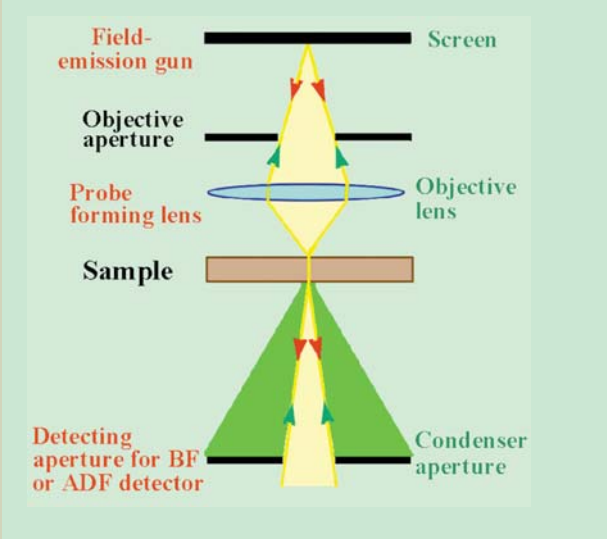

Fig. 1. Ray diagram of scanning transmission electron microscope (STEM) and conventional transmission electron microscope (CTEM). The ray runs downward and upwards in STEM and CTEM, respectively.

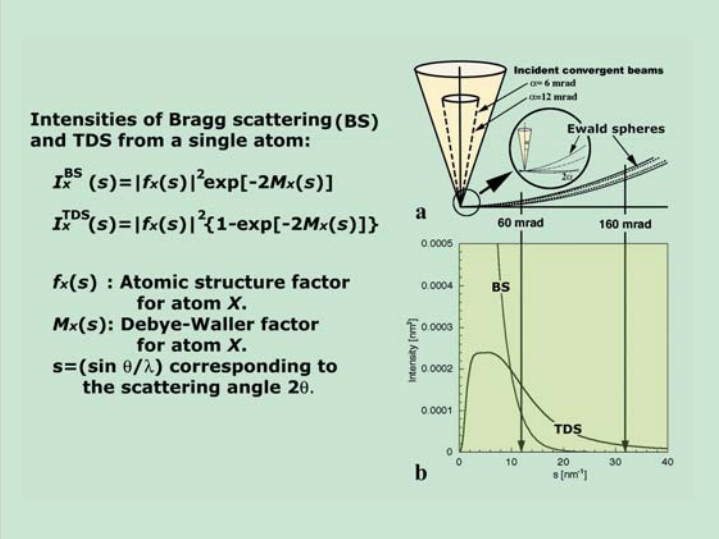

Fig. 2. Intensities of Bragg scattering (BS) and TDS for a single atom of Si, and Ewald construction for convergent electron beams with semiangle α=6 and 12 mrad.

C_s=1.0 mm (JEM-2010F TEM/STEM, in which a lens of C_s=0.5 mm is also available at present). The images calculated for D=60~160 mrad are of HAADF-STEM and D=18~48 mrad forms middle angle (MA) ADF images. The Si-dumbbells are completely resolved but the artificial spots appear in the HAADF-STEM images at Δf =−70 nm. It was explained from wave field calculations that this is caused by the sharp probe but having strong subsidiary maximum, which is shown in **Fig. 4** [8]. It is the reason that when the incident beam is located on channels between the atomic columns, the subsidiary tail forms strong wave fields along the neighboring columns to emit TDS. These artifacts may mislead the structure analysis unless one finds them from image simulation or predicts them from calculation of the probe function. The probe at Δf=−40 nm is so wide that cannot resolve Si-dumbbells.

The shape of probe depends on C_s, Δf and α (as seen from formulae in **Fig. 7**). We have examined the influence of the probe on the contrast of the images, varying these parameters [7-11] and also D and t [7, 9, 11,12]. An optimum imaging condition, which makes the effect of diffraction aberration and spherical aberration minimum, is $\alpha_{opt}=2^{1/2}(\lambda C_s)^{1/4}$ and $\Delta f_{opt}=-(\lambda C_s)^{1/2}$, and provides the most quality HAADF-STEM image. Probe functions and simulated images around the optimum conditions are shown in Fig. 4b and **Fig. 5**, respectively. As far as the lens of C_s as large as 1.0 mm is employed, the appearance of the artificial spots is inevitable.

C_s-correctors have now been developed and tested for practical use [13,14]. In a previous paper we discussed the resolution of the ideal lens in terms of the contrast transfer function [11]. The Si dumbbells are completely resolved in an image calculated for the lens of C_s=0.1 mm, as shown in Fig. 5b. However, a small deviation from the optimum focus, particularly to over-focus side, forms very low contrast image, whose Michelson visibility, defined as $C=(I_{max}-I_{min})/(I_{max}+I_{min})$, is as small as 0.133 for the [110] Si 60 nm thick, while C=0.566 at the optimum focus. This occurs with the illumination of larger area, which is caused by focusing the probe with the large semiangle above or below the surface of the crystal (see Fig. 4b). The C_s correctors allow large α for high resolution, but may cause unfavorable Bragg scattering in HAADF-STEM images. Certainly, the Bragg scattering for the 0.1-mm C_s lens influences the resultant images more than that for the 1.0-mm C_s lens does in the same detection range D=25~45 mm, as seen in Fig. 5. However, HAADF-STEM generally uses the detector in high-angle range, and the strong incident probe due to use of the large semiangle allows us to make the detection range much higher, which can eliminate the coherent scattering influence.

Concerning the dependence of D, we showed experimentally and theoretically that the contribution of the Bragg scattering is so small that can be neglected in HAADF-STEM image but that it cannot be neglected in MAADF-STEM image [12]. In Fig. 3, are shown the simulations of Bragg scattering images and TDS images, separately, together with the total images, for D=60~160 mrad and 18~48 mrad (and also in Fig 5 the simulations for D=25~45 mrad). The multiplicity of inten-

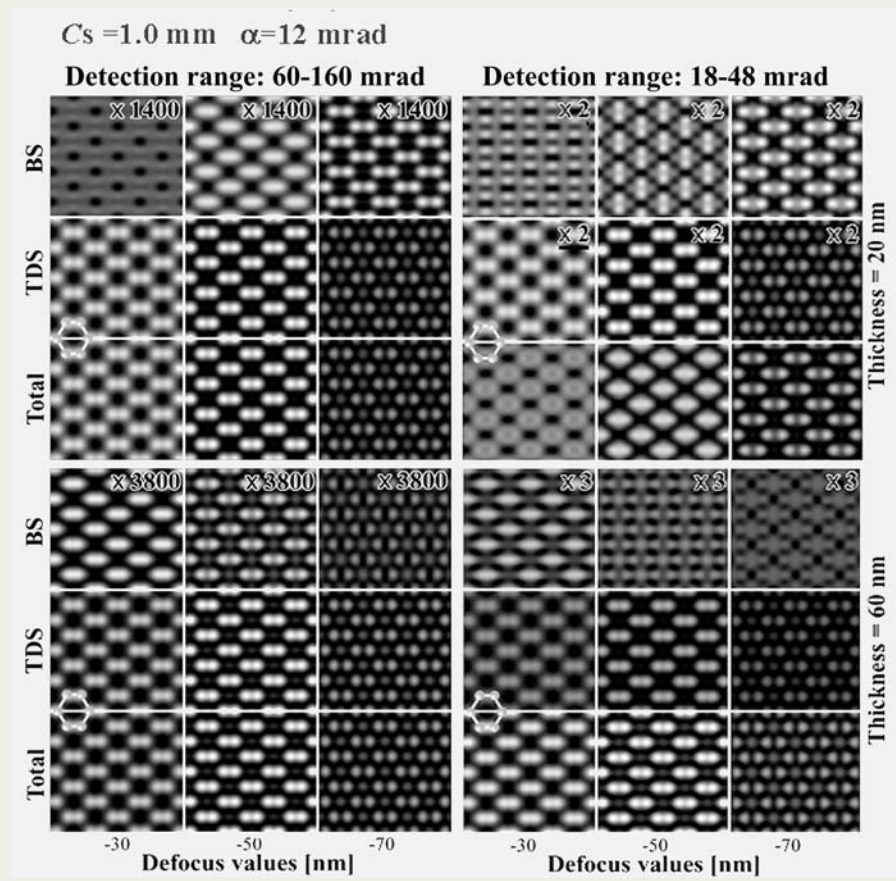

Fig. 3. Simulated high-angle ADF images (a) and middle-angle ADF images (b) of [110] Si crystals 20 nm and 60 nm thick, focused at Δf=–30, –50 and –70 nm using a semiangle of α=12 mrad with a probe forming lens of C_s=1.0 mm at 200 keV. A defocus of Δf= –50 nm corresponds to the optimum focus of this lens. Images due to Bragg scattering (BS) and TDS were calculated separately, and then the total image which means an image to be observed was evaluated. CPU time for any one BS image is about 5 min on a PC (CPU of Intel Pentium 4 (2001) 2 GHz/400 MHz System Bus, 256 KB Cache). The CPU time for any one TDS image is twice as long as that for the BS image because it is necessary to calculate the intensities using two kinds of optical potentials. Additional calculation of an image at different thickness or focus takes about 11 s. Then, these HAADF and MAADF image simulations were done within 20 min [(5 min + 11 s × 5) + (10 min + 11 s × 5) =17 min].

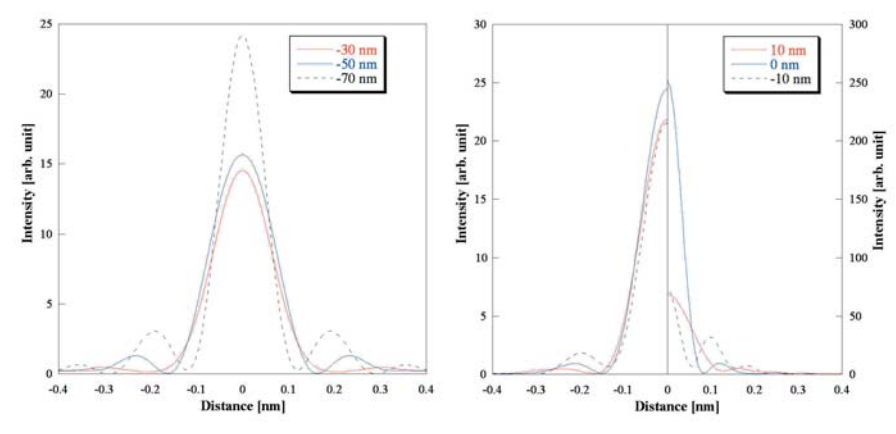

Fig. 4. (a) Probe functions of α=12 mrad focused at Δf= –30, –50 and –70 nm with the lens of Cs=1.0 mm at 200 keV. (b) Probe functions of α=10 mrad focused at Δf= –40, –50 and –60 nm with a lens of C_s=1.0 mm at 200 keV (right) and of α=18 mrad focused at Δf= –6, –16 and –16 nm with a lens of C_s=0.1 mm (left). The legends of (b) denote the value of shift from the optimum defocus. The optimum condition is α_{opt}=10 mrad and Δf_{opt}= –50 mm for C_s=1.0 mm, and α_{opt}=18 mrad and Δf_{opt}=–16 mm for C_s=0.1 mm. In (b) the one sides of the probes are presented. Calculations were made using a formula indicated in Fig. 7.

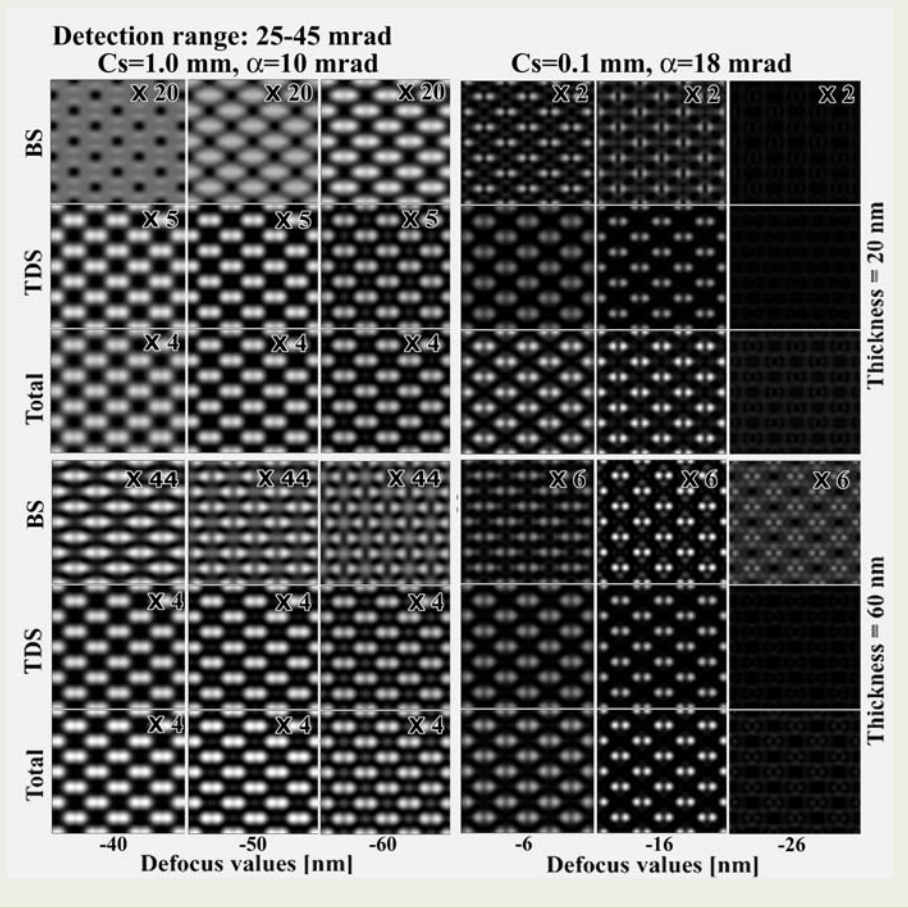

Fig. 5. Simulated middle-angle ADF images of [110] Si crystals 20 nm and 60 nm thick, focused at Δf= –40, –50 and –60 nm using α=10 mrad with the lens of C_s=1.0 mm at 200 keV (a) and at Δf= –6, –16 and –26 nm using α=18 mrad with the lens of C_s=0.1 mm (b). The CPU time for the simulation of images in (a) is almost the same as the simulation of the images shown in Fig. 3. Since the semiangle is large, it takes a long time for the simulation in (b). The CPU time for a BS image is about 2 h and that for a TDS image is about 4 h. Additional calculation of an image at different thickness or focus takes about 11 s. Then, all these calculations were done in about 6 h [(2 h+11 s × 5) + (4 h + 11 s × 5) =6 h].

sity indicated in figures shows that the Bragg scattering, which forms very complicated image contrast depending on focus and thickness, contributes more greatly to the total images as D is settled in smaller angle range.

Each atom ejects TDS electrons, depending on the dynamical wave field of the incident electrons in the crystal that is oscillating and eliminated. Since the contrast of the HAADF-STEM image is given by a simple sum of intensities of TDS electrons collected on the detector, it monotonously increases with increasing thickness t, as shown in Ref. [12] and seen in Figs 3 and 5. In a previous paper [15], the influence of defocusing conditions and thickness change on the experimental HAADF-STEM image was also illustrated using ceramic materials.

The lattice distortion around precipitates or substitutes influences the induced wave field in the crystal and causes unexpected image intensity from the simple Z-contrast, accordingly. The effect of the lattice distortion on the HAADF-STEM images was examined using $SrTiO_3$. It should be taken into account for the image simulation of quantitative composition analysis [8, 9]. Debye-Waller factor of atoms, which is directly conjugated with TDS, might be different between a distorted area such as grain boundary and the perfect crystal. It was also found that a small tilt of the crystal zone axis with respect to the coma-axis of the probe-forming lens causes asymmetric dumbbells in the [110] Si image [16]. Therefore, special care to the beam alignment or the image simulation needs for quantitative HAADF-STEM applications such as the determination of crystallographic polarity or the compositional analysis.

Thus, HAADF-STEM image contrast does not always depend on the number or atomic number of atoms in columns, or does not always show Z-contrast, which expected from Rutherford scattering formula of electron for atoms. Image simulation allows interpretation and quantification of atomic-scale HAADF STEM images.

A Simulation Scheme for Routine HAADF-STEM Works

There are two basic methods for calculation of HAADF-STEM images; multislice method and Bethe method. Multislice method requires enormous computing time comparing to Bethe method, because the whole calculation has to repeat the integration of scattering intensities, at each probe position, over the ADF detector. It used to take half a day or more to display one image. A new scheme for BF- and ADF-STEM simulations has been developed [12]. It contains calculations for the Bragg scattering and TDS, based on Bethe method using two kinds of optical potentials [17]. This scheme reduces the CPU time of the simulation a tenths as compared to a scheme by Pennycook and Jesson on Bethe method [18], which was used in our early investigations [7, 9, 10, 19]. It allows routine works of BF- and ADF-STEM image simulations, accordingly. **Fig. 6** shows a flowchart of the algorism of the new scheme for STEM image simulation, and the formalism of the scheme is shown in **Fig. 7**. First, the probe function is calculated. It shows the intensity distribution of the incident convergent beam on the specimen surface, and depends on C_s, Δf and the wave length λ through the lens aberration function $W(\boldsymbol{K}_{\parallel})$ and α within which the integration is made. Then, the Bloch wave field in the crystal, induced with the convergent incident electron beam, is calculated using Bethe eigenvalue method. The absorption is included into the calculation using optical potentials V'^{all}. The use of V'^{all} means that the absorption due to TDS, plasmon and core loss is all taken into account. The calculation of the Bloch waves gives the intensity of coherent Bragg reflections collected on the detector and, thus provides the BF- or ADF-STEM images due to the Bragg scattering. The images due to Bragg scattering shown in Figs 3 and 5 were calculated in this way.

The intensity I_{all} of absorption calculated above must be the all intensity of electrons scattered over whole angle range, a part of which is TDS electrons, and correlates with a transmission coefficient. Then, the intensity I_{ex} of all electrons that excludes only TDS to be captured with the detector is calculated using the optical potential V'^{ex}. The HAADF-STEM image or ADF-STEM image due to TDS is simply obtained from I_{ex}–I_{all}. This tricky way reduced drastically the CPU time, as shown in figure captions of Figs 3 and 5. The detail of scheme is shown in Ref. 11, and examples of the calculation are shown in our previous papers [8, 11, 15, 16, 19].

As seen in Figs 3 and 5, the contribution of the Bragg scattering is so small that is negligible in HAADF-STEM range. The simulations for TDS give satisfactorily an account of the observed HAADF-STEM images. On the contrary, the Bragg scattering and TDS are in the same order in MAADF STEM. Since the detector cannot selectively collect only one of these scatterings, the image simulation for MAADF STEM should include the calculations for the both elastic scattering and TDS.

Deconvolution Processing of HAADF-STEM Images

HAADF-STEM image intensity $I(\boldsymbol{R})$ may be given by convolution between the probe function $P(\boldsymbol{R})$ and object function (projected atom structure) $O(\boldsymbol{R})$, that is, $I(\boldsymbol{R})\approx P(\boldsymbol{R})*O(\boldsymbol{R})$, under an approximation of nondispersive Bloch waves. Then, an experimental HAADF-STEM image that is deformed by the incident probe can be deduced to the object function by the

deconvolution, $O(\boldsymbol{R})=\mathcal{F}^{-1}\{\mathcal{F}[I(\boldsymbol{R})]/\mathcal{F}[P(\boldsymbol{R})]\}$, where $\mathcal{F}$ and $\mathcal{F}^{-1}$ represent Fourier and inverse Fourier transformation, respectively. We have developed a deconvolution processing technique, where the defocus value assigning the probe function is determined using the maximum entropy method [20]. Images having unresolved Si dumbbells or the artificial bright spots are retrieved to the projected atomic structure, which is shown with schematic illustration in **Fig. 8**. The deconvolution processing is completely different from any conventional image-processing method such as noise filtering through Fourier transform or smoothing or averaging of images, which cannot eliminate the influence of the probe, for instance, the artificial spots.

HAADF-STEM images recorded with field-emission electron microscopes of today are often deformed by instrumental and environmental instability. The deconvolution processing was applied to retrieve a systematically distorted image by referring a HRTEM image [21]. It successfully deduced the *Z*-contrast images of ZnO and a Zn_2Sb-monolayer inversion twin-boundary from a distorted HAADF-STEM image of Sb_2O_3-doped ZnO.

Application to Materials Characterization

With the aid of the image simulation, we can obtain the exact structural and compositional information in atomic-resolved HAADF-STEM images. We reported HAADF-STEM concentration analyses of As atoms along every [110] column in As-doped Si wafers [19] and Bi atoms along every [001] column near the boundary layer in Bi_2O_3-doped $SrTiO_3$ ceramic condensers [9]. The analysis of HAADF-STEM images of inversion boundaries in Sb_2O_3-doped ZnO was performed where both the image simulation and the deconvolution technique were employed [10, 15, 21], and the utility of these two approaches for quantitative analysis has been discussed [22]. With the aid of deconvolution processing, the atomic structure of interfaces [23], the formation and structure of *V*-defects or hexagonal pyramid defects [24] and the relation of strain field and In atom distribution [25] were investigated in multiple quantum wells InGaN/GaN violet laser diodes. Structural and compositional analyses of various perovscite ceramics such as AO-doped $SrTiO_3$ (A=Ca, Sr. Ba) or $CaTiO_3$ have also been in progress [15].

Acknowledgements

One of the authors (MS) deeply thanks Dr. M. Kawasaki, JEOL USA, for inducing him to make this interesting HAADF STEM investigation, at the end of 1998 just before his retirement from Kyoto Institute of Technology, and also to Mr. M. Asanuma, JEOL Europe, for interests and encouragements. Thanks are owing to our collaborators, particularly, coauthors of our papers cited in references. TY would express his special thanks to Prof. I. Hashimoto, Tokyo University of Science, and Prof. K. Watanabe, Tokyo Metropolitan College of Technology, for their guidance, discussion and advice.

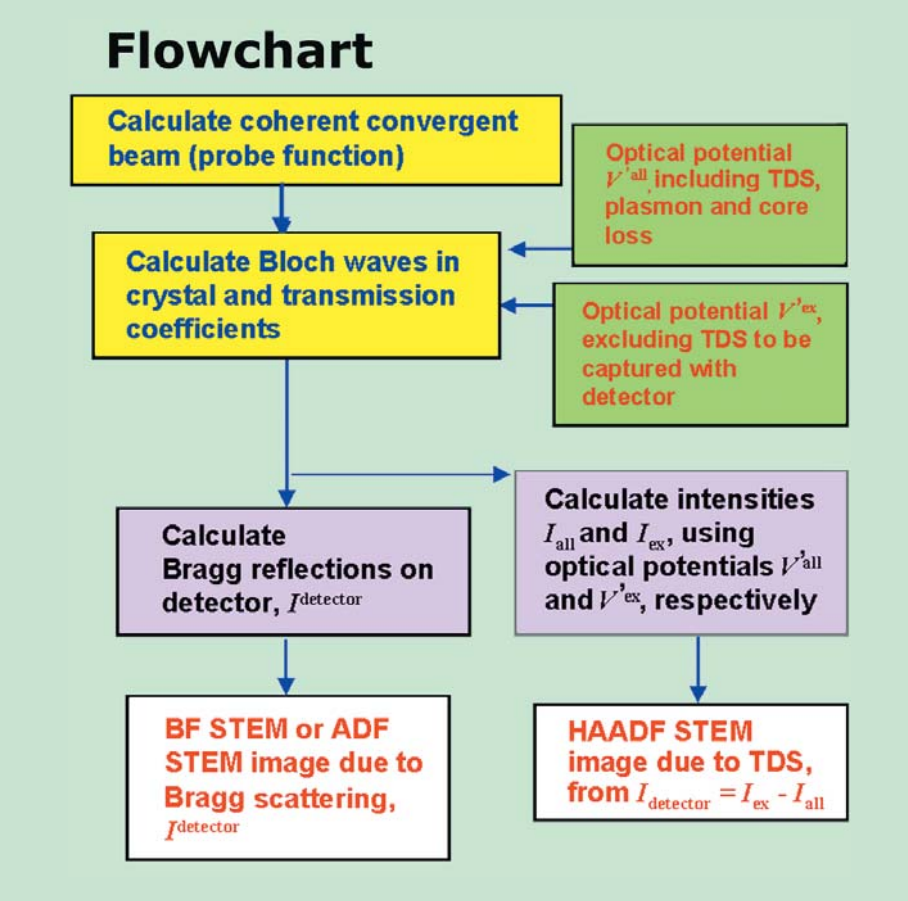

Fig. 6. Flowchart indicating the algorism of a new scheme for HAADF-STM image simulation.

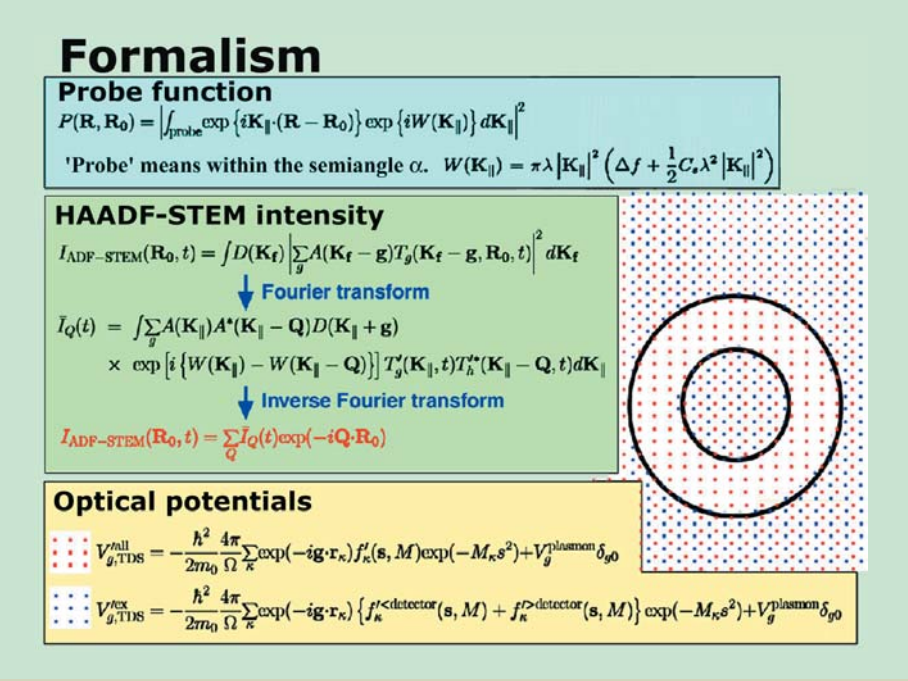

Fig. 7. Formulae for calculation of HAADF-STEM image in the new scheme. Details and notations are shown in Ref. 11. A drawing indicates ranges for potentials V'^{all} and V'^{ex} in respect with the detection range enclosed by two circles.

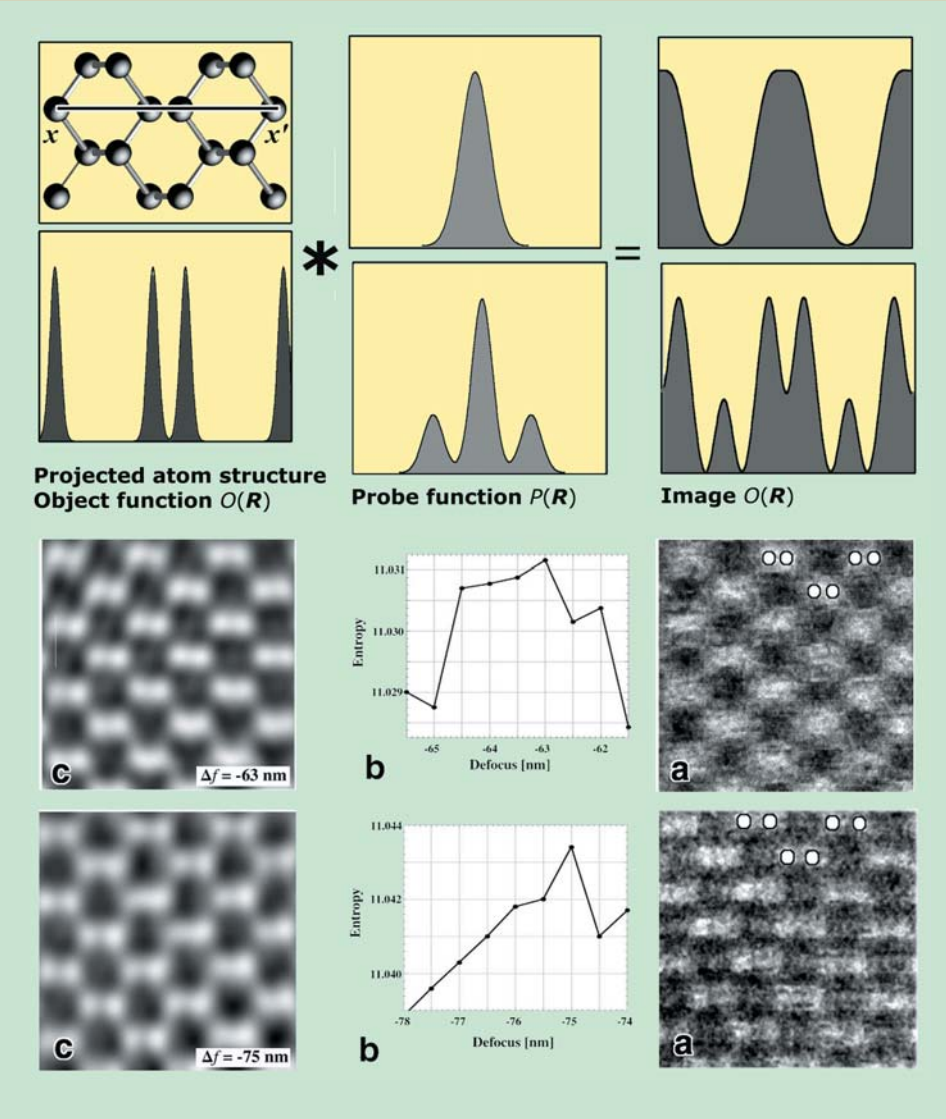

Fig. 8. Deconvolution processing of HAADF-STEM images. An image is taken to be a convolution of the object function (project atom structure) and the 'effective' probe function, as shematical shown for two typical probes. The effective probe function is not the real one. Observed images in (a) were retrieved to *Z*-contrast images in (c) by the deconvolution. The effective probe function used for the deconvolution was obtained from the focus value determined using the maximum entropy method, as shown in (b).

References

1. For example, S.J. Pennycook and P.D. Nellist, in D.G. Rickerby, G. Valdre and U. Valdre (Eds), *Impact of electron and scanning probe microscopy on materials reserach*, Kluwer Academic Publishers, Netherlands, 161 (1999).
2. J. M. Cowley, *Appl. Phys. Lett.* **15**, 58 (1969).
3. R.W. James, *The optical principles of the diffraction of X-rays*, G. Bell and Sons, London, 1948.
4. R.F. Loane, P. Xu and J. Silcox, *Acta Cryst.* **A47**, 267 (1991).
5. A. Howie, *J. Microsc.* **117**, 11 (1 979).
6. P.D.Nellist and S.J. Pennycook, *Ultramicrosc.* **78**, 111 (1999).
7. K. Watanabe, T. Yamazaki, I. Hashimoto and M. Shiojiri, *Phys. Rev.* **B64**, 115432 (2001).
8. T. Yamazaki, M. Kawasaki, K. Watanabe, I. Hashimoto and M. Shiojiri, *J. Electron Microsc.* **50**, 517 (2001).
9. M. Kawasaki, T. Yamazaki, S. Sato, K. Watanabe and M. Shiojiri, *Phil. Mag.* **A81**, 245 (2001).
10. T. Yamazaki, K. Watanabe, A. Recnik, M. Ceh, M. Kawasaki and M. Shiojiri, *J. Electron Microsc.* **49**, 753 (2000).
11. K. Watanabe, N. Nakanishi, T. Yamazaki, M. Kawasaki, I. Hashimoto and M. Shiojiri, *Phys. Stat. Sol.* **(B) 235**, 179 (2003).
12. K. Watanabe, T. Yamazaki, Y. Kikuchi, Y. Kotaka, M. Kawasaki, I. Hashimoto and M. Shiojiri, *Phys. Rev.* **B63**, 085316 (2001).
13. P.E. Batson, N. Dellby and O.L. Krivanek, *Nature* **418**, 617 (2002).
14. J.L. Hutchison, J.M. Titchmarsh, D.J.H. Cockayne, G. Möbus, C.J.D. Hetherington, R.C. Doole, F. Hosokawa, P. Hartel and M. Haider, *JEOL news* **37E**, 2 (2002).
15. S. Sturm, A. Recnik, M. Kawasaki, T. Yamazaki, K. Watanabe, M. Shiojiri and M. Ceh, *JEOL news* **37E**, 22 (2002).
16. T. Yamazaki, M. Kawasaki, K. Watanabe, Hashimoto and M. Shiojiri, *Ultramicrosc.* **92**, 181 (2002).
17. C. R. Hall and P. B. Hirsch, *Proc. Roy. Soc. of London* **A286**, 158 (1965).
18. J. Pennycook and D. E. Jesson, *Phys. Rev. Lett.* **64**, 938 (1990).
19. T. Yamazaki, K. Watanabe, Y. Kikuchi, M. Kawasaki, I. Hashimoto and M. Shiojiri, *Phys. Rev.* **B61**, 13833 (2000).
20. K. Watanabe, Y. Kotaka, N. Nakanishi, T. Yamazaki, I. Hashimoto and M. Shiojiri, *Ultramicrosc.* **92**, 191 (2002).
21. N. Nakanishi, T. Yamazaki, A. Recnik, M. Ceh, M. Kawasaki, K. Watanabe and M. Shiojiri, *J. Electron Microsc.* **51**, (2002) 383.
22. T. Yamazaki, N. Nakanishi, A. Recnik, M. Kawasaki, K. Watanabe, M. Ceh and M. Shiojiri, *Ultramicrosc.* in print.
23. K. Watanabe, J.R. Yang, N. Nakanishi, K. Inoke and M. Shiojiri, *Appl. Phys. Lett.* **80**, 761 (2002).
24. K. Watanabe, J.R. Yang, S.Y. Huang, K. Inoke, J.T. Hsu, R.C. Tu, T. Yamazaki, N. Nakanishi and M. Shiojiri, *Appl. Phys. Lett.* **82,** 718 (2003).
25. K. Watanabe, N. Nakanishi, T. Yamazaki, J.R. Yang, S.Y. Huang, K. Inoke, J.T. Hsu, R.C. Tu and M. Shiojiri, *Appl. Phys. Lett.* **82**, 715 (2003).

Atomic Structure Analysis of Σ=3, 9 and 27 Boundary, and Multiple Junctions in β-SiC

Koji Tanaka, Masanori Kohyama

Special Division for Green Life Technology, National Institute of Advanced Industrial Science and Technology, AIST Kansai.

The atomic structures of Σ=3, 9 and 27 boundary, and multiple junctions in β-SiC were studied by the high-resolution electron microscopy (HREM). Especially, the existence of the variety of structures of Σ=3 incoherent twin boundaries and Σ=27 boundary was shown by HREM. The structures of Σ=3, 9 and 27 boundary were explained by structural unit models.

Introduction

There has been increasing interest in SiC as high-temperature devices or high-performance ceramics. It is very crucial to investigate the structures and properties of grain boundaries (GBs) of SiC, because grain boundaries in sintered ceramics or polycrystalline films have significant effects on bulk properties. The study of GB by the HREM is now one of the main tools for understanding materials. A rigid body translation of one grain relative to the other is an important part of the atomic relaxation of a grain boundary. The presence of a rigid body translation along the common <111> direction at {211}Σ=3 incoherent twin boundary (ITB) was found in Si [1] and Ge [2], whereas no rigid body translation was found under different conditions in Si [1] or in diamond [3]. It was also pointed out that the translation state was sensitive to the environment of the boundary [4]. Finally, the inclination of the boundary plane can also be a possible factor in the decrease of the energy [4].

In the present study, {211}Σ=3 ITB and its junction with {111}Σ=3 coherent twin boundaries (CTBs), {221}Σ=9 boundary and its triple junction with {111}Σ=3 CTBs, and {552}Σ=27 boundary and its quadruple junction with {111}Σ=3 CTBs have been investigated by the HREM and compared with the theoretical study.

Experiment

The transmission electron microscope (TEM) specimen of chemical vapor deposition (CVD) β-SiC was prepared by the mechanical thinning and ion milling. CVD techniques can easily provide dense materials of high purity and interfaces that are well-defined even in covalent materials. Moreover, CVD specimens often exhibit a preferred orientation during growth and this enhances the probability of coincident site lattice (CSL) grain boundary formation. A HREM and an EELS analysis was performed on CVD β-SiC with a preferred orientation of {220} and grain size of approximately 10 μm using the field emission (FE) TEM (JEOL, JEM-3000F). Atomic models were given on the basis of the structural unit model. The relaxed atomic positions and grain boundary energies were calculated by the self-consistent tight-binding (SCTB) method.

1-8-31 Midorigaoka, Ikeda, Osaka, 563-8577, Japan,
E mail : koji.tanaka@aist.go.jp

Results

In the case of Σ=3

Figure 1 (a) ~ **(d)** show the atomic models of the non-polar interfaces of {211}Σ=3 ITBs in β-SiC. They include suitable reconstructions, in which arrows indicate the <011> bonds. These are symmetric and asymmetric models, respectively. Type A and B are constructed for the respective models. Si atoms are reconstructed in Type A, and C atoms in Type B. The relaxed atomic positions in Fig. 1 are calculated by the SCTB method.

The wrong bonds exist at the two types of positions. These are the intergranular bonds and the <011> bonds. The intergranular bonds exist on the {022} plane and cross the interface. The <011> bonds that are reconstructed connect the two atoms on the neighboring {022} planes, and double the periodicity along the <011> direction. The kinds and positions of the wrong bonds in Type A are inverted in Type B.

From the calculation by the SCTB method, the grain boundary energies of Fig. 1 (a) ~ (d) are 1.71, 2.37, 1.39, and 2.42 Jm^{-2}, respectively. Type A of the asymmetric model is the most stable and Type B of the asymmetric model has the largest energy. The energy difference between Type A of the symmetric model and Type A of the asymmetric model is not so large, which indicates both structures can occur. The rigid-body translation in Type A of the symmetric model is a dilation of 0.001 nm and that in Type B is a dilation of 0.024 nm. The rigid-body translation in Type A of the asymmetric model is a shift of 0.072 nm along the <111> direction with a dilation of 0.016 nm. That in Type B is a shift of 0.068 nm along the <111> direction with a dilation of 0.032 nm.

Figure 2 (a) and **(c)** are HREM images of the {211}Σ=3 ITB in β-SiC. The length of {211}Σ ITB is 6 {111} layers in Fig. 2 (a), 18 {111} layers in (c). [The lengths are indicated by numbers in Fig. 2 (a) ~ (d).] As can be easily recognized, the {111} planes on different sides of ITB reveal no shift in Fig. 2 (a), whereas no shift near the junctions with a {111}Σ=3 CTB and a shift of about one fifth of the {111} plane distance near the center of {211}Σ=3 ITB in (c). This indicates that the rigid body translation along the <111> is zero in Fig. 2 (a), and zero near the junctions and about 0.05 nm near the center in (c).

Atomic models for {211}Σ=3 ITB in Fig. 2 (a) and (c) were given on the basis of the results of the theoretical calculations. Fig. 2 (b) and (d) are structural unit models superimposed on HREM images corresponding to Fig. 2 (a) and (c), respectively. White circles represent the reconstruction along the <011> direction. It is obviously seen that the structural unit which consists of symmetric 5-7-6 membered rings align along the boundary in Fig. 2 (b), the symmetric structural units are filled in near the junction between a {111}Σ=3 CTB and a {211}Σ=3 ITB and the asymmetric structural units consisted of 5-7-6 membered rings are filled in at the middle of the {211}Σ=3 ITB in (d). All structural unit models fit with the HREM images very well. It should be noted that the positions of all white circles correspond to the Si site and it was shown that the grain boundary energy was lower when Si was reconstructed than C by the theoretical calculation.

The obtained <111> translation was approximately 0.05 nm in the experimental result and 0.072 nm in Type A in the theoretical calculation, respectively. It should be noted that the structure of {111}Σ=3 CTB plays like an anchor because it is very stable and rigid, and a {211}Σ=3 ITB always stays with a {111}Σ=3 CTB in real materials, which is essentially different from the ideal bicrystal in the simulation. At the short boundary, it is difficult to translate along the common <111> direction because the top and bottom of the {211}Σ=3 ITB are anchored by the {111}Σ=3 CTB. However, the <111> translation can occur at the relatively long boundary because

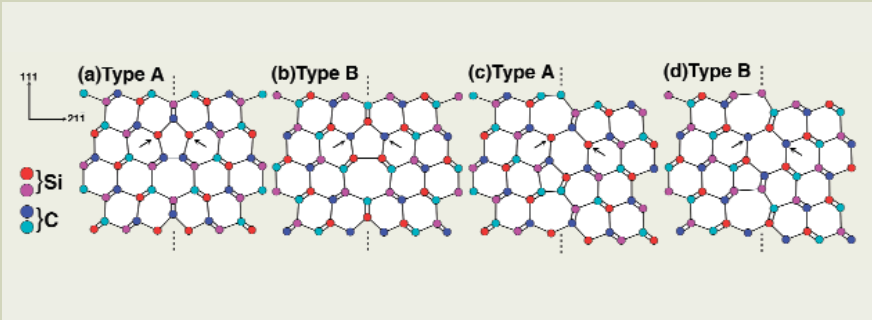

Fig. 1 Atomic models of {211}Σ=3 incoherent twin boundary in β-SiC. (a) and (b) are symmetric. (c) and (d) are asymmetric. Arrows indicate the <011> reconstruction bonds. Si atoms are reconstructed in Type A, and C atoms in Type B.

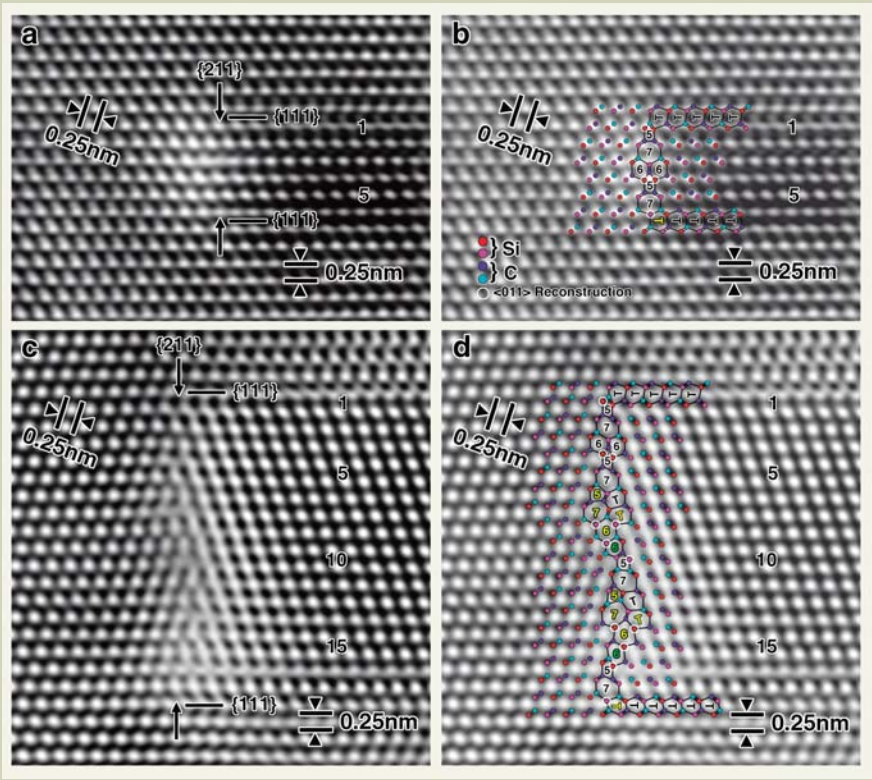

Fig. 2 (a) and (b) : HREM images of the Σ=3 incoherent twin boundary in β-SiC. (c) and (d) : Structural unit models superimposed on HREM images corresponding to (a) and (c), respectively. White circles represent the reconstruction along the <011> direction.

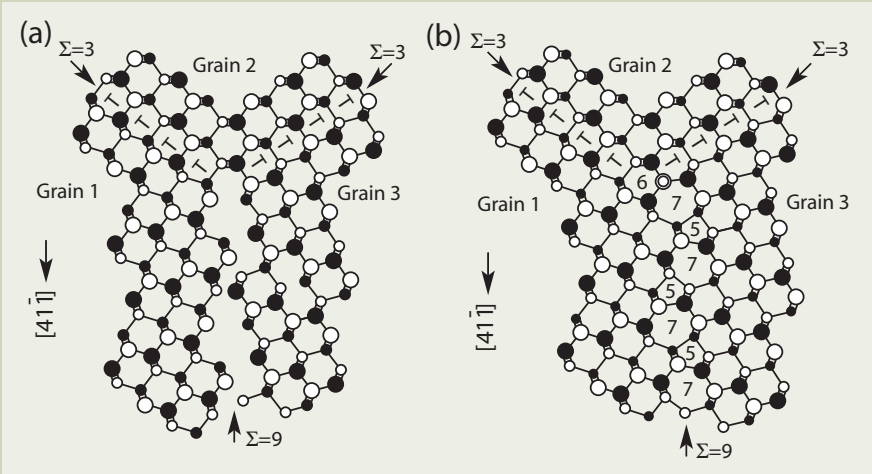

Fig. 3 Atomic model of a triple junction between one {221}Σ=9 and two {111}Σ=3 boundaries in zincblend structure along the [011] direction. Open and closed circles indicate different elements and the size difference indicates the atoms with different height. (a) : Ideal position. (b) : One atomic column off. The double circle represents the reconstruction along the [011] direction.

the restriction from the {111}Σ=3 CTB is not so severe near the center of the {211}Σ=3 ITB. The reason why the experimental value is smaller than the theoretical calculation one might be that atoms can not be fully relaxed because of an anchor effect from {111}Σ=3 CTB.

As discussed above, the structures of {211}Σ=3 ITB in β-SiC were explained very well by the prediction of the SCTB calculation.

In the case of Σ=9 and triple junction

Figure 3 (a) shows an atomic model of an ideal triple junction (TJ) between one {221}Σ=9 and two {111}Σ=3 CTBs in zincblend structure along the [011] direction. It is seen from Fig. 3 (a), atoms can not have proper bonds at the {221}Σ=9 boundary because of the height differences in the {022} stacking. By introducing an 1/4[011] translation, the symmetric structure consisted of 5-6-7-6 membered rings can be achieved at the {221}Σ=9 boundary. And by introducing an 1/9[41$\bar{1}$] translation, the zigzag structure consisted of 5-7-5-7 membered rings can be achieved. It was shown that the zigzag 5-7-5-7 structure has lower energy than the symmetric 5-6-7-6 structure in Si [5]. However, introducing an 1/4[011] translation at a GB result in introducing a screw dislocation at a TJ and introducing an 1/9[41$\bar{1}$] translation result in introducing an edge dislocation. Therefore, both cases cause an increase in the total GB energy around the TJ. On the other hand, the zigzag 5-7-5-7 structure can be achieved by shifting a GB plane by one atomic column as seen in **Fig. 3 (b)**. In this case, no extra dislocation is introduced, therefore the total GB energy around the TJ seems lower than the case of introducing a translation.

Figure 4 (a) is a HREM image of TJs between one {221}Σ=9 and two {111}Σ=3 CTBs in β-SiC and **Fig. 4 (b)** is a structural unit model superimposed on the HREM image corresponding to Fig. 4 (a). It is clear that the {221}Σ=9 boundary start from one atomic column away form the ideal TJ and the stable zigzag 5-7-5-7 structure is achieved. It should be noted that choosing a GB position has the same effect as a translation.

In the case of Σ=27 and quadruple junction

Figure 5 (a) is a HREM image of a quadruple junction (QJ) between one {552}Σ=27 and three {111}Σ=3 CTBs in β-SiC and **Fig. 5 (b)** is a structural unit model superimposed on the HREM image corresponding to Fig. 5 (a). It is seen that the {552}Σ=27 boundary does not start from the ideal QJ and the symmetric structure consisted of 5-7-6-5-6-7 membered rings is achieved near the QJ but the zigzag structure consisted of 5-7-5-7-6 membered rings is achieved far from the QJ. The GB energy of the zigzag model is smaller than the symmetric model according to the SCTB calculation for β-SiC [6].

Figure 5 (c) and **(d)** are atomic models of {552}Σ=27 boundary. Figure 5 (c) is a symmetric model and (d) is a co-existence model of a symmetric and a zigzag structure. As indicated in Fig. 5 (c), the zigzag structure consisted of 5-7-5-7-6 membered rings like Fig. 5 (d) is achieved if the GB position shifts

one atomic column from the symmetric structure position. To achieve the zigzag structure, an atomic relaxation is necessary. Also, the restriction from {111}Σ=3 CTBs is so strong near the QJ and there is no space for an atomic relaxation. It might be the reason why the symmetric structure is achieved near the QJ and the zigzag structure is achieved far from the QJ.

Conclusion

The HREM and the theoretical calculation showed that the atomic structures of Σ=3, 9 and 27 boundary, and multiple junctions in β-SiC were well explained by structure unit models. The translation state was sensitive to the environment of the boundary. A shift of GB position has the same effect as a rigid body translation.

References

1. H. Ichinose, Y. Tajima, and Y. Ishida in *Grain Boundary Structure and Related Phenomena*, (Supple. to Trans. of the Japan Institute of Metals, **27** Sendai, Japan 1986), p. 253-260.
2. A. Bourret, and J. J. Bacmann in *Grain Boundary Structure and Related Phenomena*, (Supple. to Trans. of the Japan Institute of Metals, **27** Sendai, Japan 1986), p. 125-134.
3. Y. Zhang, H. Ichinose, Y. Ishida, K. Ito, and M. Nakanose in *Diamond for Electronic Application*, edited by D. L. Dreifus, A. Collins, T. Humphreys, K. Das, and P. E. Pehrsson (Mater. Res. Soc. Proc. **416**, Pittsburgh, PA 1996), p. 355-360.
4. K. Tanaka, M. Kohyama, and M. Iwasa, Matl. Sci. Forum, **294-296**, p. 187 (1999).
5. M. Kohyama, Matl. Sci. Forum, **207-209**, p. 265 (1996).
6. M. Kohyama and K. Tanaka, to be published.

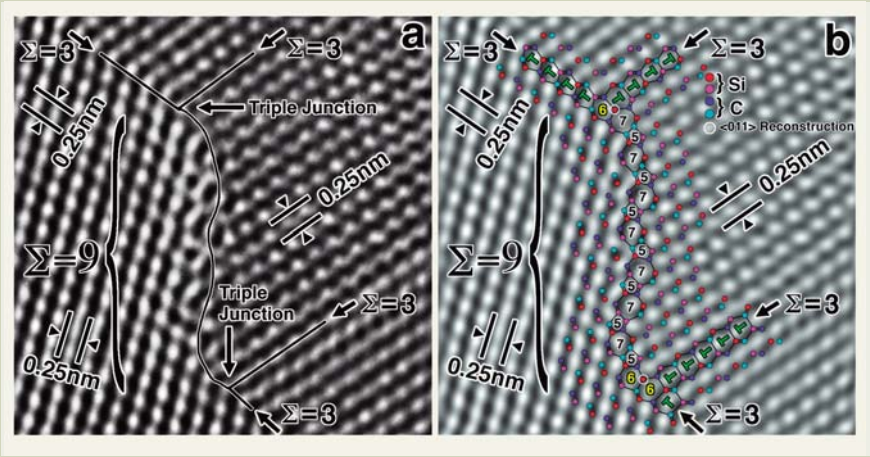

Fig. 4 HREM image of triple junctions (a) and a structural unit model superimposed on it (b). White circles represent the reconstruction along the <011> direction.

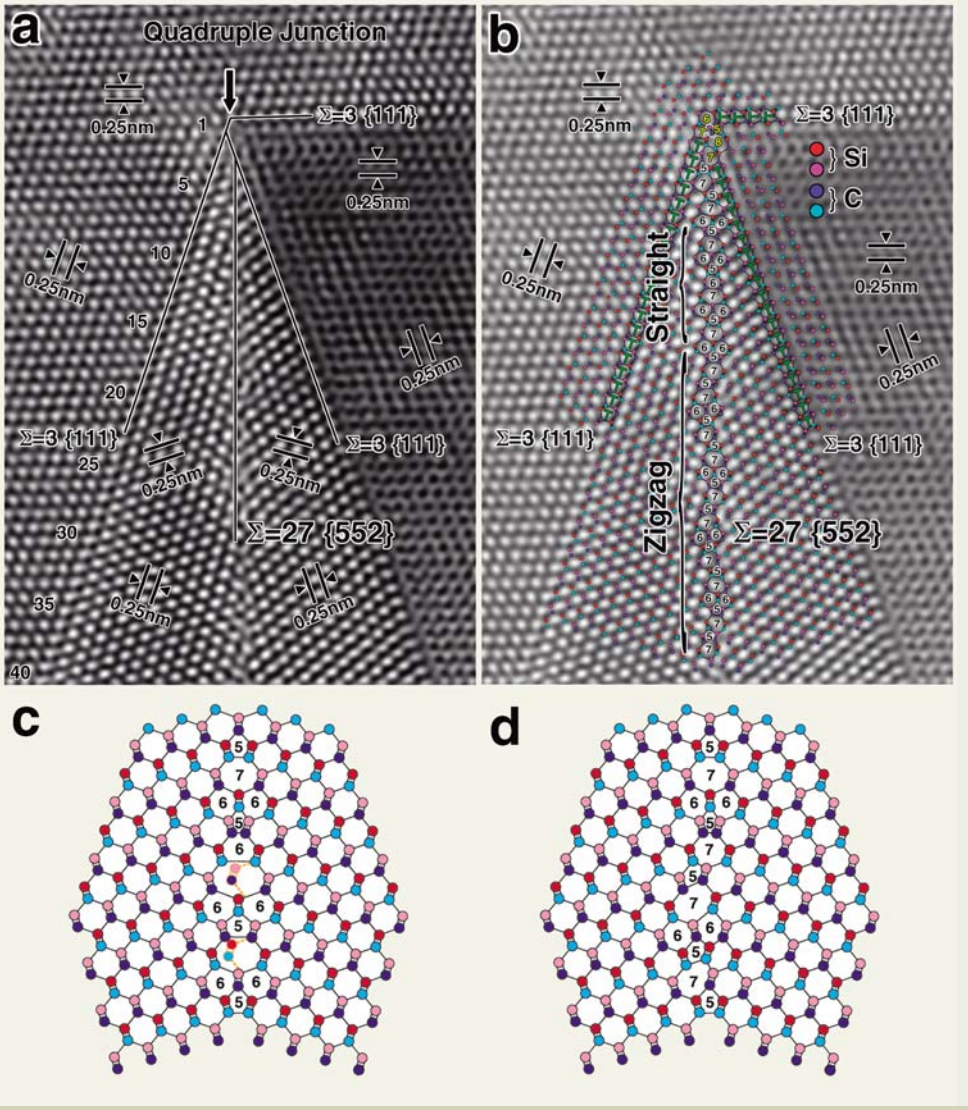

Fig. 5 (a) : HREM image of a quadruple junction between one {552}Σ=27 and three {111}Σ=3 boundaries in β-SiC.
(b) : Structural unit model superimposed on (a).
(c) : Symmetric model.
(d) : Co-existence model of a symmetric and a zigzag structure.

Direct Imaging of a Local Thermal Vibration Anomaly Through *In-situ* High-temperature ADF-STEM

Eiji Abe

National Institute for Materials Science

A real-space imaging of a local thermal vibration anomaly in a solid has been demonstrated for the first time, through atomic-resolution annular dark-field scanning transmission electron microscope (ADF-STEM) observations of an $Al_{72}Ni_{20}Co_8$ quasicrystalline compound. Significant changes of ADF-contrast depending on the observation temperature (as well as the angle ranges of the annular-detector) are found to be obvious at some particular Al atomic sites. The origin of this anomalous ADF-contrast is explained fairly well by the thermal diffuse scattering (TDS) intensity change due to different values of Debye-Waller factor, which is defined by mean-square thermal vibration amplitude of the atoms. These localized atomic fluctuations presently observed in the quasicrystal provide an important hint on an issue of *phason* – the *phason* is an extra elastic degree of freedom specific to the quasiperiodic order (in addition to the usual phonons in crystals) and has been theoretically predicted to cause localized fluctuations.

Introduction

Annular dark-field scanning transmission electron microscopy (ADF-STEM) provides atomic-resolution images by effectively illuminating each atomic column one-by-one as a finely focused electron probe (<~2 Å) is scanned across the specimen, due to the fact that the fast incidence-electrons propagate along the atomic columns with strong channeling effects, generating an intensity map at the annular detector (**Fig. 1**). To a good approximation, the atomic-resolution in ADF-STEM is interpreted to be a result of independent intensity measurements of electrons scattered from individual atomic columns, and hence the observed intensity distribution ($I(\mathbf{R})$) can be simply described by a convolution between a probe-intensity function ($P(\mathbf{R})$) and a scattering object function ($O(\mathbf{R})$) (incoherent image) [1];

$$I(\mathbf{R}) = O(\mathbf{R}) \otimes P(\mathbf{R}) \qquad (1)$$

Here, $O(\mathbf{R})$ represents the columnar scattering cross-section that contributes to the annular detector. By detecting sufficient high-angle scatterings ($s > \sim 1\,Å^{-1}$: see **Fig. 2**), the intensity at the detector is dominated by phonon scattering events; that is, thermal diffuse scattering (TDS). An Einstein model of independently vibrating atoms is valid enough to describe the multiphonon contribution that dominates high-angle diffuse scatterings. Therefore, the TDS intensity can be practically treated by an absorptive form factor given as an attenuation of the elastic scattering by the Debye-Waller (DW) factor, whose high-angle approximation is well described by the TDS cross section (σ_{TDS}) effective to the annular-detector range [1]:

$$f'_{HA}(M, s) \approx \sigma_{TDS} \propto \int_{detector} f^2(s) [1-\exp(-2M \cdot s^2)] d^2\mathbf{s} \quad (2)$$

where the $f'_{HA}(M, s)$ is the absorptive atomic form factor for high-angle scatterings and the $f(s)$ is the atomic form factor for elastic scatterings (with $s=\theta/2\lambda$, θ is a scattering angle, λ is the electron wave-length) and M is the DW factor defined by mean-square thermal vibration amplitude of the atoms. Therefore, the intensity of each illuminated atomic column will be directly dependent on the σ_{TDS} within the relevant column. We note that TDS described by σ_{TDS} is sufficient for estimating the integrated intensity reaching the detector, although it does not reflect any fine details [2] of the high-angle diffraction pattern.

Since the TDS intensity is proportional to the square of $f(s)$ (Eq.(2)), the ADF-STEM provides a significant atomic-number dependent contrast (Z-contrast) which has been quite useful to determine the local chemical structures at atomic scale. In addition to this amplitude sensitive nature of ADF-contrast, it should be reminded that the $f'_{HA}(M, s)$ (or σ_{TDS}) is a function of both M and s (see the upper-right hand side in Fig. 1) ; ADF-contrast is also sensitive to the DW factors at individual atomic sites. With this in mind, we here describe the first direct imaging of a local thermal vibration anomaly in a solid [3], through *in-situ* heating/cooling (and angle-resolved) ADF-STEM experiments.

STEM Experiment

ADF-STEM was performed by a JEM-2010F (URP version with spherical aberration Cs=0.5mm) equipped with a scanning unit [4]. The minimum probe is approximately ~1.5 Å with a convergence angle of ~12 mrad, and it can reveal clearly the dumb-bell feature of the GaAs structure, as shown below in Fig.1. Samples for STEM observation were prepared by dispersing crushed alloys on perforated carbon films supported on copper grids; by this method, surface amorphous layer, roughness, and contamination that are frequently induced by ion-milling and strongly affect the ADF contrast can be avoided. *In-situ* atomic-resolution ADF-STEM observation at 1100K was achieved using a heating holder (JEOL EM-31050) that does not require any water-cooling during the observation even at 1100K.

ADF-STEM Observation of $Al_{72}Ni_{20}Co_8$ Quasicrystal

The structure of quasicrystals – having long-range order with symmetries that are incompatible with periodicity – is often described with reference to a higher-dimensional analogue of a periodic lattice [5]. Within the context of this 'hyperspace' crystallography, lattice dynamics of quasicrystals can be described by a combination of lattice vibrations and atomic fluctuations - phonons and phasons. The phason is an extra elastic degree of freedom that may cause

1-2-1 Sengen, Tsukuba 305-0047 Japan
E-mail: abe.eiji@nims.go.jp

an anomalous fluctuation at specific atomic sites, and the DW factor of a quasicrystal can be written as;

$$M = M_{\text{phonon}} + M_{\text{phason}} \qquad (3)$$

Here we present the direct observation of local anomalies of the DW factor in a quasicrystal, through an *in-situ* high-temperature ADF-STEM observation on a decagonal $Al_{72}Ni_{20}Co_8$ for which a nearly-perfect, ideal quasiperiodic structure can be obtained by annealing at 1100K (the thermodynamically stable phase). In the observation at room temperature (300K: **Fig. 3 (a)**), the ADF-STEM image highlights the transition metal (TM : Ni or Co) positions relative to the Al due to the $f^2(s)$ dependence of the contrast (Eq. (2)). But when the sample is heated and held at a temperature of approximately 1100K in the microscope, we find a remarkable change in the relative contrast; compare **Fig. 3 (b)** to Fig. 3 (a). It is evident that a significant enhancement in contrast appears at some specific places that can be well represented by the pentagonal quasiperiodic lattice with an edge-length of 2 nm. Further, we notice that the anomalous ADF-contrast occurs at cores of the decagonal cluster (Fig. 3 (b)) which is a structural unit of the decagonal $Al_{72}Ni_{20}Co_8$ [6]. A representative feature of the clusters is shown in **Figs. 4 (a)** and **(b)**. Viewing carefully the interior contrast of the decagons, an increase of intensities is found to be significant at the positions indicated by arrowheads, which are the Al sites in the decagonal cluster model (**Fig. 4 (c)**). The intensity profiles show that the Al atom at the core, denoted as Alα, in fact shows stronger contrast at 1100K than that at 300K. We confirmed that this temperature-dependence contrast change is reversible; that is, after cooling down to 300K from 1100K, the anomalous contrast regions become darker again. It should be noted that the intensity at the Alα site ($\boldsymbol{I}_{\text{Al}\alpha}$) is originally stronger than that of the other Al sites at 300K (Fig. 4 (a)); the $\boldsymbol{I}_{\text{Al}\alpha}$ is confirmed to vary significantly depending on the angular range of the detector [3]. These angular-dependent as well as temperature-dependent (reversible) anomalous ADF-contrast can naturally be attributed to a local anomaly of the DW factor, as expected through Eq. (2); assuming that the DW factor effect is equivalent for all the Al sites, neither of these dependences is expected. We interpreted the significant increase of $\boldsymbol{I}_{\text{Al}\alpha}$ in terms of atomic vibration amplitudes, $\langle u^2 \rangle$, and successfully showed that the observed anomalous ADF-contrast at the Alα site is clearly correlated with differences in $\langle u^2 \rangle$ [3]. This is, to our best knowledge, the first direct observation of a local vibration anomaly in a solid.

The local anomalies of $\langle u^2 \rangle$ presently observed imply significant anharmonicity at the Alα site. Similar anomalies might therefore be anticipated at the neighboring TM sites, and some evidence of this is seen at 1100K (Fig. 4 (b)). Here it is quite interesting to note that the Alα sites, located at the center of the decagonal clusters that are on the 2 nm-scale pentagonal quasiperiodic lattice vertices, are shown to be phason-related according to the hyperspace crystallographic description [7]. Thus, the present local DW factor anomaly indicates an occurrence of phasonic fluctuations – a perturbation of a quasiperiodic order that can be described

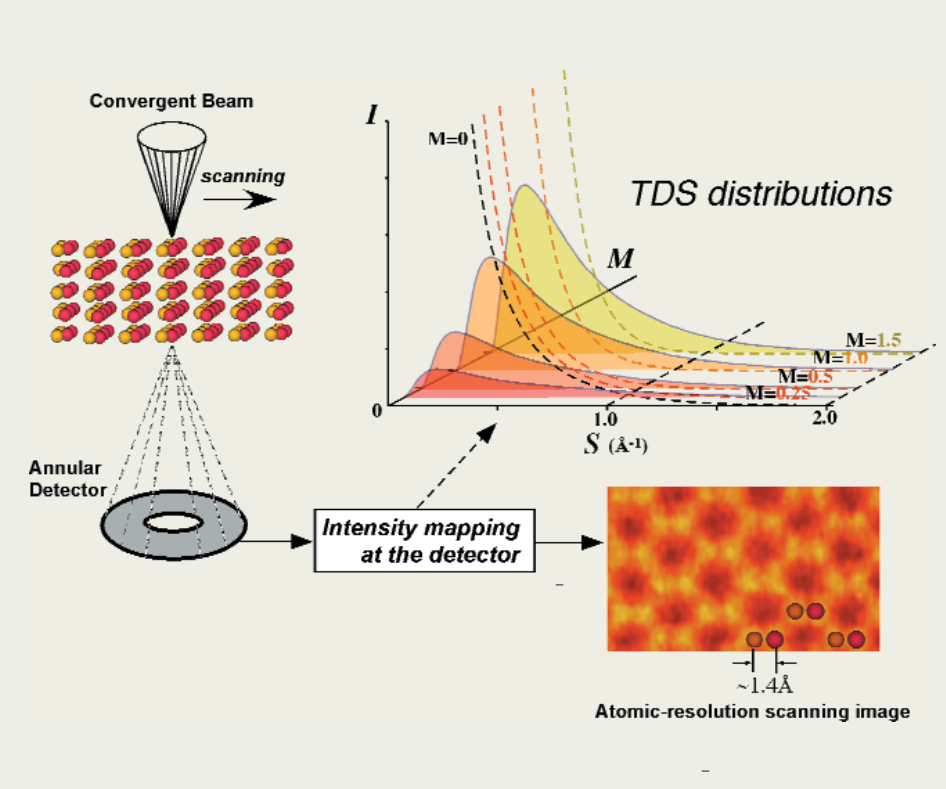

Fig. 1. Schematic drawing of atomic-resolution annular dark-field (ADF) imaging in a scanning transmission electron microscope (STEM). A practical resolution of ADF-STEM by JEOL-2010F (TEM/STEM compatible) can be ~1.4 Å, as demonstrated by the dumb-bell image of a GaAs structure. Intensity of electrons scattered at high angles is dominated by thermal diffuse scattering (TDS), which is described by an absorptive form factor, $f_{HA}(M, s)$. TDS distributions (an integrand in Eq. (2)) of an Al atom for several M values, calculated using the atomic form factor by Weickenmeier & Kohl [8], are shown at the upper-right hand side.

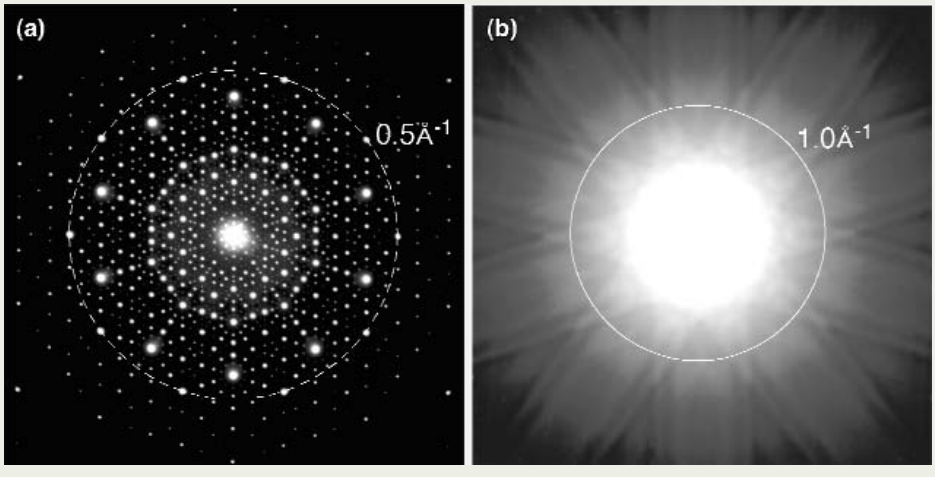

Fig. 2. (a) Parallel-beam and (b) convergent-beam electron diffraction patterns taken along the tenfold symmetry axis of the $Al_{72}Ni_{20}Co_8$ decagonal quasicrystal. A high-density of sharp diffraction spots appear in a low-angle scattering range ((a)), while the thermal diffuse scattering dominates at a high-angle region (> ~1 $Å^{-1}$, (b)).

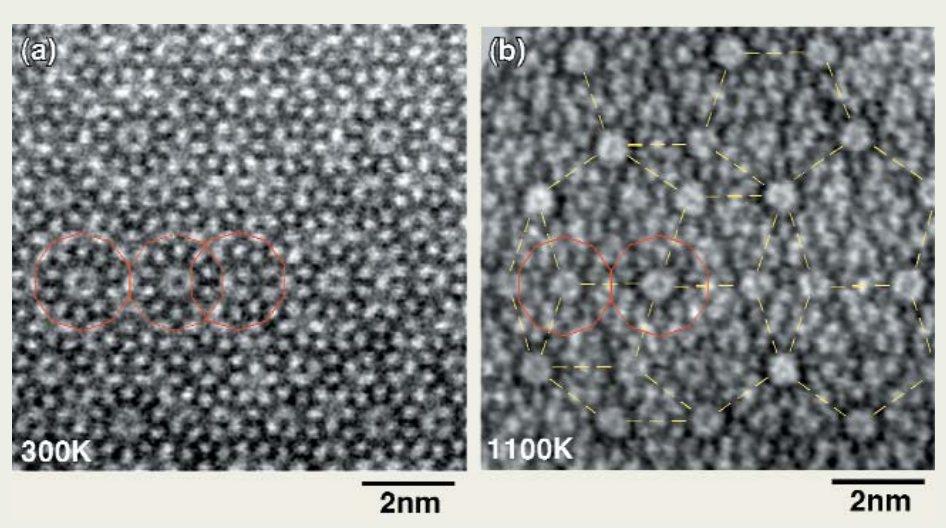

Fig. 3. ADF-STEM images of a decagonal $Al_{72}Ni_{20}Co_8$. These were taken at (a), 300K and (b), 1100K by collecting the electrons scattered at angles approximately between 45 and 100 mrad ($0.9 \leq s \leq 2.0$) with a 200kV-STEM (JEOL-2010F). The images were obtained, although not from the exactly same region, from the near-edge regions of the same cleavage-grain, so that the specimen thickness is comparable. Therefore, contrast differences between (a) and (b) are due to the different temperature not to changes in specimen thickness. By connecting the center of the decagonal clusters (red) that reveal significant temperature-dependent contrast change, pentagonal quasiperiodic lattice (yellow) can be drawn in (b).

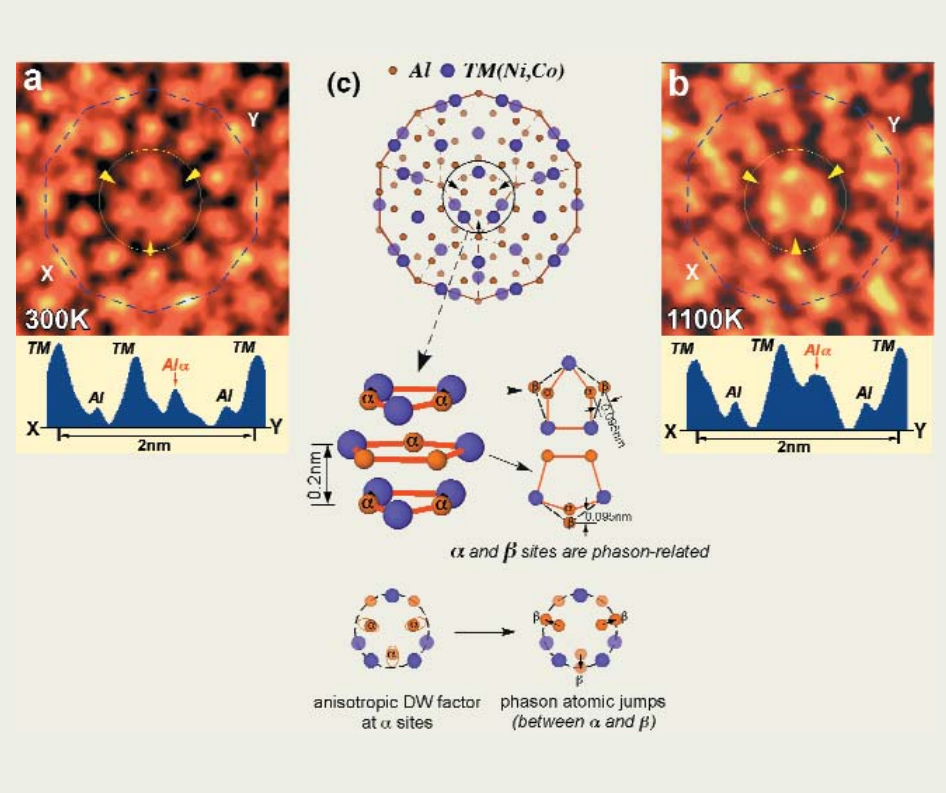

Fig. 4. A decagonal cluster with a diameter of about 2 nm, a structural unit of $Al_{72}Ni_{20}Co_8$. The clusters observed (a), at 300K and (b), 1100K, together with the corresponding line-profiles across X-Y. Significant contrast change occurs at the core of the cluster, particularly at the positions indicated by arrows, which correspond to the Alα sites denoted in the line-profiles. (c) Structural model of $Al_{72}Ni_{20}Co_8$ [6]. The structure has two distinct atomic layers stacked along the periodic c-axis; bold and semi-transparent dots denote the atoms at layers c=0 and c=1/2, respectively. Shown below is a pentagonal columnar atomic configuration around the center of the cluster. Phason-related α and β sites are on the quasiperiodic atomic plane, separated by approximately 0.095 nm. Possible anisotropy of the Debye-Waller factor of the Al atoms at the α sites and occurrence of atomic jumps into the β sites are described in the projected atomic positions, where the semitransparent atoms represent those at different level along the tenfold-axis.

through M_{phason} (Eq. (3)) – realized for the Alα atoms. An occurrence of DW factor anomalies at the Alα site is probably induced by the presence of the phason-flip atomic sites, denoted as β in Fig. 4 (c), which are separated by less than a typical interatomic distance. These α and β sites cannot be occupied simultaneously, and the β sites, considered to be energetically similar to the Alα site, could act as vacancies in providing an effective space for relaxation; it is very reasonable to assume that this causes a significant anisotropy in the DW factor, as illustrated in Fig. 4 (c), although the resolution of the present STEM (~1.5 Å) is not sufficient to reveal this anisotropic behavior. At high temperatures, occasional diffusion atomic jumps between the α and β sites are naturally expected (Fig. 4), causing phason-related structural disorders.

Summary

The present work demonstrates the additional capabilities of ADF-STEM – not only to provide Z-contrast, it can be used to detect a local thermal vibration anomaly in a solid by doing *in-situ* heating/cooling and/or the angle-resolved experiments. Further quantitative determination of the DW factor at each atomic site would be possible by comparing carefully the angle-dependent ADF-contrast change with the calculated intensity that includes both the elastic and TDS scatterings reaching the given angular range of the detector.

References

1. Pennycook, S. J. & Jesson, D. E. High-resolution Z-contrast imaging of crystals. *Ultramicroscopy* 37, 14--38 (1991); Atomic-resolution Z-contrast imaging of interfaces. *Acta metall. mater*. **40**, S149-S159.
2. Muller, D. A., Edward, B., Kirkland,E. J. & Silcox, J. Simulation of thermal diffuse scattering including a detailed phonon dispersion curve. *Ultramicroscopy* **86**, 371-380 (2001).
3. Abe, E, Pennycook, S. J. & Tsai, A. P. Direct observation of a local thermal vibration anomaly in a quasicrystal. *Nature* (London) **421**, 347-350 (2003).
4. Abe, E & Tsai, A.P. Structure of quasicrystals studied by atomic-resolution electron microscopy. *JEOL news* **36E**, 18 - 21 (2001).
5. Janssen, T. Crystallography of quasi-crystals. *Acta Crystallogr*. **A 42**, 261-271 (1986).
6. Abe, E. et al. Quasi-unit cell model for an Al-Ni-Co ideal quasicrystal based on clusters with broken tenfold symmetry. *Phys. Rev. Lett*. **84**, 4609-4612 (2000).
7. Takakura, H., Yamamoto, A. & Tsai, A. P. The structure of decagonal $Al_{72}Ni_{20}Co_8$ quasicrystal. *Acta Crystallogr*. **A 57**, 576-585 (2001).
8. Weickenmeier, A. & Kohl, H. Computation of absorptive form factors for high-energy electron diffraction. *Acta Crystallogr*. **A 47**, 590-597 (1991).

Cold-spray Ionization Mass Spectrometric Observation of Biomolecules in Solution

Kentaro Yamaguchi

Chemical Analysis Center, Chiba University

Investigations of the solution structures of primary biomolecules such as nucleosides, amino acids, sugars and lipids by using cold-spray ionization mass spectrometry (CSI–MS) are shown. Singly charged Na^+ adducts of large clusters (chain structures) for these biomolecules, presumably linked by non-covalent interactions, including hydrogen bonding and/or hydrophobic interactions were observed. Detailed DNA duplex observation using this method is also presented.

Introduction

Recently we reported a new ionization method, cold-spray ionization (CSI) [1], a variant of electrospray (ESI) [2] MS operating at low temperature, which allows facile and precise characterization of labile organic species. The optimum spray temperature is estimated to be around –20˚C. Generally, solvents show a higher dielectric constant at low temperature. This fact, as well as the solvation of the molecule, promotes electrolytic dissociation to form molecular ion in solution, because desolvation should not occur readily at such a low temperature. Therefore, it should be possible to detect extremely labile complexes without decomposition. The CSI apparatus has been refined and applied to characterize various kinds of organometallic compounds [3–4] and supramolecules [5–9]. Furthermore, CSI–MS revealed the dynamic assembling nature of coordination box type complexes [10].

This ionization method should also be applicable to biomolecules. In this report, we wish to describe solution structures including large-scale-aggregated chain structures of simple biomolecules such as nucleosides, amino acids, sugars and lipids observed by CSI–MS.

CSI–MS measurements were performed with a two-sector (BE) mass spectrometer (JMS-700, JEOL) equipped with the CSI source. Typical measurement conditions are as follows: acceleration voltage; 1.0 to 5.0 kV, needle voltage; 0 to 2.0 kV, needle current; 0 to 700 nA, orifice voltage; 60 to 100 V, ion source temp.; 5˚C, spray temp.; –20˚C, resolution (10% valley definition); 1000, sample flow rate; 17 μL/min, sample concentration; 1 mmol/L, solvent; H_2O: MeOH = 2:98.

1-33 Yayoi-cho, Inage-ku, Chiba 263-8522, Japan
e-mail: yamaguchi@cac.chiba-u.ac.jp

Chain Structure

Fig. 1 shows the CSI mass spectrum of thymidine (M1) in aqueous MeOH solution. Asymptotically reducing ion peaks, which appear to represent large-scale hydrogen-bonding aggregates, or chain structure, were observed up to around m/z 10000. The major ion peaks were assigned as $[nM1 + Na]^+$ (n = 1 to 41). The minor ion peaks located in the valleys between the major ion peaks in the spectra were assigned as doubly charged ions $[nM1 + 2Na]^{2+}$. X-ray crystallographic analysis of the nucleoside has clearly revealed a chain structure in the crystal, linked by hydrogen bonds [11]. In the case of another

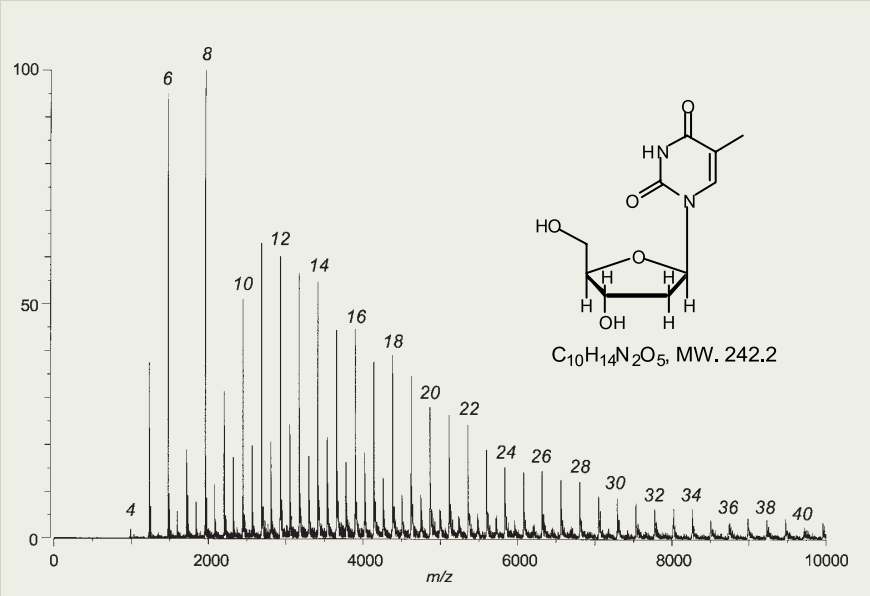

Fig. 1. CSI mass spectrum of thymidine (M1). Italic number: $[nM1 + Na]^+$.

nucleoside, 2'-deoxyguanosine, ions corresponding to quaternary aggregate structure, a G-quartet [12], were also observed together with chain structures.

Similar chain structures were also observed in amino acids. The CSI–MS spectrum of L-valine (M2) in solution is shown in **Fig. 2**. The major ion peaks were also assigned as $[nM2 + Na]^+$ (n = 1 to 42) together with doubly charged ions with in the range of m/z 0 to 5000. Other amino acids such as leucine, isoleucine, lysine and serine also exhibited similar mass spectra suggestive of large-scale-aggregated chain structures. X-ray crystallographic analysis of these amino acids has indicated presence of hydrogen-bonding chain structures in the crystal [13].

Characteristic chain structures of mono-saccharides were also clearly observed in solution. In the case of D-glucose (M3), ion peaks assigned to $[nM3 + Na]^+$ (n = 1 to 133), together with doubly charged ions, were clearly observed in the range of m/z 0 to 24000. (**Fig. 3**). The crystal structure of D-glucose is known to exhibit strong intermolecular hydrogen bonding [14]. Chain structures with different abundances of aggregation states were observed with other isomers.

Furthermore, the membrane structure of the L-α-phosphatidylcholine, dilauroyl (C12:0) (M4) lipid bilayer [15] was directly observed, preserving the hydrophobic intermolecular interactions, in solution by means of CSI–MS (**Fig. 4**). Ion peaks assigned as $[nM4 + Na]^+$ (n = 1 to 42), together with doubly charged ions, were clearly observed in the range of m/z 0 to 26000, the current limit of the mass spectrometer. Chain structure was also observed for steroids as well as other similar lipids and micelles.

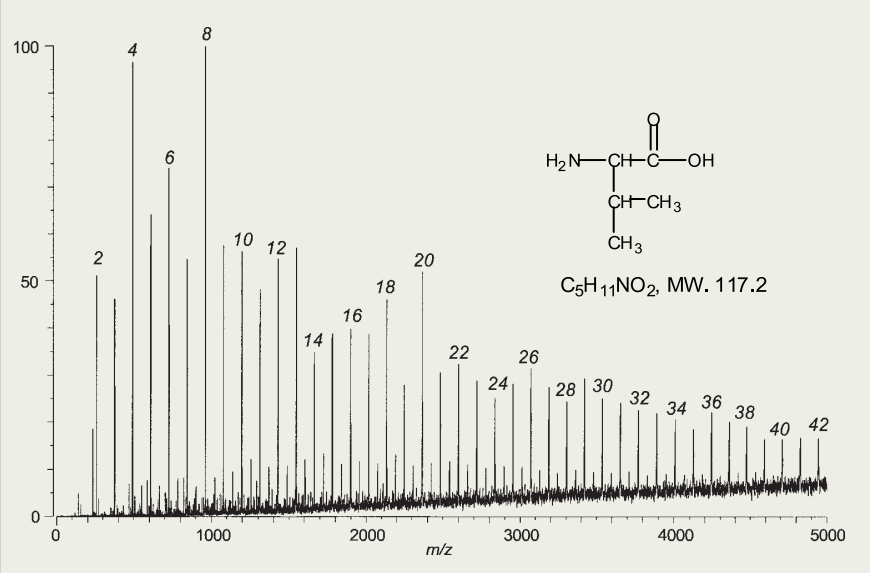

Fig. 2. CSI mass spectrum of L-valine (M2). Italic number: $[nM2 + Na]^+$.

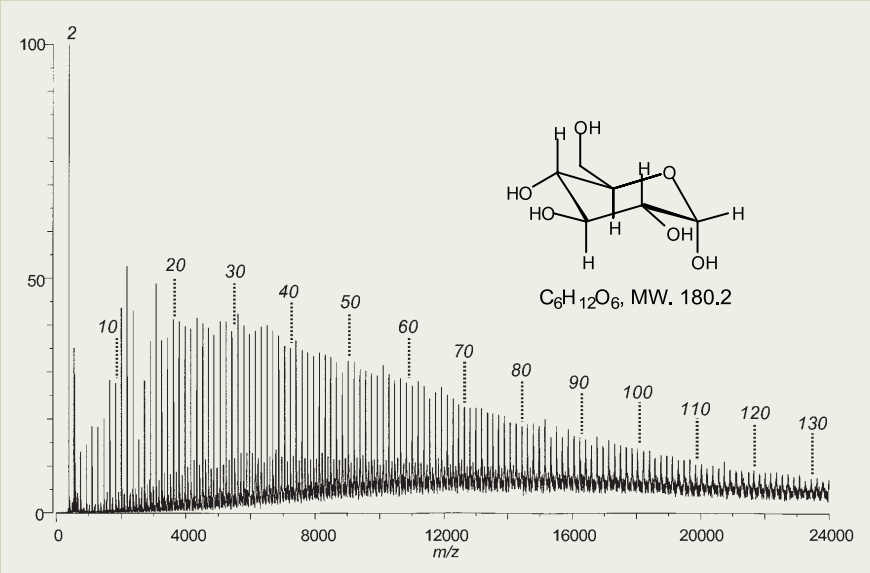

Fig. 3. CSI mass spectrum of D-glucose (M3). Italic number: $[nM3 + Na]^+$.

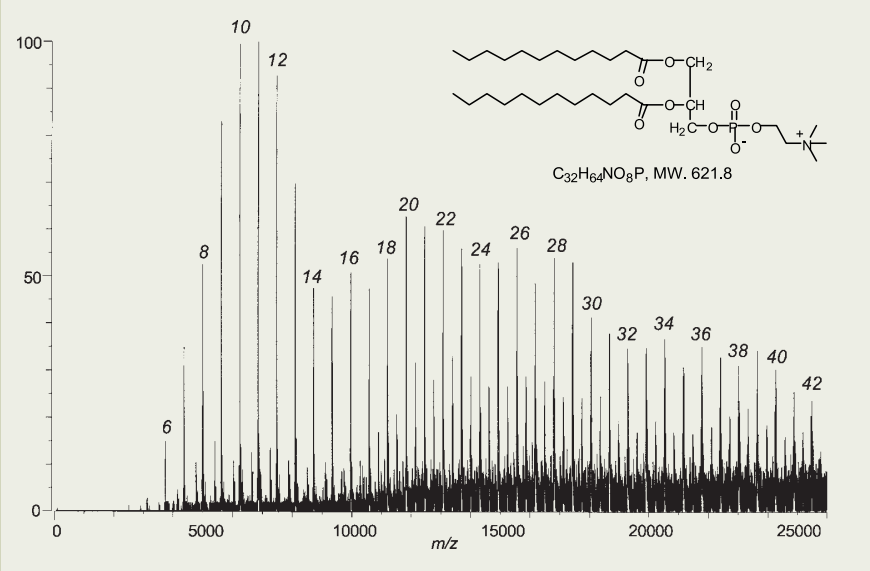

Fig. 4. CSI mass spectrum of L-α-phosphatidylcholine, dilauroyl (C12:0) (M4). Italic number: $[nM4 + Na]^+$.

DNA Duplex

Next subject is a facile and reliable analysis of double-stranded oligodeoxynucleotides that can detect precisely structures in which non-covalent bonding interactions are important, by means of cold-spray ionization mass spectrometry. In double-stranded DNA analysis, ion peaks of single-stranded oligonucleotide are always observed as a major component, together with the corresponding duplex, in gas phase by using ESI–MS. Further, non-covalent complexes of small (less than 10 base-pair) oligodeoxy-nucleotide-binding drugs are rather difficult to observe by the conventional method [16, 17]. This is because of the low melting temperature (Tm) of the hetero-duplex.

Negative CSI–MS measurements were performed with a two-sector (BE) mass spectrometer (JMS-700, JEOL) equipped with the CSI source [1]. Typical measurement conditions are as follows: acceleration voltage; –5.0 kV, needle voltage; –1.7 kV, orifice voltage; –100 to –60 V, ion source temperature; 15˚C, spray temperature; 7˚C, resolution (10% valley definition); 2000, sample flow rate; 8 μL/min, DNA concentration; 10 μM, buffer (NH_4OAc) concentration; 50 mM, solvent; H_2O: MeOH = 1:1.

Hetero-duplexes (5'-dA_nG_n-3') • (5'-dC_nT_n-3') ((A_nG_n) • (C_nT_n)) (n = 3 to 7), annealed by heating to 90°C for 10 min and slow cooling to room temperature (2 hr), were analyzed by CSI–MS. The estimated Tm_n (n = 3 to 7) values according to Wallace's theorem [18] were as follows. Tm_3 = 18, Tm_4 = 24, Tm_5 = 30, Tm_6 = 36 and Tm_7 = 42°C. The CSI–MS spectra of (A_3G_3) • (C_3T_3) and (A_4G_4) • (C_4T_4) at 7 °C (spray temperature) are shown in **Figures 5** and **6**, respectively, as examples.

Although ion peaks based on single strands (M_{ss}) were observed together with a major double-stranded (M_{ds}) nucleotide at m/z 1193 $[M_{ds}–3H]^{3–}$ ($M_{ds}^{3–}$) in the case of the 6-mer, a single major molecular ion peak of the duplex m/z 1203 $[M_{ds}–4H]^{4–}$ ($M_{ds}^{4–}$) was observed for the 8-mer. The corresponding duplex ion peaks of m/z 1512 $M_{ds}^{4–}$, m/z 1456 $M_{ds}^{5–}$ and m/z 1704 $M_{ds}^{5–}$ for the 10-, 12-, and 14-mer, respectively were also observed as the major species. The ion peaks of M_{ss} were the dominant species observed for these oligomers in conventional ESI–MS (not shown).

Furthermore, CSI–MS was applied to small oligodeoxynucleotides, 5'-dA_4C_4-3' (A_4C_4), 5'-dG_4T_4-3' (G_4T_4), 5'-dA_4G_4-3' (A_4G_4) and 5'-dC_4T_4-3' (C_4T_4). A clear ion peak m/z 1203 ($M_{ds}^{4–}$) due to the hetero duplex (A_4C_4)•(G_4T_4) and (A_4G_4)•(C_4T_4), was observed in the mixtures of (A_4C_4)(G_4T_4) and (A_4G_4)(C_4T_4), respectively. Although the ion peaks of each M_{ss} were mainly observed in the mixtures of (A_4C_4)(A_4G_4) and (G_4T_4)(C_4T_4), the mismatched duplexes, (A_4C_4)•(A_4G_4) m/z 1212 ($M_{ds}^{4–}$) and (G_4T_4)•(C_4T_4) m/z 1194 ($M_{ds}^{4–}$) were also observed in these mixtures. These are possibly based on C_4-G_4 Watson-Crick duplexes. The CSI–MS spectrum of the mixture (G_4T_4)(C_4T_4) is shown in **Figure 7**.

The ion due to the duplex was not observed in the (A_4C_4)(C_4T_4) and (G_4T_4)(A_4G_4) mixtures, presumably because of the lower affinity of A_4-T_4 duplex formation of the nucleotides having unfavorable mismatched sequences.

Finally, the mixture of all four oligodeoxynucleotides was analyzed. The CSI–MS spectrum of this mixture was quite simple. The ion peak m/z 1203 ($M_{ds}^{4–}$) based on the hetero duplexes (A_4C_4)•(G_4T_4) and (A_4G_4)•(C_4T_4), is the dominant species in the spectrum (**Figure 8**).

This confirms the remarkable molecular recognition ability of DNA, which interacts highly specifically with the most favorable bases in solution.

Thus, CSI–MS has revealed non-covalent clustering or aggregation of biomolecules in solution for the first time. In addition, various

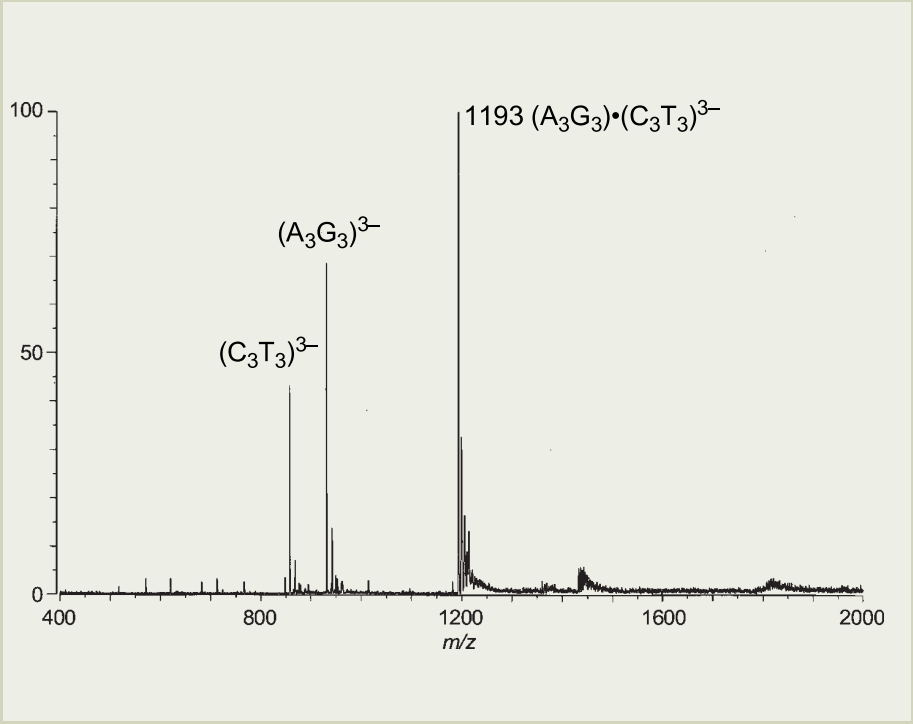

Fig. 5. Negative CSI mass spectrum of duplex (A_3G_3)•(C_3T_3).*

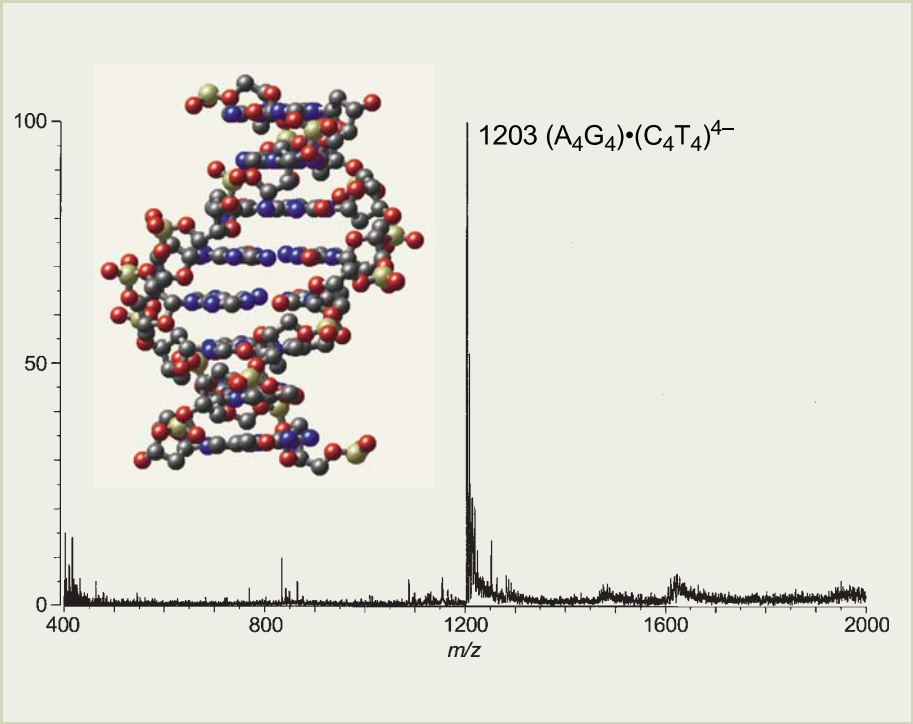

Fig.6. Negative CSI mass spectrum of duplex (A_4G_4)•(C_4T_4).*

complexes of oligodeoxynucleotides were observed by using CSI–MS. This method made it possible to observe very unstable species such as low Tm DNA duplexes which cannot be detectable by conventional ESI–MS. This method is remarkably effective to elucidate in detail the interactions of DNA complexes, being superior to other methods currently in use, such as UV melting methods. CSI–MS technique has many potential molecular-biological applications, including studies of dynamic interactions at very high resolution. The result shows the potential importance of this new MS technique for a wide variety of structural investigations in organic chemistry as well as biochemistry.

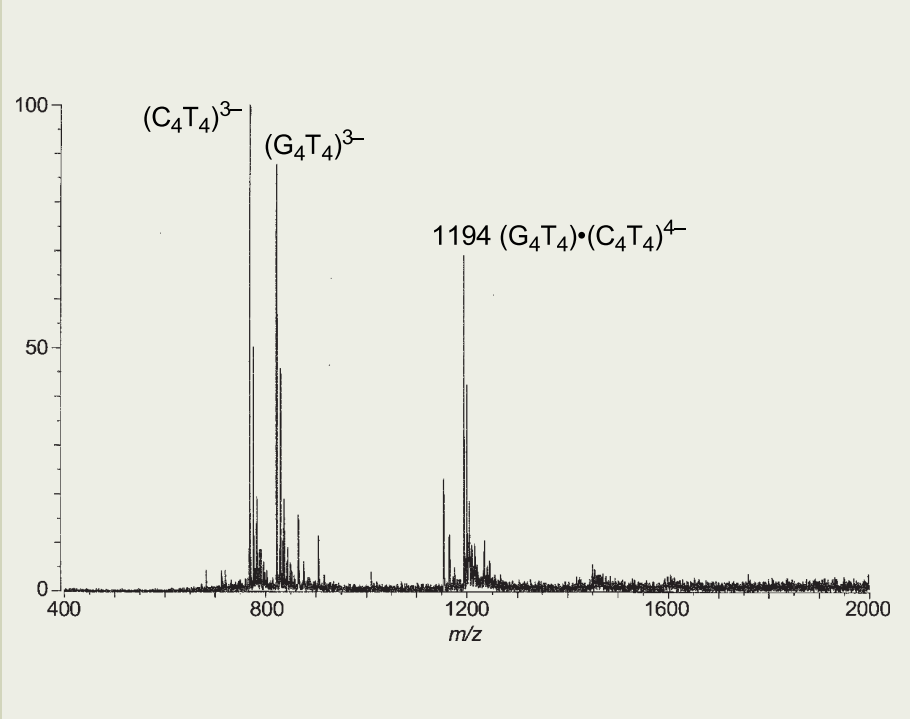

Fig. 7. Negative CSI mass spectrum of the mismatched duplex $(G_4T_4)•(C_4T_4)$.*

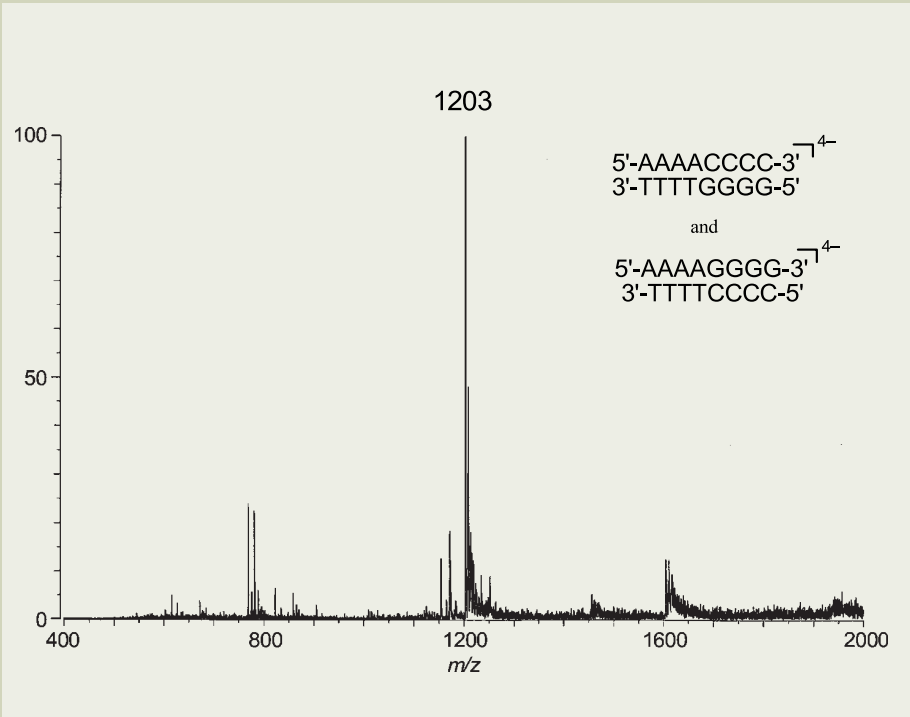

Fig. 8. Negative CSI mass spectrum of a mixture of four 8-mers; (A_4C_4), (G_4T_4), (A_4G_4) and (C_4T_4).*

References

1. (a) S. Sakamoto, M. Fujita, K. Kim and K. Yamaguchi, *Tetrahedron*, 2000, **56**, 955, and (b) K. Yamaguchi, *J. Mass Spectromet*., **38**, 473–490 (2003).
2. J. B. Fenn, M. Mann, K. Meng, S. F. Wong and C. M. Whitehouse, *Science* 1989, **246**, 64.
3. S. Sakamoto, T. Imamoto and K. Yamaguchi, *Org. Lett*., 2001, **3**, 1793.
4. T. Suzuki, N. Yamagiwa, Y. Matsuo, S. Sakamoto, K. Yamaguchi, M. Shibasaki and R. Noyori, *Tetrahedron Lett*., 2001, **42**, 4669.
5. Z. Zhong, A. Ikeda, M. Ayabe, S. Shinkai, S. Sakamoto and K. Yamaguchi, *J. Org. Chem*., 2001, **66**, 1002.
6. N. Fujita, K. Biradha, M. Fujita, S. Sakamoto and K. Yamaguchi, *Angew. Chem. Int. Ed*., 2001, **40**, 1718.
7. C. Dietrich-Buchecker, N. Geum, A. Hori, M. Fujita, S. Sakamoto, K. Yamaguchi and J.-P. Sauvage, *Chem. Commun.*, **2001**, 1182.
8. S. Sakamoto, M. Yashizawa, T. Kusukawa, M. Fujita and K. Yamaguchi, *Org. Lett.*, 2001, **3**, 1601.
9. A. Ikeda, H. Udzu, Z. Zhong, S. Shinkai, S. Sakamoto, and K. Yamaguchi, *J. Am. Chem. Soc*., 2001, **123**, 3872.
10. Y. Yamanoi, Y. Sakamoto, T. Kusukawa, M. Fujita, S. Sakamoto and K. Yamaguchi, *J. Am. Chem. Soc*., 2001, **123**, 980.
11. D. W. Young, P. Tollin and H. R. Wilson, *Acta Cryst*., 1969, **B25**, 1423.
12. J. L. Sessler, M. Sathiosatham, K. Doerr, V. Lynch and K. A. Abboud, *Angew. Chem. Int. Ed*., 2000, **39**, 1300.
13. K. Torii and Y. Iitaka, *Acta Cryst*., 1970, **B26**, 1317.
14. G. M. Brown and H. A. Levy, *Acta Cryst*., 1979, **B35**, 656.
15. R. M. Venable, Y. Zhang, B. J. Hardy and R. W. Pastor, *Science*, 1993, **262**, 223.
16. Reviews: (a) J. L. Beck, M. L. Colgrave, S. F. Ralph, M. M. Sheil, *Mass Spectrom. Rev*. 2001, **20**, 61; (b) S. A. Hofstadler, R. H. Griffey, *Chem. Rev*. 2001, **101**, 377.
17. (a) A. Kapur, J. L. Beck, M. M. Sheil, *Rapid Commun. Mass Spectrom*. 1999, **13**, 2489; (b) V. Gabelica, E. D. Pauw, F. Rosu, **J. Mass Spectrom**. 1999, **34**, 1328; (c) V. Gabelica, F. Rosu, C. Houssier, E. D. Pauw, *Rapid Commun. Mass Spectrom*. 2000, **14**, 464; (d) K. X. Wan, T. Shibue, M. L. Gross, *J. Am. Chem. Soc*. 2000, **122**, 300.
18. R. B. Wallace, J. Shaffer, R. F. Murphy, J. Bonner, T. Hirose, K. Itakura, K.;*Nucleic Acid Res*. 1979, **6**, 3543.
19. S. Sakamoto and K. Yamaguchi, *Tetrahedron Letters*, **44**, 3341–3344 (2003) .

* Reprinted from Tetrahedron Letters, 44, Sakamoto and Yamaguchi, "Low Tm DNA duplexes observed by cold-spray ionization mass spectrometry," pp 3341 - 3344, Copyright 2003, with permission from Elsevier.

Electron Spin Resonance (ESR) in Nanocarbon Research

Houjin Huang

Materials Laboratories, Sony Corporation

We present an overview of the research on Electron Spin Resonance (ESR) techniques as applied to nanocarbon materials. Through ESR measurements, various electronic and spintronic information about nanocarbon materials has been obtained, including the electronic spin structure of C_{60} anions, the electronic structure of endofullerenes, and defects and conduction electrons in carbon nanotubes. We believe that conventional and advanced ESR techniques, such as pulse ESR, will play an important role in the future nanocarbon research, including the exploration of device applications using the spins in nanocarbon materials.

Introduction

Nanometer scale carbon materials, called nanocarbon materials, including fullerenes and carbon nanotubes, have been a topic of considerable interest over the past decade. Various kinds of nanocarbon materials have been synthesized and characterized. Applications of these novel materials, such as to displays, electronics, spintronics, energy and medicines are currently under development [1-3]. Nanocarbon materials with new structures and properties continue to emerge.

Since the electronic structure of materials determines their physical and chemical properties, it is crucially important to investigate them and their change when undergoing physical and chemical processes. In the course of research on the structure and dynamics of nanocarbon materials, electron spin resonance (ESR) techniques have been widely used, and have also played a critical role in the discovery of new materials.

Here we briefly review ESR-involved nanocarbon research with an emphasis on recent advances in this field. Information derived from ESR signals is illustrated using various nanocarbon materials.

Electronic spin structure of C_{60} anions

It is well known that C_{60} readily accepts electrons to form anions due to its great electron affinity. Molecular solids of C_{60} anions (alkali, alkali-earth, or TDAE-doped) complexes show many interesting physical properties [4-5]. The key to understanding the properties of C_{60}-anion materials is the elucidation of the electronic spin structures associated with charge fluctuations and the splitting of the t_{1u} LUMO and t_{1g} NLUMO by *Jahn-Teller* distortions in successive levels of reduction. ESR techniques played a critical role in this research.

There have been many ESR studies on C_{60}^{-} (doublet), C_{60}^{2-} (triplet or singlet) and C_{60}^{3-} anions (quartet or doublet) [6-10]. For example, in order to observe the polyanionic high-spin states of C_{60}, Shohoji et al. reduced C_{60} with potassium and observed the ESR signals [11]. In the first reduction step, a superimposed ESR spectrum of the doublet state of C_{60}^{1-} and the triplet sate of C_{60}^{2-} was observed. Further reduction gave a mixed ESR spectrum of a dianionic triplet state and a trianionic quartet, in addition to the doublet-state spectrum. Continuing reduction yielded a quartet-state fine-structure ESR spectrum of C_{60}^{3-} dominating the triplet signal, as shown in **Fig. 1**. The quartet state spectrum was reproduced by spectral simulation with the same spin Hamiltonian parameters. Spin state transitions and the *Jahn-Teller* distortion effect have also been investigated using temperature-dependent ESR spectroscopy and 2D-electron spin transient nutation spectroscopy, respectively [11].

Electronic structure of endofullerenes

Since many endohedral fullerenes (or endofullerenes, as shown in **Fig. 2**) have unpaired electron spins located on host cages and/or on entrapped atoms, ESR techniques are particularly useful in detection and illustration of their electronic structure.

Endohedral metallofullerenes

A variety of endohedral metallofullerenes has been synthesized (mainly using arc discharge) and purified by HPLC. Also, a considerable variety of ESR spectra of lanthanum fullerenes has been obtained [12].

Figure 3 shows the ESR spectra of CS_2 extract of arc-generated soot and HPLC-isolated isomers. The ESR spectrum (a) of the extract can be regarded as the superimposed spectra of (b) for isomer I and (c) for isomer II. There are several important features in the spectra. First, for both isomers, isotropic 8 lines with equal intensity are obtained at room temperature, which corresponds to hyperfine coupling (hfc) with La nucleus I=7/2. Second, the satellite structures, as seen in the spectra for both isomers, are observed, which are due to the hfc with ^{13}C nuclear on fullerene cages. Third, the hfc constants for both isomers are very small but show different values (0.116 mT for isomer I and 0.0836 mT for isomer II). Considering the very large nuclear magneton of La, the splitting was extraordinarily small. Such small hfc constants can only be explained in reference to the unpaired spins located on fullerene cages [12-14].

The peaks of the eight lines of La@C_{82} are no longer equal when ESR measurements are performed at low temperature [14]. At 170 K, the spectrum shows a fishbone-like pattern. The peak intensity decreases and the line width broadens with an increase in the quantum number of the La nuclear spin. The anisotropic nature of La@C_{82} cannot be observed at room temperature. These phenomena (also found in other metallofullerenes such as Sc@C_{82}) can be interpreted in terms of the well-defined hydrodynamic theory, and the anisotropy of the ESR parameters are deduced from an analysis of the spectral pattern [15]. From this analysis, 97.6% of spin density is found to be located on the fullerene cage, while the remaining percent is suited on the $5dz^2$ orbital of the La nucleus. Thus La@C_{82} can be

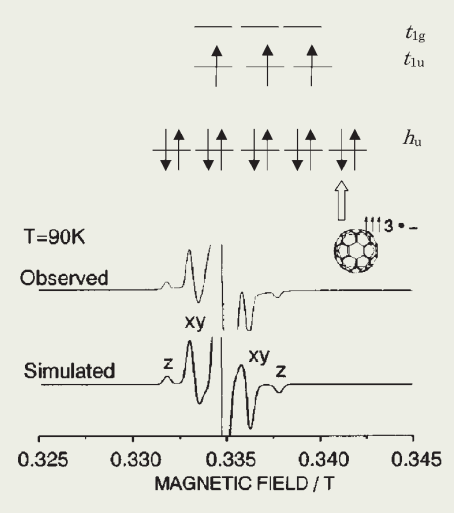

Fig. 1. X-band observed and simulated quartet-state ESR fine-structure spectra from C_{60}^{3-} fullerene at 90K. Spin Hamiltonian Parameters, S=3/2, g=2.0025, $|D|$=0.0014 cm^{-1}, and E=0 cm^{-1}. X, Y, Z denote the canonical absorption peaks. The schematic molecular orbital structure of C_{60}^{3-} is illustrated at the top of this figure.

2-1-1 Shinsakuragaoka, Hodogaya,
Yokohama, Kanagawa 240-0036, Japan
E-mail: houjin.huang@jp.sony.com

described as La^{3+} @C_{82}^{3-}.

In contrast to the obvious splittings of the endofullerenes encapsulated with La, Sc, and Y, ESR observations of the hyperfine splittings of other lanthanide metallofullerenes, such as Ce@C_{82}, Gd@C_{82} and Lu@C_{82}, are much more difficult because of additional spins from 4f orbitals. We have obtained X-band ESR spectra of Gd@C_{82}, Tb@C_{82}, and Lu@C_{82} at room temperature and liquid-nitrogen temperature. A single broad peak was observed. At liquid-nitrogen temperature, the peak is deformed, presumably due to the motional effects of anisotropic interactions of the spin systems, leading to an m_I dependence of the peak width [16-18]. Kato et al. recently succeeded in observing the weak spin fine structure of Gd@C_{82} at 1.5K using conventional X-band ESR. The unsymmetrical fine structure was further simplified using W-band ESR [19].

Group-V endofullerenes

Among the endofullerenes, group-V atom-encapsulated C_{60} (N@C_{60} and P@C_{60}) attract particular attention due to the atomic nature of the entrapped atoms that possess half-filled p orbitals ($^4S_{3/2}$ ground states) [20-21]. Potential applications, such as to quantum computation, have been proposed [22]. Because of the difficulties in their production, up to now ESR has essentially been the only method used to detect and investigate these kinds of materials.

Murphy et al. for the first time investigated nitrogen-implanted solid C_{60} using Q-band (ν ~ 35 GHz) and and X-band (ν ~ 9.4 GHz) ESR and found that atom-like nitrogen was encapsulated inside the C_{60} cage [20]. ESR spectra showed three very sharp lines that had never been previously observed in other nitrogen-containing paramagnetic species. The disintegration behavior of N@C_{60}, N@C_{70}, and P@C_{60} was also recorded using ESR measurements. The results show that decomposition of N@C_{60} occurs around 500K while N@C_{70} (~440K) and P@C_{60} (~400K) survive at lower temperatures [23].

Electron nuclear double resonance (ENDOR) spectra of N@C_{60} have also been observed, indicating that the hyperfine interaction is purely isotropic. ENDOR measurements not only confirm the presence of one nitrogen nucleus in the paramagnetic center, but they are also be able to determine the electronic spin to be S = 3/2, meaning that there is no bonding between nitrogen and the C_{60} cage [20].

Pulse ESR is indispensable to study the spin relaxation behavior of N@C_{60} [24-29]. Knapp et al. first measured spin-lattice relaxation time T_1 of a N@C_{60} solution with a π-π/2 pulse sequence, and obtained the value of $T_1 \cong 120$ µs [24]. The exceptionally long spin relaxation time confirms that the molecule can be viewed as a chemical realization of a nearly perfect trap without electron transfer between the entrapped element and the C_{60} cage. Pulse ESR studies also lead to the conclusion that solvent collision-induced deformations of the carbon shell which modulate the zero-field-splitting sensed by the quartet spin state of the molecule are the dominant spin relaxation mechanism. Pulse ESR and ENDOR studies of N@C_{60} embedded in a solid matrix such as crystalline C_{60} further confirm the nearly perfect de-coupling of the encased quartet spin from the carbon cage [24-25]. The degrading of symmetry induced by cage modification or phase transition of the matrices can be easily detected by the appearance of a zero-field splitting of axial symmetry, since the quartet electronic spin of the encapsulated N-atoms is very sensitive to the cage structure and its surroundings [27-29].

In order to produce the endofullerenes efficiently, we have developed a method based on rf-plasma for large-scale production of N@C_{60} [30]. A gram-scale deposit containing the same level of dopants can be obtained in less than an hour instead of days using ion-bombardment method. **Fig. 4a** shows an ESR spectrum of the product. Two sets of splittings, each consisting of three equally spaced lines but of different sharpness, are clearly visible. The hyperfine constant (hfc, 0.567 mT) is attributed to the isotropic hyperfine interaction of the ^{14}N unpaired electron spins with the nucleus spin. The splitting with the larger peak-to-peak width of ~18 µT is caused by the formation of polymers containing N@C_{60}, while the splitting with the peak-to-peak width of ~2 µT originates from pristine N@C_{60}, as is shown in **Fig. 4b**. The rf-plasma-generated product has also been investigated using pulse ESR. Similar to the findings with cw-ESR, pulse ESR also shows some differences between our sample and that producing by ion implantation [31].

Table 1 gives a summary of the ESR parameters of some well-studied endofullerenes. Unpaired spin (s) are located on fullerene cages for metallofullerenes, while they are confined in the atomic orbitals for group-V endofullerenes. Even though there are fundamental differences between these two kind of endofullerenes, it can be seen that the g-values of the electron spins of all endofullerenes are around 2.0, indicating that there is a very small contribution from orbital angu-

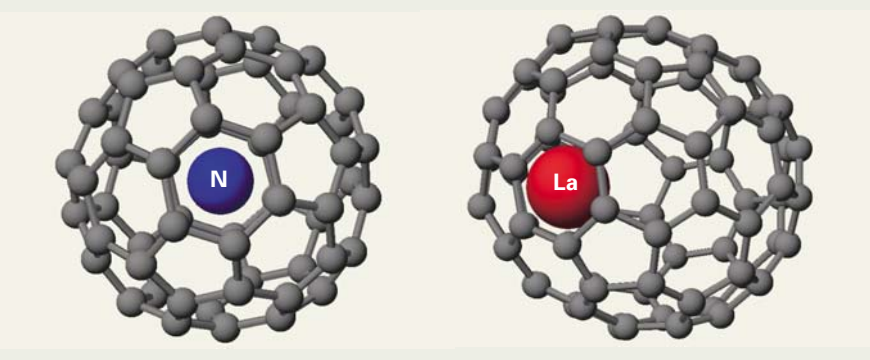

Fig. 2. Structural models for N@C_{60} and La@C_{82} (C_{2v}). The ESR active spins are located on the nitrogen atom and C_{82} cage for N@C_{60} and La@C_{82}, respectively. There is also a notable difference in the location of encapsulated elements inside their cages.

Table 1. X-band ESR parameters for various endofullerenes[a]

Species	hfc/mT	*g*-value[b]	*ΔHpp*/µT	T_1/µs	T_2/µs
Sc@C_{82} (I)	0.382	1.9999	3.6 (300 K)		
Sc@C_{82} (II)	0.116	2.0002	1.9 (300 K)		
Y@C_{82} (I)	0.048	2.0004	8.7 (300 K)		
Y@C_{82} (II)	0.034	2.0002	12.0 (300 K)		
La@C_{82} (I)	0.120	2.0008	4.9 (300 K)		
La@C_{82} (II)	0.083	2.0002	5.2 (220 K)		
^{14}N@C_{60}	0.566	2.0030	0.1 (300K)	120	50
^{14}N@C_{70}	0.539	2.0030	0.1 (300K)	125	30

[a] T_1 and T_2 are measured at room temperature in toluene.
[b] g-value of ^{15}N@C_{70} is smaller than that of ^{14}N@C_{60} by 0.000038.

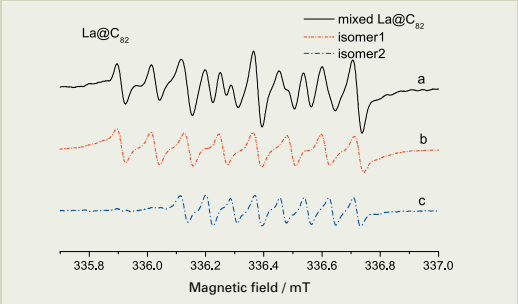

Fig. 3. ESR spectra of (a) CS_2 extract of soot containing La@C_{82}; (b) La@C_{82} (I), the major isomer (hfc = 1.159 G); (c) La@C_{82} (II), a minor isomer (hfc = 0.836 G).

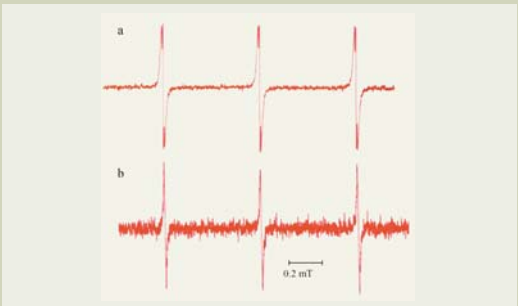

Fig. 4. X-band ESR spectra of a mixture of N@C_{60} and its polymers (a), and N@C_{60} after removal of the polymers (b). The triplet splitting is due to the hyperfine interaction with ^{14}N nucleus (I=1). Both spectra are observed at room temperature with a modulation width of 3 µT. The solvent is CS_2.

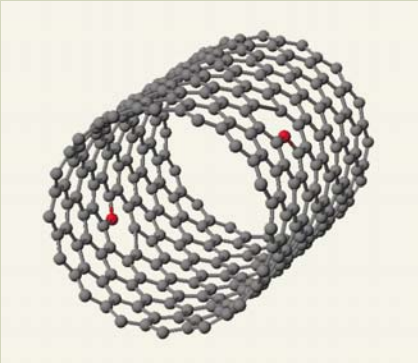

Fig. 5. A view of one single-walled carbon nanotube showing the presence of defects.

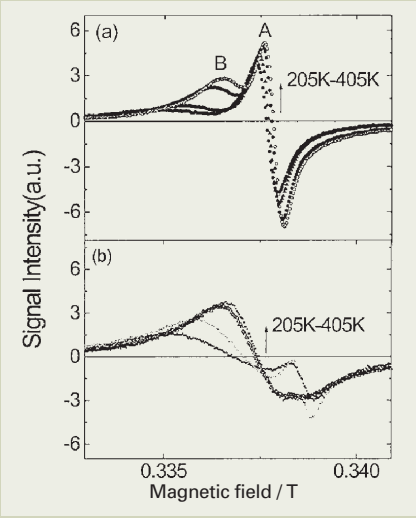

Fig. 6. Temperature dependence of ESR spectra for MWNTs. The resonance signal shows a Dysonian shape and corresponds to the typical signal due to conduction electrons: (a) as-grown CNTs and (b) purified and annealed sample, respectively.

lar moment, *L*, to the Zeeman states. Besides, these endofullerenes are considerably stable at room temperature and in air, which is different from the usual behavior of most organic free radicals.

The homogenous line width of $N@C_{60}$ as determined by spin-echo experiments is found to be of the order of 0.1 μT, which is at least a factor of ten narrower than any ESR line observed for radicals in a solution [24]. It is also notable that the relaxation times of nitrogen endofullerenes are extremely long, which does not apply to conventional free radicals, whose relaxation times are usually in the order of sub-microseconds or less.

Defects and conduction electrons in carbon nanotubes

Carbon nanotubes (CNTs) can be thought of as graphitic sheets with a hexagonal lattice that have been wrapped up into a seamless cylinder. Their intriguing helicity and diameter-dependent electronic conductivity has sparked intensive research, aiming at realizing molecular-level electronics and other applications [32]. The synthesized CNTs, however, are usually far from perfection, as is shown in **Fig. 5** [33]. The purification process may also introduce defects on CNTs [34]. In order to clarify the electronic structure of CNTs including defect states, as well as their effect on transport properties, ESR is regarded as a powerful tool.

Zhou et al. first reported a very weak ESR signal for an unpurified carbon nanotube with a g-value of 2.000 [33]. Kosaka et al. suggested that the as-grown nanotubes have many defects that can be annealed at high temperature to obtain ESR results very different from graphite [34-35]. The annealed CNTs show conduction ESR signals indicating the presence of metallic and/or narrow-band gap semiconducting CNTs.

The effect of annealing can also be seen by comparing the intensity and g-value dependence of the conduction ESR peaks for CNTs experiencing purification or annealing processes, as shown in **Fig. 6**. At room temperature, the ESR spectrum for the unpurified sample is clearly composed of two signals, a narrow signal A and a broad signal B. Signal B decreased continuously when the temperature decreased and became very small at 125K, while signal A was still observable at low temperature. Signal A disappears after annealing (730K), and thus may be related to the resonance centers in amorphous carbon particles and defects in the tubes.

Signal B produced by a conduction spin system has been observed from both MWNTs and SWNTs [34-38]. The g-value and line width of this signal gradually increase after thermal annealing [39]. This indicates an increase of carrier concentration in the CNTs which are metallic conductors. The conductivity of well-annealed CNTs is much higher than that of poorly annealed CNTs in two terminal resistance measurements, which is consistent with ESR observations.

Looking to the future

There are many other applications of ESR techniques in nanocarbon research, such as light-induced reactions of C_{60}-based materials [40-41], structural phase transitions in fullerides [42], and magnetic interactions in carbon nanostructures [43]. It is believed that ESR and its related techniques will continue to play an important role in nanocarbon research, including device applications using spins in these materials.

References

1. P. J. F. Harries.: *Carbon Nanotubes and Related Structures: New Materials for the 21th century*, (Cambridge U. P.), (1999).
2. R. H. Baughman et al.: *Science*, **297** 787 (2002).
3. T. Akasaka et al.: *Endofullerenes -A New Family of Carbon Clusters, Development in Fullerene Science*, vol 3, (Kluwer Academic), (2002).
4. K. Tanigaki et al.: *Nature*, **352** 222 (1991).
5. P. M. Allemand et al.: *Science*, **253** 301 (1991).
6. D. Dubois et al.: *J. Am. Chem. Soc*., **113** 4364 (1991).: *J. Am. Chem. Soc.*, **114** 6446 (1992).
7 M. Baumgarten et al.: *Adv. Mater.*, **5** 458 (1993).
8. M. M. Khaled et al.: *J. Am. Chem. Soc.*, **116** 3465 (1994).
9. P. C. Trulove et al.: *J. Am. Chem. Soc.*, **117** 6265 (1995).
10. P. D. W. Boyd et al.: *J. Am. Chem. Soc.*, **117** 2907 (1995).
11. M. C. B. L. Shohoji et al.: *J. Am. Chem. Soc.*, **122** 2962 (2000).
12. H. Shinohara: *Rep. Prog. Phys.*, **63** 843 (2000).
13. S. Suzuki et al.: *J. Phys. Chem.*, **96** 7159 (1992).
14. S. Okubo, T. Kato, in *Nanonetwork Materials, ed.* by S. Saito et al., (American Institute of Physics), (2001).
15. T. Kato et al.: *J. Phys. Chem.* **97** 13425 (1993).
16. H. Huang et al.: *J. Phys. Chem*. **B 104** 1473 (2000).
17. H. Huang et al.: *J. Phys. Chem. Solid*, **61** 1105 (2000).
18. H. Huang et al.: in *Physics and Chemistry of Nanostructures*, ed by Shihe Yang and Ping Shen (1999).
19. T. Kato et al.: *IMS Anneal Review*, (2001 and 2002).
20. T. A. Murphy, et al.: *Phys. Rev. Lett*., **77** 1075 (1996).
21. H. Mauser et al.: *Angew. Chem., Int. Ed. Engl*., **36** 2835 (1997).
22. W. Harneit, Phys. Rev. **A 65** 032322 (2002).
23. M. Waiblinger et al.: *Phys. Rev*. **B 64** 159901 2001.
24. C. Knapp et al.: *Chem. Phys. Lett*., **272** 433 (1997).
25. N. Weiden et al.: *J. Phys. Chem*., **103** 9826 (1999).
26. E. Dietel et al.*: J. Am Chem. Soc*., **121** 2432 (1999).
27. K. P. Dinse et al.: *Carbon*, **38** 1635 (2000).
28. N. Weiden et al.: *Phys. Rev. Lett*., **85** 1544 (2000).
29. P. Jakes et al.: *J. Mag. Reson*., **156** 303 (2002).
30. H. Huang, M. Ata and M. Ramm.: *Chem. Commn*., **18** 2076 (2002).
31. H. Huang et al., to be published.
32. R. H. Baughman et al.: *Science*, **297** 787 (2002).
33. O. Zhou et al.: *Science*, **263** 1744 (1994).
34. M. Kosaka et al.: *Chem. Phys. Lett*., **225** 161 (1994).
35. M. Kosaka et al.: *Chem. Phys. Lett*., **233** 47 (1995).
36. S. Bandow et al.: *Appl. Phys*. **A 67** 23 (1998).
37. P. Petit et al.: *Phys. Rev*. **B 56** 9275 (1997).
38. Y. Lee et al.: *J. Electrochem. Soc*., **147** 3564 (2000).
39. S. Ishii et al.: *Phys*. **E 17** 386 (2003).
40. K. Hasharoni et al.: *J. Am. Chem. Soc*., **119** 11128 (1997).
41. E. Sartori et al.: *J. Phys. Chem.*, **A 105** 10776 (2001).
42. C. Coulon et al.: *Phys. Rev. Lett*., **86** 4346 (2001).
43. C. Goze-Bac et al.: *Carbon*, **40** 1825 (2002).

Analysis of Cadmium (Cd) in Plastic Using X-ray Fluorescence Spectroscopy

Hiroshi Onodera

Application & Research Center, JEOL Ltd.

Introduction

In recent years, mass media have focused on the topics of the environment and environmental conservation. With the advancement in scientific technology, resource development has progressed, and the developed resources have yielded a great deal of useful products that have enriched human life. However, environmental destruction has become serious due to the secondary destruction caused by the development of resources as well as the primary destruction that has originated from untidy disposal of these products. As a result of this disposal, toxic chemical substances were dissolved in soil and rivers, and permeated groundwater and animals and plants over a long time. Consequently, human beings, at the top of the ecological food chain, are suffering from health disturbances from these substances. In this context, the European Union (EU) adopted restrictions such as WEEE (Waste Electrical and Electronic Equipment) and RoHS (Restrictions on Hazardous Substances), which specify hazardous substances. Based on these regulations, the specific hazardous materials (lead, mercury, cadmium, hexavalent chromium, PBB and PBDE) are subject to usage restrictions in Europe.

We carried out analyses of inorganic components such as lead (Pb), mercury (Hg) and cadmium (Cd), using the energy-dispersive X-ray fluorescence spectrometer (EDXRF). In this paper, we report on the analysis results of Cd at low concentration (5 to 50 ppm) in plastic, which is a focus of recent attention.

Analytical Methods and Instrument

Energy-dispersive X-ray fluorescence spectroscopy

Energy-dispersive X-ray fluorescence spectroscopy is an element analysis method using X-rays. In this method, X-rays irradiate the sample and the fluorescent X-rays generated from the sample are analyzed. It is possible to identify elements from the energies (keV) of the measured spectra, and also to obtain the concentrations (mass%) of the identified elements from the intensities of the spectral peaks. The spectrometer can generally detect elements ranging from Na to U. The spectrometer can also be equipped with a special detector for the analysis of elements lighter than Na.

The spectrometer features a maintenance-free optical system. That is, the optical system is a simple one with no drive system, where all components such as the X-ray tube and detector are fixed, requiring no adjustment. In addition, since there is no need for sample pre-treatment such as surface polishing or evaporation, it is possible to perform nondestructive analysis that facilitates repeated analysis and makes sample preservation easy. The spectrometer can also perform measurement in the air, thus making it possible to analyze any samples irrespective of their states, for example, even when the sample is liquid or a paste-like substance.

Features of the instrument (JSX-3202EV Element Analyzer)

We used an energy-dispersive X-ray fluorescence spectrometer (EDXRF), the JSX-3202 EV Element Analyzer (**Fig. 1**). This spectrometer is a high-performance instrument that incorporates a high-resolution detector (energy resolution: 149 eV guaranteed) and a high-

Fig. 1. External view of the JSX-3202EV.
Large-stage configuration (290 mm diameter×150 mm high).

Detectable elements	Na to U
X-ray generator	
Tube voltage	5 to 50 kV
Maximum tube current	1 mA
Maximum load	50 W
Target	Rh
X-ray irradiation area	About 16 mm diameter
Detector	Si (Li) semiconductor
Resolution	149 eV
Liquid nitrogen (LN_2)	3 L
LN_2 consumption	1 L/day (supplied only before analysis)
Sample chamber	
Chamber size	150 mm (diameter)× 100 mm (H)
Sample environment	Air, vacuum (optional)

Main specifications of the JSX-3202EV.

brightness X-ray tube with a Rh target. The Rh tube can generate high-intensity continuous X-rays in the high-energy range, making it effective for the excitation of X-rays (K lines) from heavy metallic elements such as Cd. Although the characteristic X-rays (Rh Kβ 2 line) scattered from the Rh tube overlap the fluorescent X-rays from Cd, this phenomenon can be suppressed by the use of the newly developed X-ray filter. (A detailed explanation is presented in the next section.)

In an ordinary usage of this instrument, the X-rays irradiate the sample surface through a collimator 7 mm in diameter. Five other kinds of collimators are also available (4.0, 2.0, 1.0, 0.8, 0.3 mm in diameter). When using the 7 mm collimator, the X-ray irradiation area on the standard surface of the measurement position becomes an ellipse (major axis: about 16 mm, minor axis: about 13 mm). The effective detection thickness (the penetration depth of the irradiation X-ray beam) is 1 cm or a little more when the beam axis is perpendicular to the sample surface. In the optical system of the JSX-3202EV, since the incident angle of the X-ray beam is about 45 degrees to the sample, the effective detection thickness is 5.0 to 5.5 mm. When quantitative analysis is performed, in order to avoid the change of the spectral intensity depending on the sample thickness, it is necessary to prepare a pellet that is thicker than the effective detection thickness, or to make the sample thickness uniform (having no surface irregularity) even for a thin film.

Filter for Cd

When measuring the relatively thick samples such as plastic, using the Rh tube, two problems arise in the detection of spectral peaks. One problem is the background. This background considerably increases toward the range of the high-energy end, which makes the confirmation of the spectra of trace elements difficult. Another problem is the characteristic X-rays scattered from the Rh tube. These characteristic X-rays overlap the fluorescent X-rays generated from palladium (Pd), silver (Ag) and cadmium (Cd). In order to suppress these phenomena, we developed a special filter. This filter is attached between the X-ray tube and the sample. It cuts two kinds of X-rays from the X-ray beam: Rh characteristic X-rays and the continuous X-rays in the energy range lower than Cd absorption edge. Thus, this new filter can reduce the background near the Cd Kα line, enhancing the detection sensitivity.

Figure 2 shows the effectiveness of the filter when acrylic resin is used as a sample. In Fig. 2, four spectra are shown for comparison. When zirconium (Zr) or molybdenum (Mo) is used for an X-ray filter, the background and the the Rh scattering lines (particularly the Kβ 2 line) cannot be suppressed to a satisfactory level. In contrast, the newly developed filter sufficiently reduces both the background and the Rh scattering lines.

This filter cuts only the X-rays with energies lower than Cd absorption edge, which do not contribute to the excitation of Cd Kα. In addition, when using this filter, the continuous X-ray intensity in the high-energy range is higher than the intensity when a Zr filter or a Mo filter is used. This X-ray filter is therefore effective for the analysis of Cd.

Experiment : Analysis of Trace Cd

Sampling in X-ray fluorescence spectroscopy

In qualitative analysis or simple quantitative analysis using X-ray fluorescence spectroscopy, the sample can be measured without any careful treatment for sampling. However, when high-precision quantitative analysis is required, it is necessary to carry out careful sampling so that stable spectral intensities can be obtained irrespective of the state of the sample. In order to make a good sample, the sample's surface roughness, area and thickness should be uniform while paying attention to segregation in the sample and the sample's density. To this end, generally, powder samples and samples with various shapes (areas, thicknesses) are pressed into pellets.

Samples and sampling method

In this experiment, we used a polyvinyl chloride (PVC) power cable. A power cable contains resin. The insulation wires in the cable are composed of soft resin, and the plug and socket consist of hard resin.

Cd contained in PVC has functioned as a stabilization agent for many years. Although Cd has been recycled, this is still used for power cables. **Figure 3** shows a power cable used in the present experiment and various samples for each part of the cable. Sampling was performed to the insulation wires, connector and socket.

Insulation material for electrical wires

The black insulator contains three thin wires,

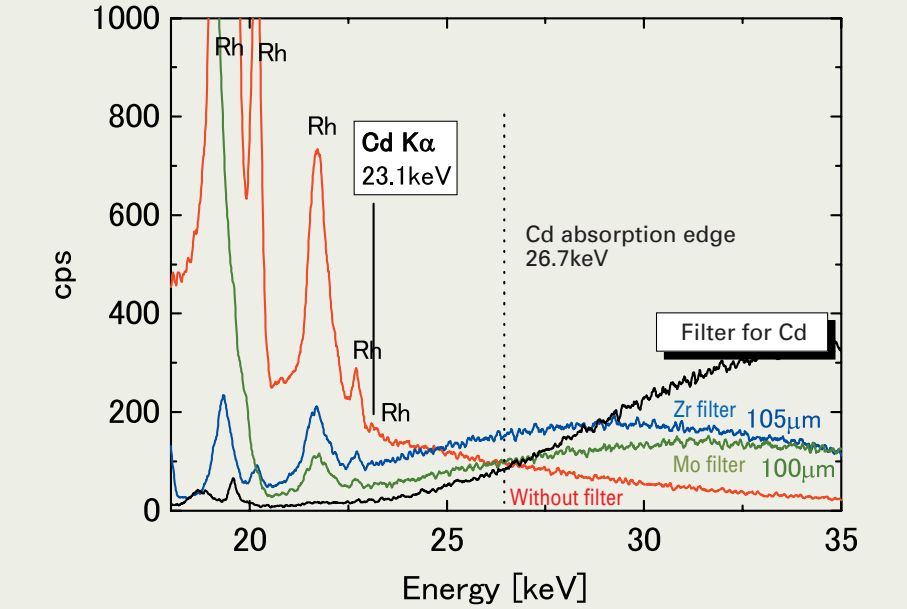

Fig. 2. Effectiveness of filter for Cd.
(Tube voltage: 50 kV, specimen environment: air, sample: acrylic resin)

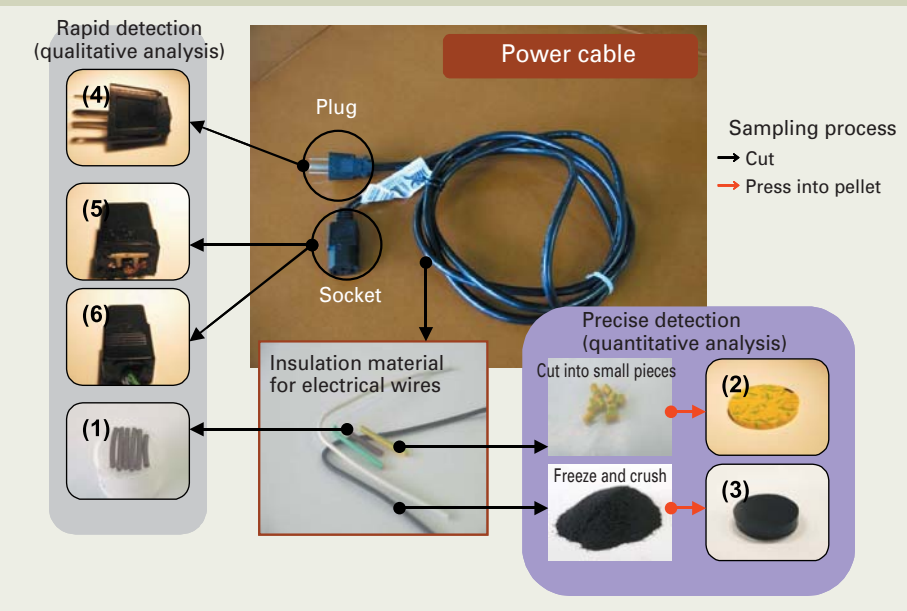

Fig.3. Samples and sampling for each part of a power cable.

and these insulation materials were sampled. The metal wires were removed from the wires.
(Sample 1) Insulation material was cut into several tubes and arranged on the sample holder.
Size of one tube: 2.5 mm outside diameter, 1.0 mm inside diameter. Sampling time: 2 minutes.
(Sample 2) Insulation material cut into small pieces was pressed into a pellet by using a heating press.
Sampling time: 5 minutes for cutting, 15 minutes for heating press.
(Sample 3) Insulation material cut into small pieces was frozen in liquid nitrogen, crushed using a crushing machine, and pressed into a pellet using a heating press. **Figure 4** shows a Retsch Corporation's ZM100 centrifugal crushing machine and a sample crushed using this machine.
Sampling time: 5 minutes for cutting, 5 minutes for freezing and crushing, 15 minutes for heating press.

When rapid identification of Cd is required, sampling shown as (1) in Fig. 3 is applicable. However, in quantitative analysis or the detection of trace Cd on the order of ppm, sampling (2) or (3) is effective.

Connector and socket

Samples (4) to (6) in Fig. 3 were cut from the cord and measured without sampling. Since these samples have sufficiently large area and flat surfaces with little surface irregularity, they can be used for not only rapid analysis but also high-precision analysis. However, some samples may have insulation materials with insufficient thickness. Therefore, when analysis precision has high priority, careful attention is needed.

Cd concentrations in the six samples are (Sample 1) 11 ppm, (Sample 2) <2 ppm, (Sample 3) 7 ppm, (Sample 4) 18 ppm, (Sample 5) 22 ppm, (Sample 6) 44 ppm. These values were obtained by inductively coupled plasma (ICP) chemical analysis at Analysis Center Co., Ltd.

Basic unit.

Insulation material (Cd concentration: 11 ppm) crushed by the machine.

Fig. 4. Centrifugal crushing machine ZM100.

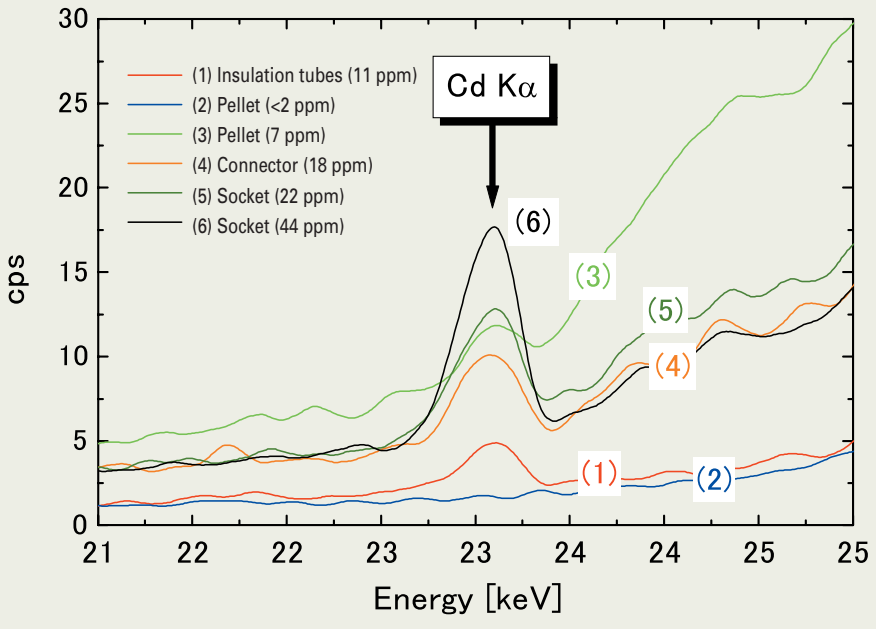

Fig. 5. Cd spectra obtained from six samples.
(Tube voltage: 50 kV, specimen environment: air, accumulation time: 5 minutes)

Analysis results of samples

Figure 5 shows the spectra of the six samples obtained using the filter for Cd. Smoothing was carried out for 15 points using the Savitsky-Golay method. The spectra of low-concentration Cd were obtained from all of the samples irrespective of the shape of the sample.

Differences in background are observed in the spectra. The probable reason for this is that the concentration of antimony (Sb), whose spectral peak appears at energies higher than the Cd spectral peak, are different in the six samples, and that this difference influences the intensities of the background in the six spectra.

In the spectrum of Sample 1, it is found that both the intensities of the spectral peak of Cd Kα and the background are low. It may be interpreted that these phenomena are caused by the influence of not only the matrix element concentrations but also the sample thickness, which is smaller than those of the other samples.

Investigation of Sampling for Effectively Detecting Cd

In order to effectively detect Cd, we investigated how to place the sample and to carry out sampling. Sample 1 (insulation tubes with Cd concentration of 11 ppm) was used for investigating the sample orientation, sample area and sample thickness.

Sample orientation

The X-rays irradiate the sample surface in an elliptical region (with longer length than width), seen from the direction that is parallel to the axis of the X-ray beam. Taking this phenomenon into consideration, we predicted that the intensity of the spectral peak would be different in the case when the sample is placed parallel to the X-ray axis and perpendicular to the axis, because the X-ray irradiation area is different in the two cases.

Figure 6 (a) shows the sample and the sample orientation, and **Fig. 6 (b)** shows the Cd spectra of the sample with two different orientations. Although the difference in intensity is small, it was confirmed that the spectrum shows higher intensity when the sample was placed parallel to the axis of the X-ray beam. We found from this result that it is effective to place the sample parallel to the beam axis, which corresponds to the major axis of the elliptical region on the sample. This effect becomes noticeable for the sample area smaller than the X-ray irradiation area and also for the sample that is small and elongated.

Sample area

We investigated the correlation between the sample area and the intensity of the Cd spectrum by changing the number of insulation

tubes from one to four. **Figure 6 (c)** shows the insulation tubes arranged on the holder and **Fig. 6 (d)** shows the Cd spectra obtained from different numbers of the arranged tubes. As the number of tubes increases, the intensity of the spectral peak also increases. However, it is found that when the number becomes four or more, the intensity is no longer influenced by the number of tubes. This is interpreted as the sample area being larger than the X-ray irradiation area.

It should be noted that if the gaps between tubes are large, the intensity does not reach saturation even for the sample with a sufficiently large area. Thus, in order to obtain a spectrum with high intensity, it is necessary to arrange the tubes without gaps.

Sample thickness

We investigated the difference in spectral intensity for various sample thicknesses. We changed the thickness by stacking the insulation tubes on the holder and by preparing the pellets with different thicknesses. As mentioned earlier, since the effective detection thickness of the X-ray beam in the optical system of the JSX-3202EV is 5.0 to 5.5 mm, we stacked up to three insulation tubes.

Figure 6 (e) shows the insulation tubes stacked on the holder and **Fig. 6 (f)** shows the Cd spectra obtained from different numbers of the stacked tubes. Also, in **Fig. 6 (g)**, the pel-

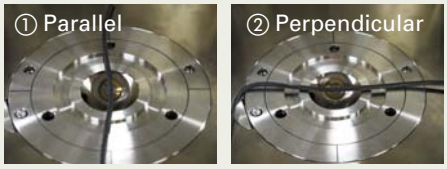

Fig. 6 (a) Measured sample with different orientations.

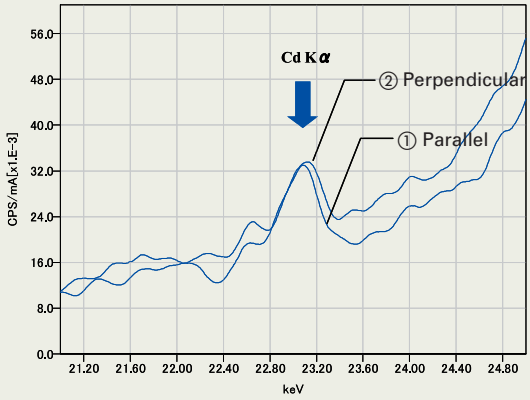

Fig. 6 (b) Cd spectra obtained from the sample with different orientations.
(Tube voltage: 50 kV, specimen environment: air, accumulation time: 15 minutes)

Fig. 6. (c) Measured samples (tubes) arranged on the holder.

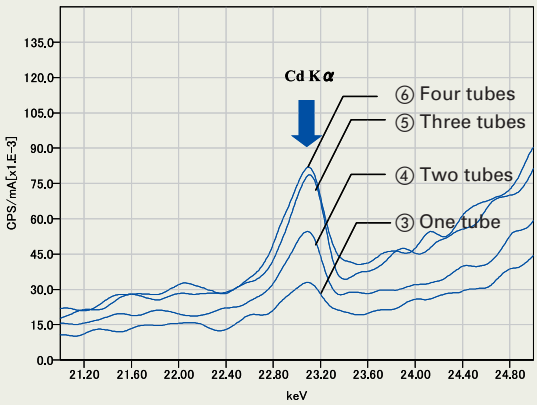

Fig. 6 (d) Cd spectra obtained from different numbers of arranged insulation tubes.
(Tube voltage: 50 kV, specimen environment: air, accumulation time: 15 minutes)

Fig. 6 (e) Measured samples (tubes) stacked on the holder.

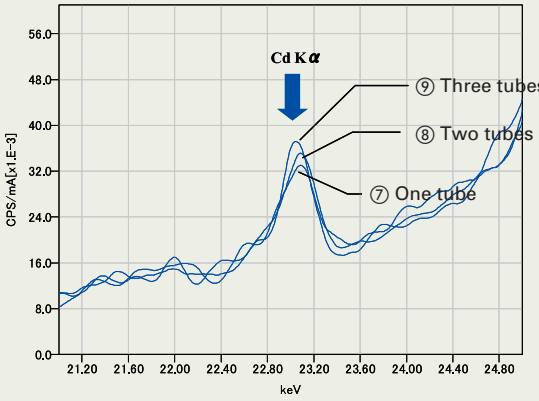

Fig. 6 (f) Cd spectra obtained from different numbers of stacked tubes.
(Tube voltage: 50 kV, specimen environment: air, accumulation time: 15 minutes)

Fig. 6 (g) Measured samples (pellets) with different thicknesses.

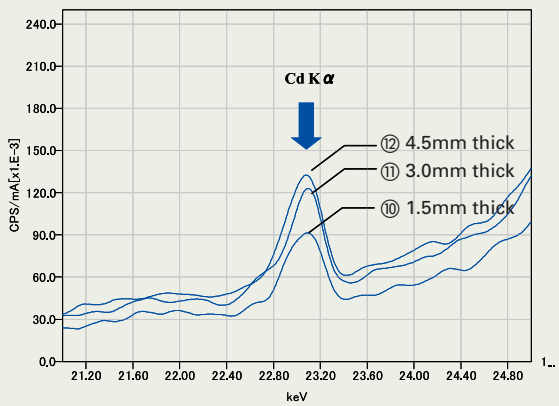

Fig. 6 (h) Cd spectra obtained from the pellets with different thicknesses.
(Tube voltage: 50 kV, specimen environment: air, accumulation time: 15 minutes)

Fig. 6.

lets of insulation material with different thicknesses are shown, and in **Fig. 6 (h)**, the Cd spectra of these pellets are presented. Thicker samples have higher spectral intensity. This phenomenon is more noticeable for the pellet samples because the pellet has an area larger than that of the stacked tubes. Also, in case of the insulation tubes, the increase in spectral intensity is small even when two or more tubes are stacked, because there are gaps between the tubes.

Figure 6 (i) shows the Cd spectral intensities obtained in the experiments that were presented in Figs. 6 (b), 6 (d), 6 (f) and 6 (h). High intensities were obtained from the pellets, particularly from the thicker ones. In case of the insulation tubes, the arranged tubes show higher intensities than that obtained from the stacked ones.

When quantitative analysis is performed, it is necessary to prepare a pellet with sufficiently large thickness or to make a sample with uniform thickness (without surface irregularities).

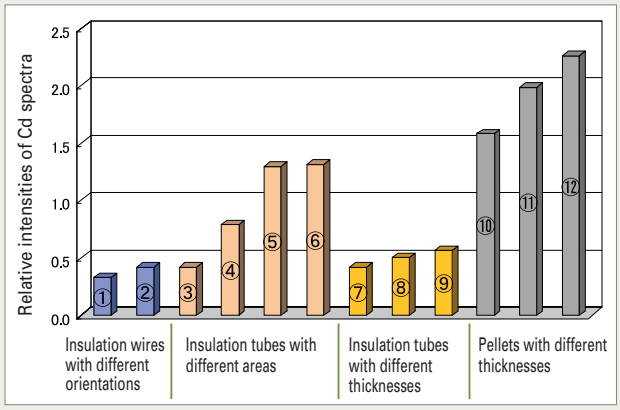

Fig. 6 (i) Cd spectral intensities for different sampling.

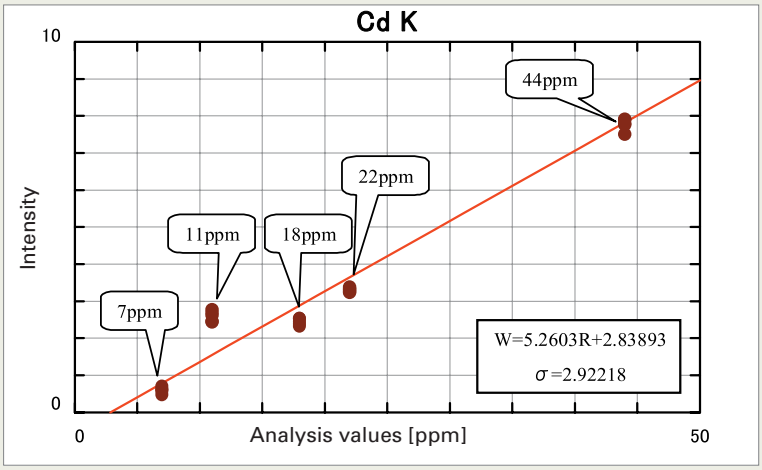

Fig. 7 (a) Calibration curve of Cd spectra (first-order).
Cd concentration range for calibration curve: 7 to 44 ppm.

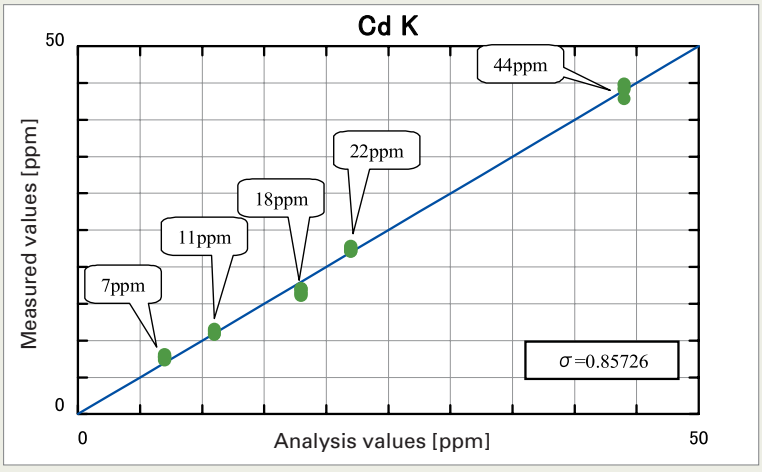

Fig. 7 (b) Calibration curve of Cd spectra (with matrix effect correction for Pb).
Cd concentration range for calibration curve: 7 to 44 ppm.

Fig. 7.

Investigation of Calibration Curves

We investigated a calibration curve of Cd spectra obtained from five pellet samples. Cd concentrations of these samples were 7 ppm, 11 ppm, 18 ppm, 22 ppm and 44 ppm, which were precisely determined by ICP analysis. Measurement was carried out in the air, using the filter for Cd. Tube voltage at 50 kV and a collimator 7.0 mm in diameter were used.

Smoothing was carried out for the obtained spectra, and we calculated the intensities of the Cd spectra by removing the background with the ROI (region of interest) being 22.87 to 23.36 keV. **Figure 7 (a)** shows the created calibration curve. In this curve, although the correlation between Cd concentrations obtained by ICP analysis and the Cd spectral intensities is accurate, the intensity of 11 ppm Cd is a little higher than that of 18 ppm Cd.

In this experiment, each sample contains Pb and Sb in addition to Cd. Since Cd Kα is absorbed by Pb and Sb, the intensity of the Cd spectrum changes, depending on the concentrations of Pb and Sb.

It should be noted that when the Cd spectrum is subjected to smoothing, the reproducibility of the spectral shape deteriorates as the spectral peak intensity decreases; therefore, it is necessary to carefully determine the ROI and the background range.

Figure 7 (b) shows the calibration curve that includes the correction for the absorption by Pb, whose mass absorption coefficient is assumed to be constant. That is, variations in the Cd spectral intensities, which depend on Pb concentrations, were corrected in the calibration curve. (This correction is called the matrix effect correction.) We obtained the Pb spectra to detect Pb concentrations in the samples, and carried out the correction by using the measured concentrations of Pb.

Conclusions

We carried out analyses of Cd at low concentration in polyvinyl chloride (PVC) samples, using a JSX-3202EV energy-dispersive X-ray fluorescence spectrometer, which is equipped with a newly developed filter for Cd. The filter, incorporated in the spectrometer, proved to be effective for detecting low-concentration Cd in the PVC samples with various shapes (areas, thicknesses). In addition, the Cd spectral intensities in this experiment showed a linear relationship with Cd concentrations measured by ICP chemical analysis.

Our future task is to investigate the matrix effect that decreases the Cd spectral intensity, and to create more detailed calibration curves that can be applied to the analysis of bulk samples with sufficiently large area and thickness. When this task is completed, we will investigate a method that allows quantitative analysis of Cd, by which Cd spectra can be obtained even from one insulation wire without cumbersome sampling (pressing the wire into pellet).

We will also continue to carry out the analyses of Pb and Hg, which are specified as hazardous substances in the EU regulations, for more precisely determining the concentrations of these elements.

JWS-3000 High Resolution Review SEM

Mitsuo Suga, Akira Takishita, Shigemasa Ohta, Manabu Saito and Kunihiko Uchida

Semiconductor Equipment Division, JEOL Ltd.

Introduction

A review SEM is a scanning electron microscope (SEM) used for observing defects and surface shape of semiconductor devices. This SEM has various features: It can be installed in a semiconductor clean room and can observe wafers without cleaving them. It can navigate to defect coordinate positions obtained by defect-inspection systems using light or an electron beam. In recent years, it is equipped with an Auto Defect Review (ADR) function.

The JWS-3000 is a high-performance review SEM that can observe the entire surface of 200 mm and 300 mm wafers, tilted up to 45°. **Figure 1** is an external view of the JWS-3000. The features of the JWS-3000 are described below.

Fig. 1. External view of the JWS-3000.

Features of Instrument

High resolution observation

As shrinkage of semiconductor devices progresses, users of review SEMs demand higher resolution. The JWS-3000 incorporates a newly designed strong-excitation conical objective lens that is based on a semi-in-lens used for a field-emission (FE) SEM. In addition, a bias voltage up to −1.5 kV can be applied to the substrate (in Super Fine mode). These improvements achieve a high resolution of 3 nm at an accelerating voltage of 1 kV. **Figure 2** shows comparative images of contact holes at an accelerating voltage of 1 kV, taken with a conventional instrument, the JWS-8755S (Fig. 2 (a)) and the JWS-3000 (Fig. 2 (b)). The resolution of the JWS-8755S is 5 nm at 1 kV, but inferior to 3 nm achieved with the JWS-3000. Figure 2 (b) clearly shows a more highly resolved contact-hole image than Fig. 2 (a). The JWS-3000 also affords high-resolution observation even when a wafer is tilted (see **Figs. 3** and **4)**.

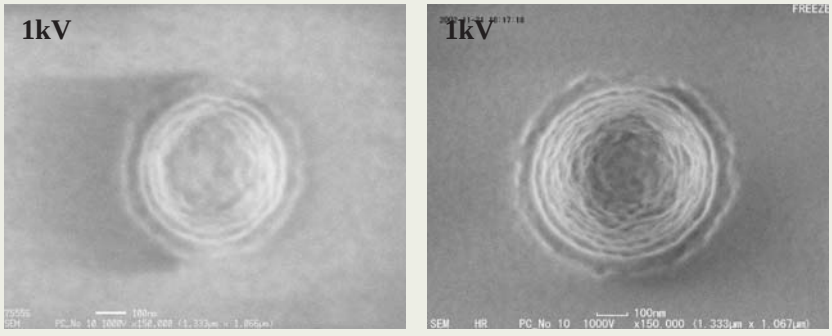

(a) Image of a contact hole taken with the JWS-8755S. (conventional instrument)

(b) Image of a contact hole taken with the JWS-3000.

Fig. 2. High resolution SEM images taken with a conventional instrument and with the JWS-3000.

Since resists and low-k materials on wafers are damaged by a high-accelerating-voltage

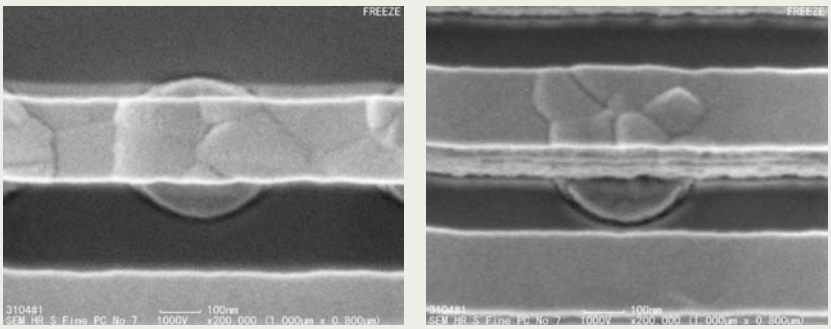

a) Tilt angle: 0° (b) Tilt angle: 15°

Fig. 3. High resolution SEM images obtained using the JWS-3000, with the wafer tilted. Surface-shape observation of a side wall of etching patterns.

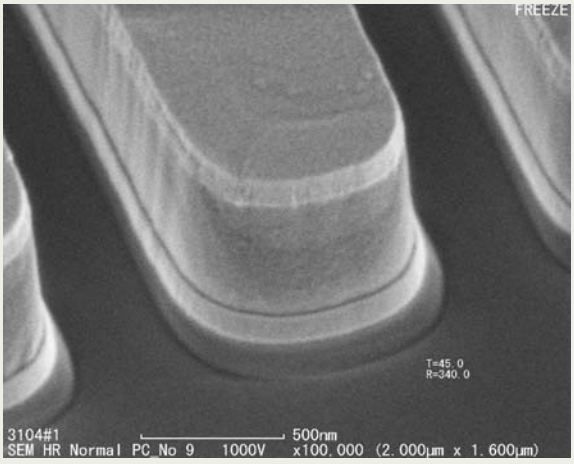

Tilt angle: 45°

Fig. 4. High resolution SEM image obtained using the JWS-3000, with the wafer tilted.

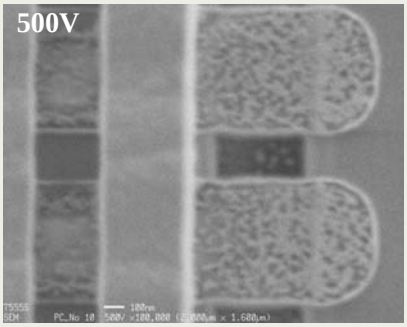

(a) Image taken with the JWS-8755S (conventional instrument).

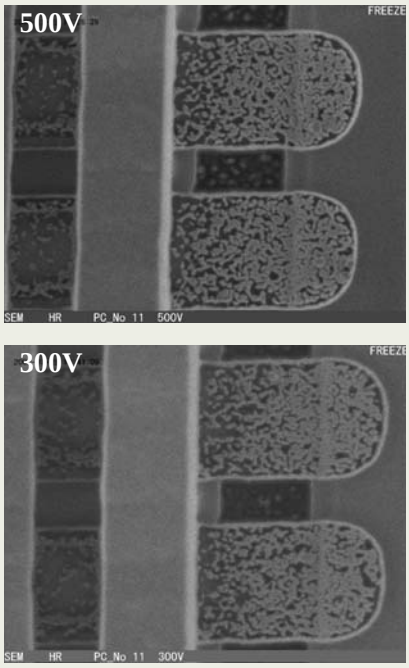

(b) Images taken with the JWS-3000.

Fig. 5. Low-accelerating-voltage SEM images taken with a conventional instrument and with the JWS-3000.

electron beam, users of review SEMs demand low-accelerating-voltage observation. **Figure 5** shows that the JWS-3000 can provide high resolution at low accelerating voltages, compared with conventional instruments. In conventional SEMs, resolution deteriorates when the accelerating voltage is low (Fig. 5 (a)). In the JWS-3000, Super Fine mode allows observation with relatively high resolution even at low accelerating voltages (Fig. 5 (b)). The JWS-3000 can reduce the accelerating voltage down to 100 V.

Improved ADR and automatic functions

The JWS-3000 has an improved ADR function. In order to detect defects even on flat samples using the ADR function, the Auto Focus function has been enhanced (Fine Auto Focus). Auto Focus using image processing and a wafer-height sensor make ADR possible even for samples on which focusing is difficult (see **Fig. 6**). That is, wafers subjected to chemical mechanical polishing (CMP) and bare silicon (Si) wafers can be easily focused for ADR analysis. In addition, improvements to the stage and image acquisition expand the defect-review throughput up to 900 DPH (defects per hour) or more (when a JEOL standard sample is used).

Imaging of height information on defects

In high-accuracy classification of defects, height information on defects is sometimes useful. For this purpose, it is valuable to carry out tilt observation, or to acquire SEM images showing “shadows” of defects using multiple detectors. The JWS-3000 can perform both tilt observation and acquisition of shadow images. Tilt observation has conventionally been carried out manually, because automatic observation provided insufficient accuracy of stage positioning and took a long time to

correct wafer position along with stage tilt. In contrast, the JWS-3000 has an improved stage-positioning accuracy for tilt observation, which is achieved by correcting the stage-stop position using the height information on the wafer surface. This improvement makes tilt ADR analysis easy (**Fig. 7**).

Furthermore, for the acquisition of shadow images, the JWS-3000 incorporates two detectors (right and left) inside the objective lens. These detectors selectively detect electrons emitted in the oblique directions, enabling the JWS-3000 to obtain shadow images (see **Fig. 8**). Since the length of a shadow depends on the height of the defect, the shadow image offers height information on defects.

Imaging of simple electrical defects

Review SEMs can observe not only defects in shape but also simple electrical defects. If a semiconductor device has a simple electrical defect, when a wafer is illuminated with an electron beam, a voltage difference arises on the wafer surface and this difference is detected as a voltage contrast. **Figure 9** shows comparative voltage-contrast images of a wafer on which contacts are buried, taken with the JWS-3000. Figure 9 (a) is an image obtained using the left detector, and Fig. 9 (b) shows an image obtained using the upper detector. Since the upper detector of the JWS-3000 is sensitive to the sample potential, Fig. 9 (b) demonstrates that simple electrical defects can be detected by means of the upper detector. This detector is also suitable for observation of the bottoms of contact holes (see **Fig. 10**).

Employment of new systems

The JWS-3000 employs a graphical user interface system that runs on a PC (see **Fig. 11**). New features such as a recipe wizard are introduced, making instrument operation easy. The JWS-3000 also adopts a system that supports remote operation. Using this system, users can control the instrument from outside of a clean room.

Summary

We have briefly explained the JWS-3000 high resolution review SEM. This review SEM achieves high resolution at low accelerating voltages by the employment of a newly designed electron optical system. This instrument also has improved automatic-observation functions in addition to the highly regarded manual observation of the JWS series. The JWS-3000, incorporating many new features presented in this paper, will be expected to play an important role in defect observation of semiconductor devices, as well as in surface-shape observation of wafer surfaces.

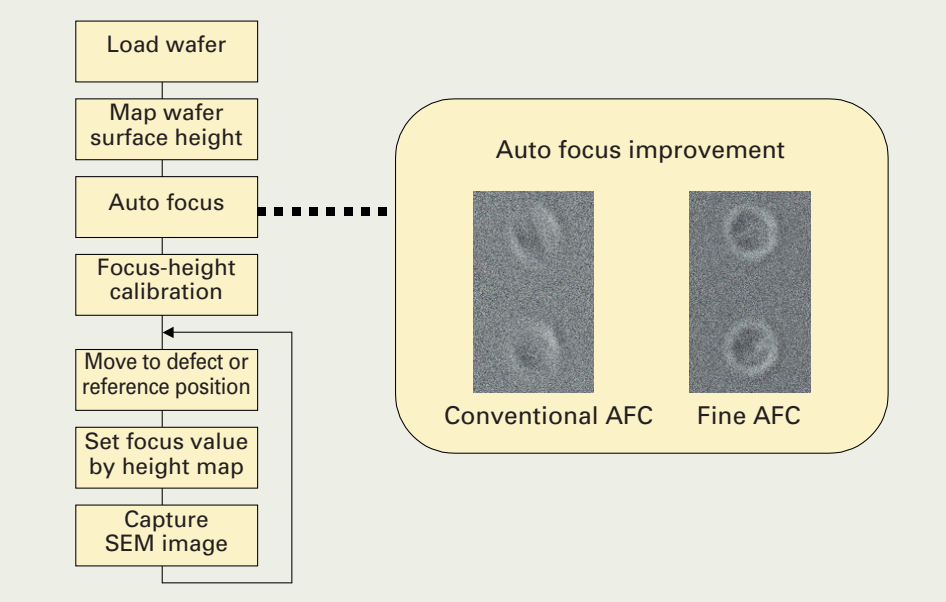

Fig. 6. Improvement of automatic functions.

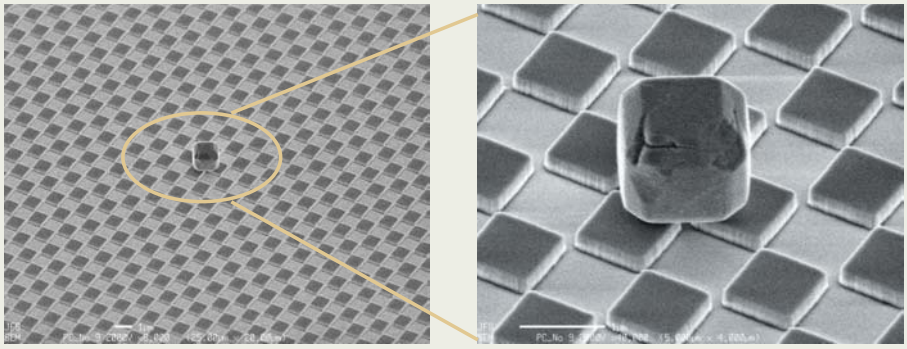

Tilt angle: 45°

Fig. 7. Tilt ADR.

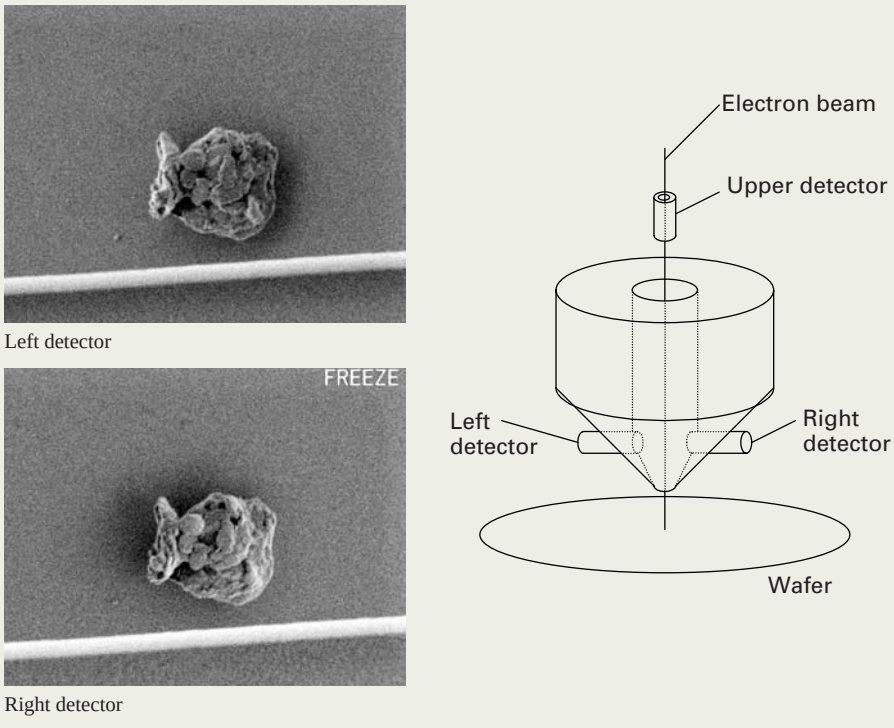

Fig. 8. Multiple detection system (multiple detectors).

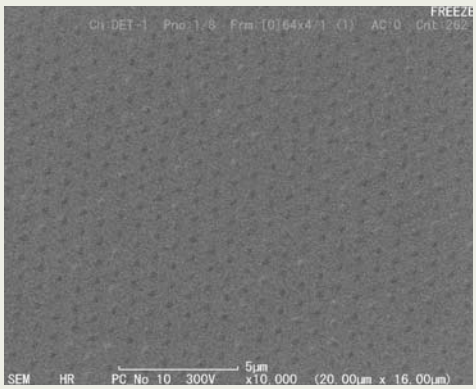

(a) Image obtained using the left detector.

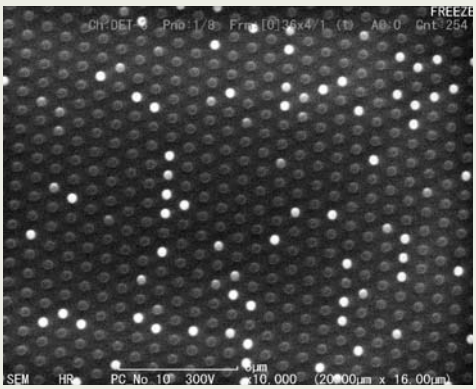

(b) Image obtained using the upper detector.

Fig. 9. Voltage-contrast images taken with the JWS-3000.

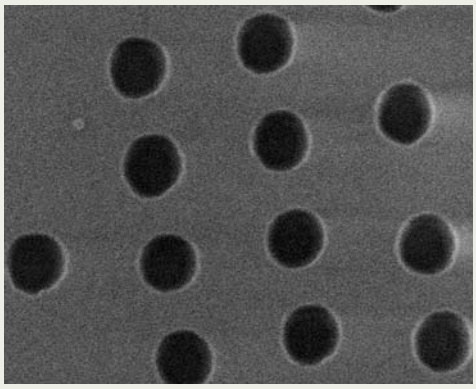

(a) Image obtained using the left detector.

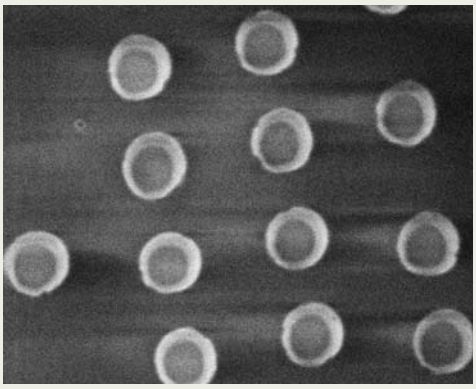

(b) Image obtained using the upper detector.

Fig. 10. Images of the bottoms of contact holes taken with the JWS-3000.

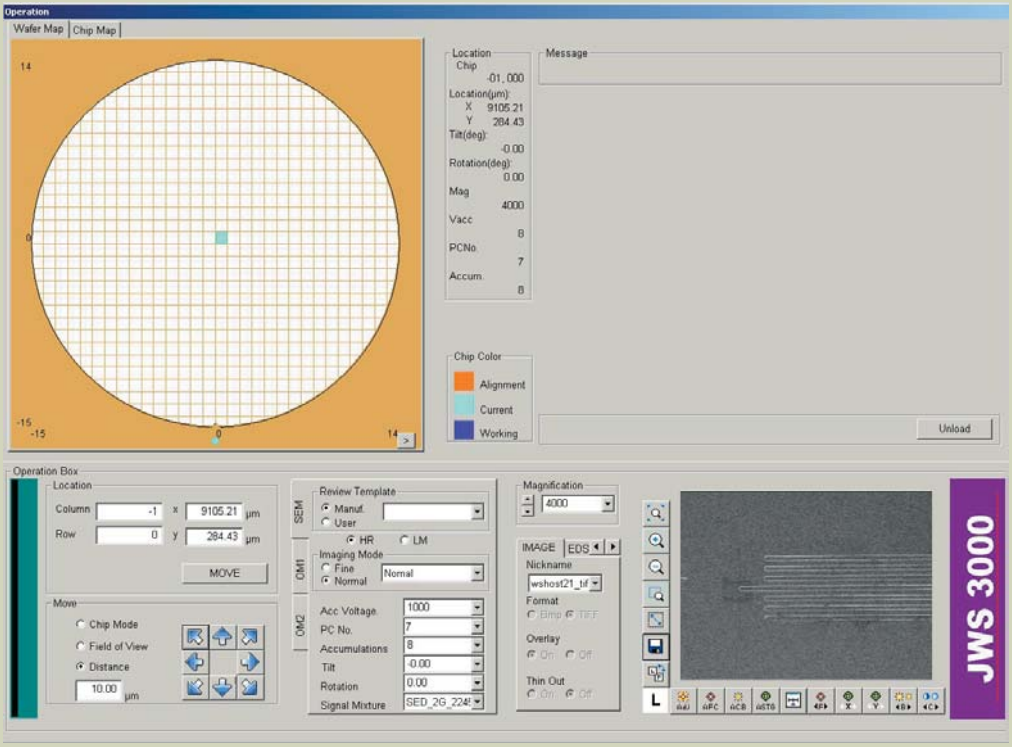

Fig. 11. New graphical user interface.

Application and Extension of Pickup Method to Various Materials

Toshiaki Suzuki, Noriaki Endo, Eiji Okunishi and Toshiko Kuba

Application & Research Center, JEOL Ltd.

Introduction

The pickup method [1] is widely utilized as a means of preparing TEM specimens by using the FIB (Focused Ion Beam) instrument. This method traps only a thin-filmed portion of the specimen with the tip of a glass probe by using an optical microscope with a manipulator, and places it on a supporting film. Therefore, unlike other methods such as the dicing method [2], this method requires no pre-treatment. Moreover, several thin-film specimens can be mounted on a TEM grid with a supporting film. From these reasons, this method is found to be very efficient in both preparing and observing specimens. The pickup method is now utilized mainly for semiconductor devices, and also it can be applied to other specimens. We confirmed that even a thin-film specimen with different electric property from each other (such as metal, semiconductor or insulator) can be trapped on the tip of a glass probe, and that it is possible to place a thin-film specimen on a support other than the commonly used collodion film. We report here the procedure for preparing a thin-film specimen using the pickup method, some examples of application of the various supports, and its application to TEM tomography.

Procedure for Making Thin-film Specimen by Pickup Method

Making of a thin-film specimen by the pick-up method consists of three steps: (1) Preparing a glass probe, (2) Fabricating and separating a thin film by FIB, and (3) Picking up the thin film. We explain these processes in sequence below.

(1) Preparing a glass probe

The pickup system consists of a micro-pipette puller (**Fig. 1**) and a micro-forge (**Fig. 2**) which are used to process a glass probe, and an optical microscope with a manipulator (**Fig. 3**). To use the pickup method, one needs to prepare a glass probe beforehand. The glass probe is made by heating, pulling and cutting the center of a glass rod (**Fig. 4**). After that, the tip of the glass probe is heated by the heater of a micro-forge in order to increase the surface area of the probe tip and thus increase the contact area with the thin film (**Fig. 5**). The glass probe manufactured by this process is inserted in the holder and mounted in the manipulator of the optical microscope.

(2) Fabricating and separating a thin film by FIB

The surface of the bulk specimen is processed according to the normal procedure to fabricate a thin film. When the film has reached a thickness of about 1 μm, the stage is inclined by 60° and the specimen is subjected to a cutting process (bottom cutting) to separate the thin film at the bottom of the thin film part (**Fig. 6**). After that, the normal thin film processing continues until the specimen reaches a thickness of less than 0.1 μm. At that time, both edges of the thin film part are cut (side cutting) (**Fig. 7**), and completely separated from the bulk specimen (**Fig. 8**) as the last step in the processing.

(3) Picking up thin film

The specimen, after being taken out of the specimen chamber of the FIB, is placed on the stage of the optical microscope with a manipulator (**Fig. 9 left**). When the tip of the glass probe touches the specimen at the separated thin film part (**Fig. 9 middle**) as a result of manipulation of the X, Y and Z axes of the glass probe using the hydraulic handle, the thin film part is trapped. The trapped thin film part is transferred to and mounted on the support-

Fig. 1. Micro-pipette puller.
Apparatus to make a probe by heating and cutting a glass rod.

Fig. 2. Micro-forge.
Apparatus for heating the probe tip and enlarging the surface area.

Fig. 3. Optical microscope with manipulator.
Left: Overall picture of optical microscope with manipulator.
Right: Enlarged picture of manipulator.

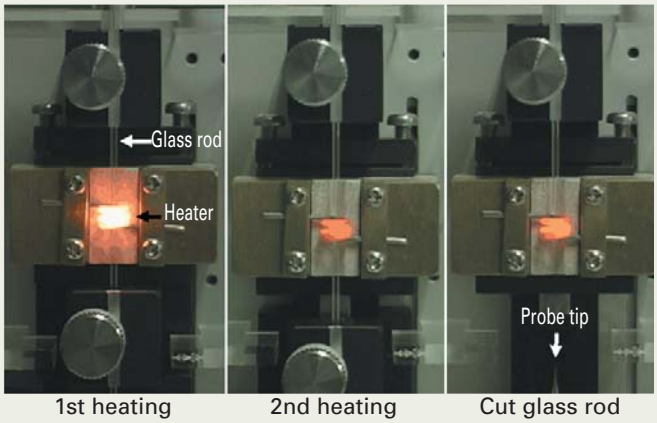

Fig. 4 . Preparation of probe 1.
Probe is made by heating and cutting a glass rod using the micro-pipette puller.
Heating is carried out in two stages, and a sharper tip is made.

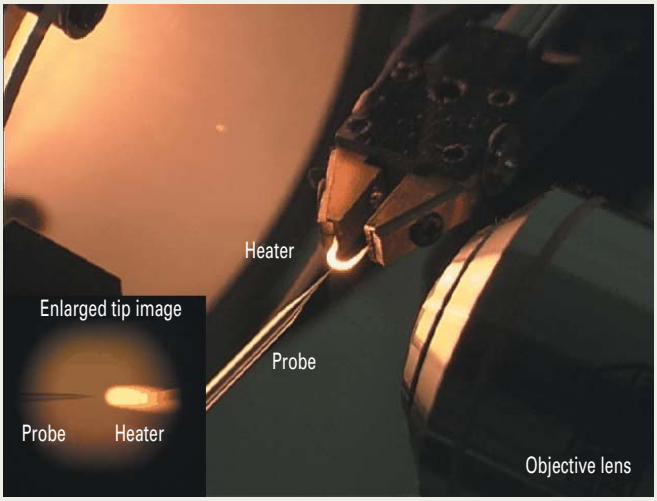

Fig. 5. Preparation of probe 2.
The probe tip is heated and the surface area is increased by micro-forge.
At the lower left is an enlarged picture of the tip.

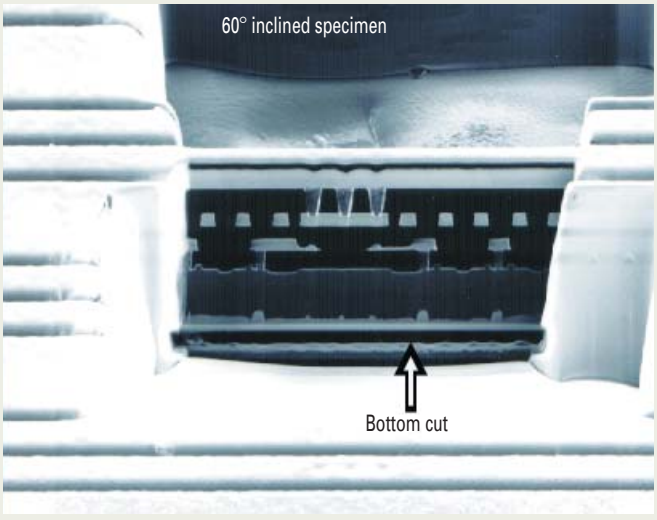

Fig. 6. Fabrication of thin film by FIB and separation 1.
After thinning film to about 1 μ m, tilt it 60° and bottom-cut it off from the bottom of the thin film.

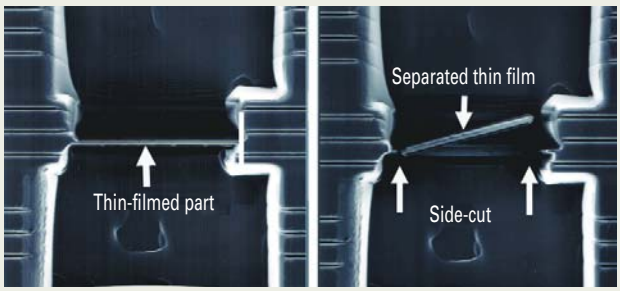

Fig. 7. Fabrication of thin film by FIB and separation 2.
After thinning film to 0.1 μm (Left), side-cut both sides of the thin film to separate it.

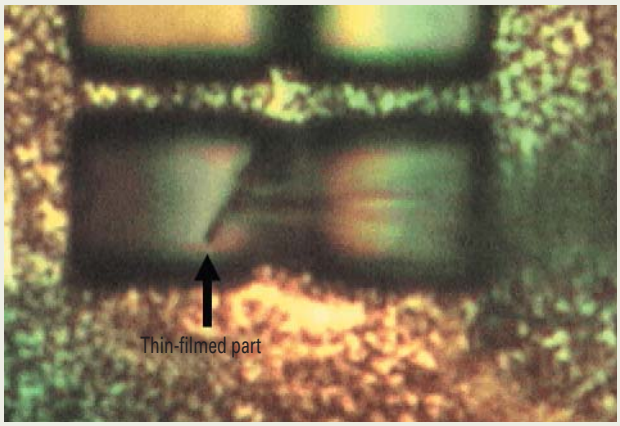

Fig. 8. Pickup 1.
Manipulate the hydraulic handle, approach the probe tip and touch it.

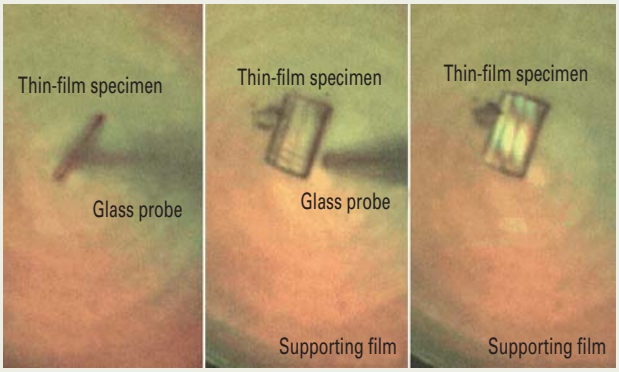

Fig. 9. Pickup 2.
Transfer the specimen (left), which is trapped on the glass probe, to the supporting film and mounted on it (middle). The glass probe is retracted to a safe position (right).

ing film (**Fig. 9 right**). After that, the TEM observation is conducted.

Application of Pickup Method to Various Materials

Every material has its own characteristic physical properties such as conductivity. The reason why the thin film specimen is trapped on the tip of the glass probe is generally believed to be electrostatic force. On account of this, some specimens might be difficult to trap depending on the material. Therefore, we must apply this method to various materials, which have their own physical properties, into thin films and check whether the glass probe traps them. On this occasion, we selected thin films from three electrically different types of materials, metal, semiconductor and insulator, and carried out experiments to determine what kinds of thin films are trapped by the tip of the glass probe after FIB processing. We also conducted experiments to determine whether the thin film can be mounted on the supporting film when we changed the kind of the supporting film. Furthermore, we tried experiments to determine whether the TEM observation and element mapping are possible. The combinations of the specimen and supporting film used in the experiments are shown in **Table 1**. We prepared ① Nickel and gold film plated on a copper plate and ② Gold and cadmium alloy as the metallic materials, ③ Device I (CCD) and ④ Device II (tungsten plug) as the semiconductor materials, and ⑤ Wiring on glass plate (inorganic material) and ⑥ Polymer blend (organic material) as the insulators.

As a result, we have found that every specimen from ① to ⑥ can be trapped at the tip of the glass probe. Namely, we have found from these experiments that the electrical property of the material does not affect its capability of being trapped. We have found in particular that even specimen ⑤, is a glass plate, which is almost the same material as the glass probe, can be trapped. Although it is generally believed that the specimen trapping by the glass probe is caused by static electricity, we can surmise [3] that the thin film is trapped by a cause other than static electricity, because even the same material as the tip can be trapped; however, we must carry out more detailed verification to prove this. Furthermore, collodion is generally used for the supporting film, but in the present experiment, we could mount the thin-film specimens on even supporting films made of materials other than collodion. We could also carry out the TEM observation and element mapping with prolonged irradiation of the specimen without any problem, and doing so did not cause any changes such as breaking the supporting film during observation (**Figs. 10** to **20**). The holey carbon film in particular enables us to obtain a clear high-resolution image by observing the portion of the thin film on the hole. It has been already reported that a specimen can be mounted not only on the supporting film, but also on the bulk substrate (such as graphite and silicon single crystal). This shows that the pickup method is also applicable to the scanning electron microscope, electron-probe micro analyzer and Auger analyzer in addition to TEM, and that by utilizing this technique, reprocessing by

Table 1. Combinations of the specimen and type of supporting film.

Electrical property of specimen	Specimen name	Type of supporting film
Metallic material	① Nickel and gold film plated on copper plate	Holey carbon film*
	② Gold and cadmium alloy	Micro plastic grid
Semiconductor material	③ Device I (CCD)	Holey carbon film*
	④ Device II (Tungsten plug)	Carbon film
Insulator		
Inorganic material	⑤ Wiring on glass plate	Holey carbon film*
Organic material	⑥ Polymer blend	Carbon film

* Made by Quantifoil Co. http://www. quantifoil.com

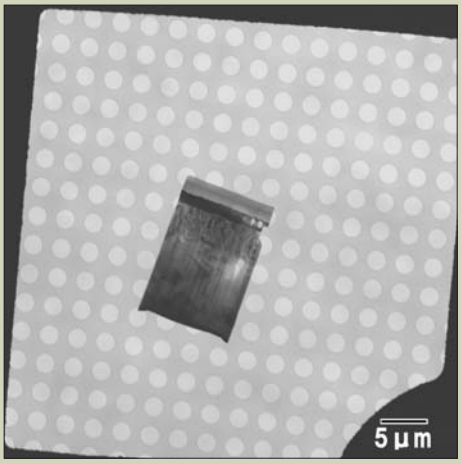

Fig. 10. Thin-film specimen ① mounted on the holey carbon film (TEM image).
(Nickel and gold film plated on copper plate: metal material)

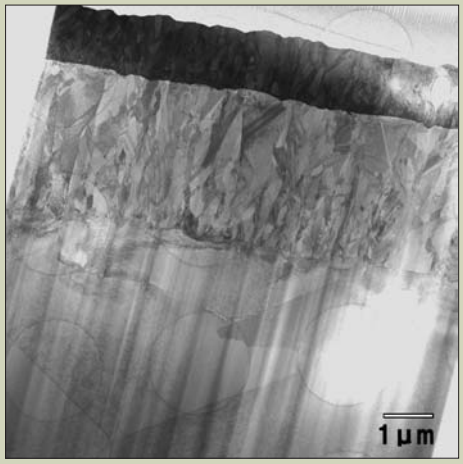

Fig. 11. Thin-film specimen ① mounted on the holey carbon film (enlarged TEM image).
(Nickel and gold film plated on copper plate: metal materials)

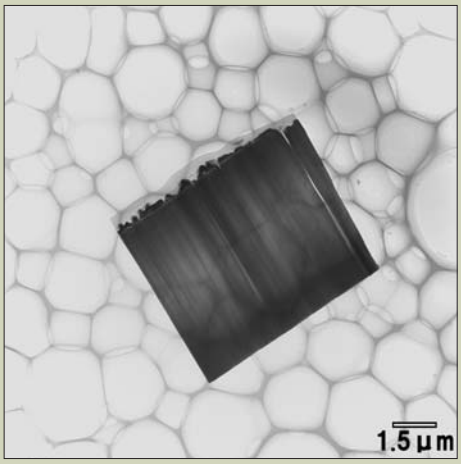

Fig. 12. Thin-film specimen ② mounted on a micro plastic grid (TEM image).
(Gold and cadmium alloy: metal material)

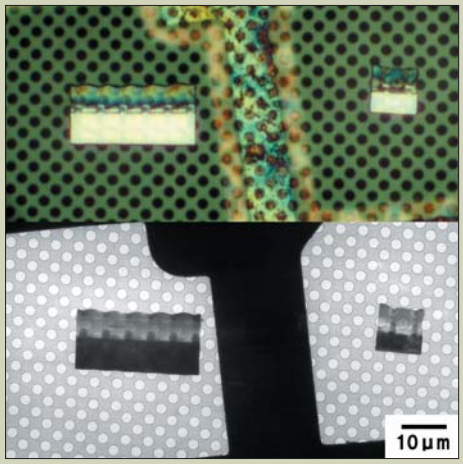

Fig. 13. Thin-film specimen ③ mounted on the holey carbon film.
(Top: Optical microscope image, Bottom: TEM image)
(Device I : semiconductor material)

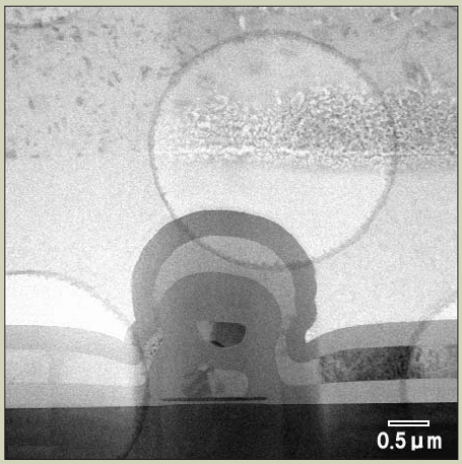

Fig. 14. Thin-film specimen ③ mounted on the holey carbon film (STEM bright-field image).
(Device I : semiconductor material)

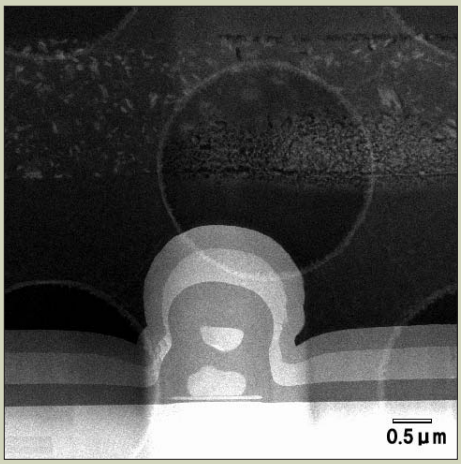

Fig. 15. Thin-film specimen ③ mounted on the holey carbon film (STEM dark-field image).
(Device I : semiconductor material)

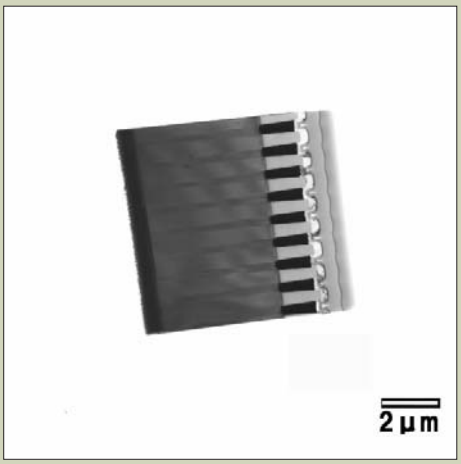

Fig. 17. Thin-film specimen ④ mounted on a carbon film (TEM image).
(Device II : semiconductor material)

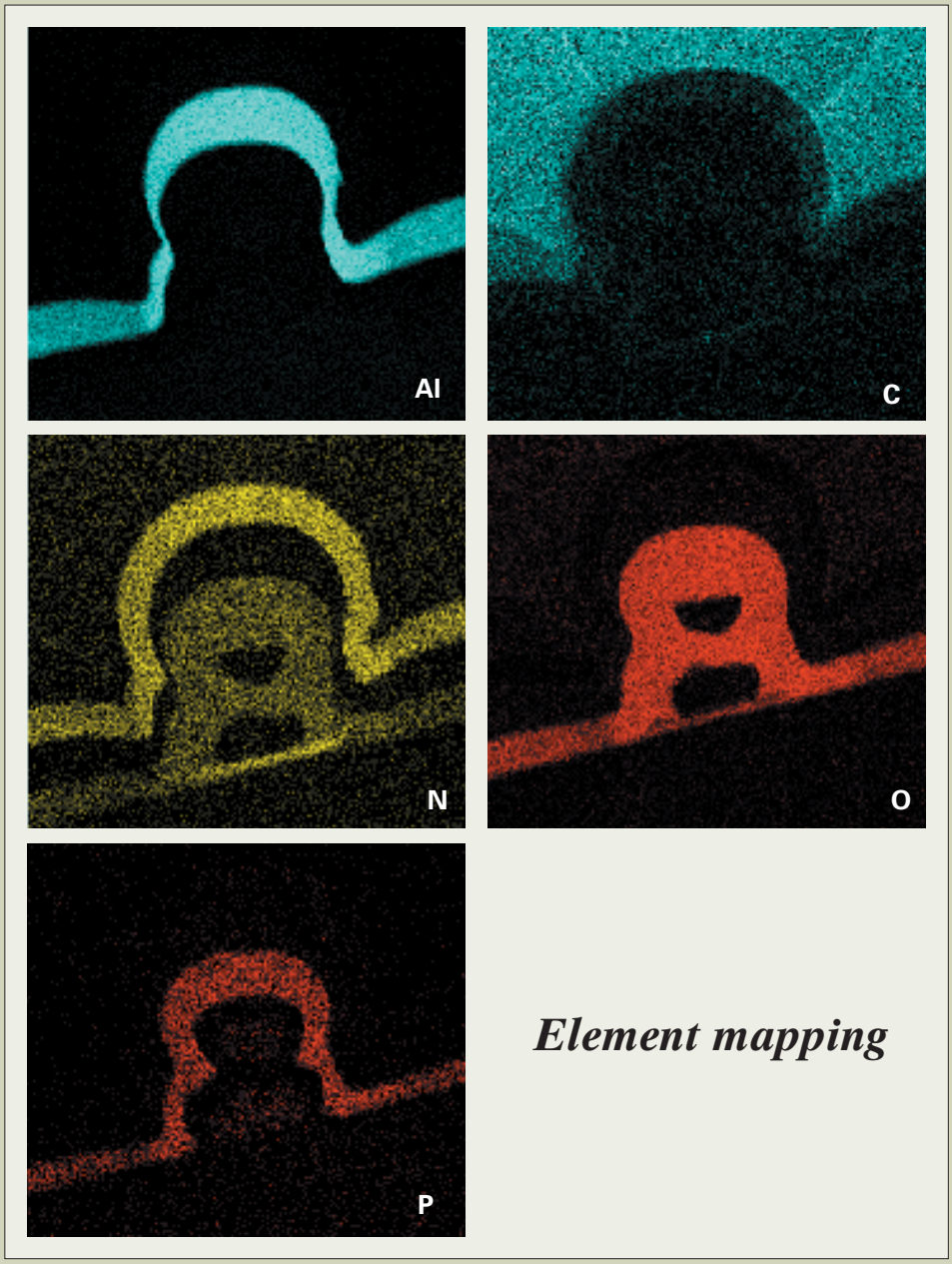

Fig. 16. Thin-film specimen ③ mounted on the holey carbon film (Element mapping).
(Device I : semiconductor material)

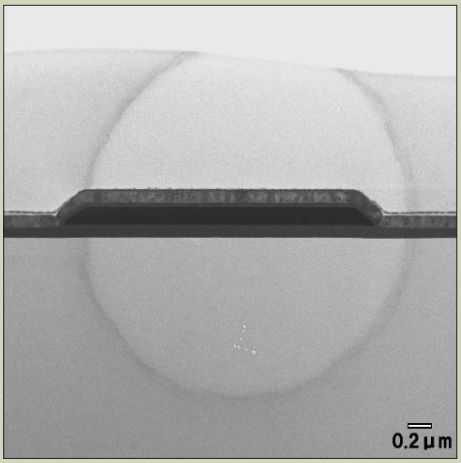

Fig. 18. Thin-film specimen ⑤ mounted on the holey carbon film (STEM bright-field image).
(Wiring on glass: inorganic insulator material)

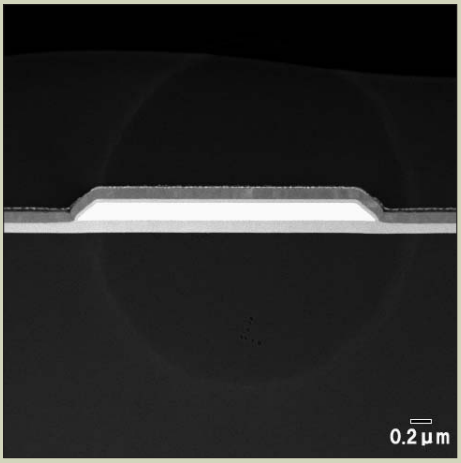

Fig. 19. Thin-film specimen ⑤ mounted on the holey carbon film (STEM dark-field image).
(Wiring on glass: inorganic insulator material)

using an FIB is possible [4]. Even for an insulator specimen, Auger analysis in which a conductive coating cannot be applied, is an extremely effective method [5] by mounting the thin-filmed specimen on conductive substrate, because the greater part of the electron beam can pass through the specimen giving the least effects on electrical charging of the specimen.

Application to TEM Tomography

TEM tomography [6] using the principle of CT (computerized tomography) can obtain the high-precision reconstructed image by acquiring greater information over as large an angle as possible. Recently, demand for the three-dimensional structure analysis of semiconductor devices is increasing. The fabrication of the specimen by using the FIB, which is capable of pinpoint processing, is expected; however, the dicing method cannot provide the information over such a large angle due to the geometrical structure of prepared specimen. On the other hand, the pickup method can provide the information over a large angle without blocked by the obstacle, because only the thin-filmed specimen is mounted on the supporting film. **Figure 21** shows one of a series of STEM images of the DRAM prepared by using the pickup method, and 3D reconstructed images obtained from the STEM images are shown in **Fig. 22**.

Conclusions

The pickup method can be applied to the wide range of materials. It enables high-throughput specimen processing, because it requires no pre-processing, and multiple thin film specimens can be mounted on a TEM grid with a supporting film. It also enables obtaining a clearer high-resolution image by using the holey carbon film as a supporting film. Moreover, the specimen can be mounted not only on the supporting film but also on the bulk substrate. As a result, it can also be applied to thin-film reprocessing and analysis using the Auger analyzer, electron probe micro analyzer, or scanning electron microscope other than TEM. It is especially effective for Auger analysis, in which a conductive coating using such as sputtering cannot be applied, even for insulating specimen. We can also expect to apply the method to TEM tomography because the specimen is not concealed by obstacles even tilting it through a high angle.

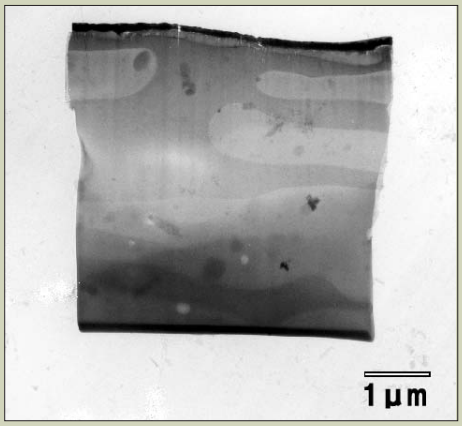

Fig. 20. Thin-film specimen ⑥ mounted on a carbon film (STEM bright-field image).
(Polymer blend: organic insulator material)

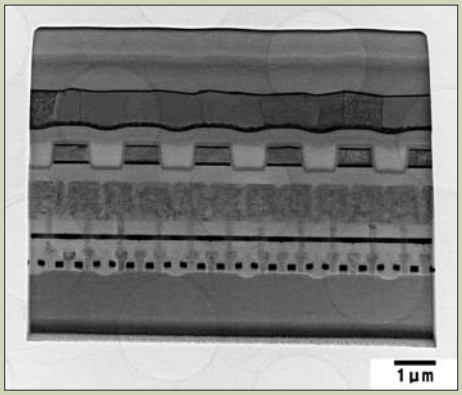

Fig. 21. STEM image of DRAM prepared by pickup method.

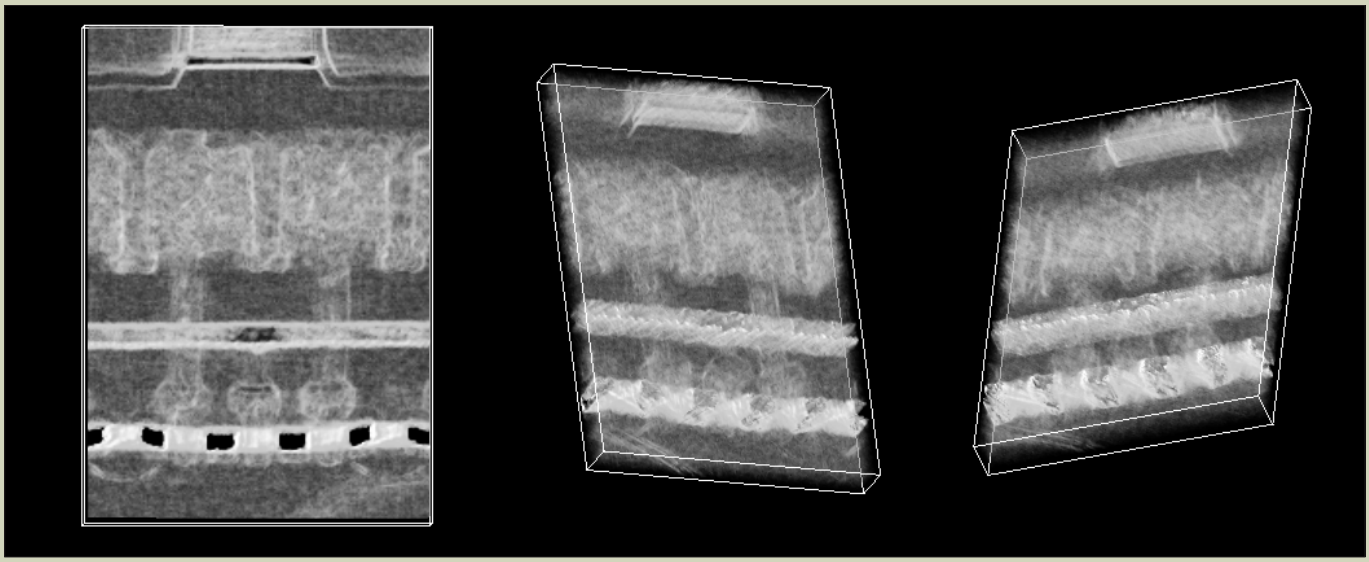

Fig. 22. 3D reconstructed image of device (Specimen: DRAM). This is obtained from a series of STEM images of the thin film picked up as shown in Fig. 21.

References

1. M. M. H. F. Overwijk, F. C. vanden Heuvel and C.W. Bulle-Lienwma: *J. Vac. Sci. Techno. B*, **11** (6), Nov/Dec, 2021 (1993).
2. Y. Yabuuchi: *Proceedings of the 9th Symposium on Analytical Electron Microscopy* (in Japanese) p. 44 (1993).
3. N. Teii: *Seidenki no ABC, BLUE BACKS series of Kodansha Pub. Co.* (in Japanese), p. 20.
4. T. Kuba: *Proceedings of the 59th Annual Meeting of the Japan Microscopy Society* (in Japanese) p. 105 (2003).
5. K. Tsutsumi, T. Suzuki and Y. Nagasawa.: *JEOL News*, **36E**, No.1, 66 (2001).
6. H. Furukawa et al.: *JEOL News*, **36E**, No.1, 50 (2001).

Introduction of New Products

Field Emission Electron Microscope
JEM-2200FS

The JEM-2200FS is a new energy filter TEM that is optimally configured for analytical functions, since it combines a 200 kV field-emission gun (FEG) and an in-column energy filter.
The JEM-2200FS also uses a new, rotation-free image-forming optical system, which not only facilitates acquisition of TEM images and diffraction patterns, but also produces stable spectra obtained using an energy analyzer.
This high-end energy filter TEM offers many new solutions for a wide range of applications.
Also, a 300 kV field-emission electron microscope JEM-3200FS is available.

- New in-column energy filter TEM
- High-brightness, high-stability FEG
- Full digital system for simple integrated operation
- Extensive functions for image processing and computer analysis

Field Emission Scanning Electron Microscope
JSM-7000F

The JSM-7000F has been developed to meet the needs for characterization of nano-structures. A fine electron probe at low electron energy is ideal for this purpose. Furthermore, a high probe current with a fine probe diameter is preferred for efficient characterization of nano-structures. The electron optical system developed for the JSM-7000F is equipped with the unique in-lens Field Emission Electron Gun (FEG) and aperture angle optimizing lens to meet this requirement. The objective lens, which does not form a magnetic field around the specimen, is guaranteed to give 3 nm resolution at 1 kV and 1.2 nm at 30 kV. The maximum probe current is 200 nA, which is sufficient for utilization of the high-sensitivity WDS at its top efficiency. The Schottky thermal FEG ensures high precision for prolonged analysis with its highly stable electron probe current. The large specimen chamber, which can be equipped with a great variety of detectors including EBSD, EDS, WDS, cathodoluminescence, and EBIC with their optimum geometries, is optimized for the characterization of nano-structures.

Introduction of New Products

Field Emission Auger Microprobe
JAMP-9500F

JEOL has introduced the JAMP-9500F Field Emission Auger Microprobe, featuring the world's highest spatial resolution. JEOL's newly developed electron optical system has greatly improved spatial resolution, making it possible for the JAMP-9500F to achieve the minimum probe diameter of 3 nm (for resolution of secondary-electron image (SEI)) and 8 nm (for Auger analysis).
In addition, the JAMP-9500F uses a hemispherical electrostatic energy analyzer (HSA) with a multi-channel detector, which has been optimized for Auger analysis. This HSA offers high energy-resolution analysis with high sensitivity, demonstrating its full effectiveness in chemical-state analysis.
The JAMP-9500F allows surface-shape observation using high-resolution SEI, Auger-image analysis at high magnifications and line-profile analysis. What's more, this instrument can perform depth-profile analysis while employing ion etching at the same time. Moreover, employment of a new neutralizing gun makes Auger analysis of insulating materials possible. The specimen stage can accommodate a large sample (up to 95 mm in diameter), enabling the JAMP-9500F to analyze any specimens while giving the instrument a nanometer-area analysis capability (several tens of nm in diameter).

Field Emission Electron Probe Microanalyzer
JXA-8500F

The JXA-8500F is a high-brightness, high-performance field emission electron probe microanalyzer that features a newly developed FE electron gun, electron-optics system and vacuum system. The FE electron gun has successfully attained an amazingly small electron probe, thus achieving, at low accelerating voltages and over a wide range of probe current, submicron-level analytical resolution and high-sensitivity X-ray detection.

Detectable element range	$_{5}$B to $_{92}$U ($_{4}$Be to $_{92}$U*[1])
Detectable wavelength range	0.087 to 9.3 nm
Number of WDSs	1 to 5 selectable (full scanner type)
Maximum specimen size	100 mm×100 mm×50 mm (thick)*[2]
Analyzable area	90 mm×90 mm*[2]
Maximum specimen-stage drive speed	15 mm/s*[2]
Accelerating voltage	1 to 30 kV (0.1 kV steps)

*[1] This range is available only when the optional analyzing element for beryllium is installed.
*[2] The value depends on what specimen stage you select.

Introduction of New Products

High Resolution Review SEM
JWS-3000

The JWS-3000 is a high resolution wafer inspection system for a 300 mm diameter wafer, which can be used effectively in CIM/FA. It is a high-throughput wafer visual inspection system provided with a eccentric goniometer stage by which the entire wafer surface, tilted up to 45°, can be observed. A high resolution image can be obtained even under a lower accelerating voltage than in conventional cases.
The system can communicate with a factory computer, and can access an automatic-transfer cart and read in material-recognition codes automatically, based on the SEMI standards. By networking (using Ethernet) with various kinds of defect/dust-particle inspection systems, on-line operation with various inspection systems can be realized.

- Wafer size: 300 mm diameter
- Image resolution: 3 nm (at 1 kV accelerating voltage in retarding mode ON)
- Tilt observation: <45 deg.
- Low energy observation: 100 V for Low-k Material
- High throughput ADR
  D-D: 750 DPH over 90%
  Array : 900 DPH over 90%
- Auto defect analysis for Bare Wafer (Tilt EDS)
- VC observation
- HAR contact Hall observation

Element Analyzer
JSX-3202EV

The JSX-3202EV, an element analyzer for environmental analysis, is ideal for detecting materials specified in two EU (European Union) regulations on environmental contaminants, such as WEEE (waste electrical and electronic equipment) and RoHS (restrictions on hazardous substances). This analyzer can detect specific harmful substances such as cadmium (Cd), lead (Pb), mercury (Hg) and chrome (Cr), which are contained in packing materials and pigments, and also hazardous materials like arsenic (As), down to a level of several ppm. The JSX-3202EV realizes a sensitivity of 5 ppm in analyzing a trace of cadmium (Cd) contained in plastic material, and achieves a lower detection limit of 2 ppm for standard specimens (value obtained from actual measurement by JEOL).

- Minute traces of elements such as Cd, Pb, Hg and Cr can be analyzed all at once.
- New optical system (patent applied for) lets you analyze elements with high sensitivity and low background in a short time.
  - ☐Only 10 seconds for 40 ppm Cd specimen, and 2 minutes for 10 ppm Cd specimen
  - ☐Sb, Pb, Br can be analyzed with high sensitivity and low background.
  - ☐One wire can be analyzed as a sample.

Introduction of New Products

Bench Top GCQMS
JMS-K9

The JMS-K9 Bench Top GCQMS is a high-sensitivity GC/MS system with the latest computer technology. It consists of a gas chromatograph (GC) with capillary column, a basic QMS (Quadrupole Mass Spectrometer), a data system and a printer. The system includes the following for stable GC/MS data with high-sensitivity and simple operations:

- An automatic tuning function for the ion source and analyzer of the QMS.
- A plug-in prefilter and postfilter for the analyzer of the QMS.
- TMP (turbo-molecular pump) for the QMS's vacuum system for clean vacuum in the analyzer.

Mass range	*m/z* 1.5 to 1022
Resolution	More than 2000 (FWHM) at *m/z* 614
Ionization voltage	30 to 200 V (variable at 1 V step)
Sensitivity	
EI (Scan mode) (rms)	1 pg octafluoronapthalene *m/z*272, *S/N*>90
EI (SIM mode) (rms)	0.1 pg octafluoronapthalene *m/z*272, *S/N*>120
P-CI* (Scan mode)	100 pg benzophenone *m/z*183, *S/N*>100
N-CI* (Scan mode)	10 pg hexachlorobenzene *m/z*284, *S/N*>200
Dynamic range	1.6×10^7

*options

High Resolution Mass Spectrometer MStation
JMS-800D

A high-end mass spectrometer system for dioxin analysis. Equipped with a new socket ion source, an automatic lock-mass ON/OFF reservoir, and a photo multiplier detector, it achieves high throughput. It also incorporates a complete set of precision-management supporting tools such as the Diok and the special-data search system.

- Resolution
  60,000 (10 % valley)
- Sensitivity
  2, 3, 7, 8-TCDD 30 fg *S/N*>30
  (6 channels, 100 msec./ch, Resolution 10000)
- Accelerating voltage
  up to 10 kV

M&M 2003

The meeting this year was organized by members of the Microscopy Society of America (61st annual meeting), the Inter-American Committee of Societies for Electron Microscopy (7th Biennial Meeting), the Microbeam Analysis Society (37th Annual Meeting), and the International Metallographic Society (36th Annual Meeting). More than 1400 hundred attendees enjoyed a rich program focused on instrumentation and applications in numerous fields of materials and biological science. Approximately 100 vendors (and approximately 1000 vendor representatives) specializing in instruments, accessories, software, specimen preparation, microscopy services, and a host of other microscopy related products, were also in attendance.

There were a number of notable symposia and a few "firsts" for a meeting of this type. This was the first meeting where the submission of papers was 100% digital and the first time since the last proceedings where only invited papers were published in hard copy format, all other abstracts published on CD only. Again, the premier Journal of numerous Microscopy societies, Microscopy and Microanalysis, lead the publishing effort.

The Symposia from this years meeting can tell us something about the future of electron microscopy, a subject of great interest to JEOL and to the readers of the JEOL News. JEOL instruments figure largely in many of the symposia in Materials and the Life Sciences. With an eye on the future, of special interest were Symposia in Microscopy of Nanomaterials, Tomography, Advances in High Resolution Imaging, and Focused Ion Beam.

There were 92 papers (about 10% of the total) in the symposium titled "Electron Microscopy of Nanomaterials". There is no question that Nanoscience has long required electron microscopy for the nano-characterization and nano-imaging of nano-scale features, even before the advent of Nano-technology. That a symposium would have 92 entries is without precedent at the M&M and shows the level of research funding and scientific interest that is presently focused on the nano world. Perhaps we should refer to our societies as Nanoscopy Societies and our tools as Electron Nanoscopes. The wide range of JEOL instrumentation available for nanoscale research is without parallel in the industry. JEOL instruments include a complete performance range of TEMs, SEMs, Auger Microscopes, Electron Microprobes and SPM's.

Since nanotechnology deals with a variety of materials types including biological and bioactive materials, the convergence of biology and materials science has clearly been assisted by the growth in interest in nanotechnology. The overlap is especially obvious in the field of tomography. Previously the realm of the biologist, tomography is now of great interest in the field of materials nanotechnology, especially in the elucidation of 3 dimensional structure of particle agglomerations, nanotube and nano-structure composites, and a variety of other "nano" manufactured entities. In the symposium "Electron Tomography: Recent Advances and Applications", 18 researchers discussed the state-of-the-art in reconstruction, acquisition, and real-world examples.

The search for ever better understanding of the materials, both hard and soft, leads to improvements in both imaging and analytical resolution. When Ruska proposed the electron microscope in the early 1930's, he was told that the electron microscope would never work, primarily because the spherical aberration of electron lenses was believed to be insurmountably large. Fortunately he ignored his detractors, but it is true that spherical aberration has been one of the major factors limiting the resolution of the electron microscope. Today there are correctors available that can eliminate the degrading effects of spherical aberration. These correctors are separately available for both the TEM and STEM. The symposium entitled "Advances in High Resolution Imaging" was almost entirely devoted to the subject of aberration correction. Though correctors have been available for over 5 years, the application to problems in materials and biological science is still in its infancy. JEOL has active joint programs with CEOS GmbH for TEM and STEM Cs correction. STEM and TEM correctors are being provided to Oxford University, Lehigh University, Oak Ridge National Labs, Brookhaven National Lab, and Hitachi Global Storage Technologies. Other companies with published interest in these corrector types include LEO and Nion.

Spherical Aberration correction is not limited to the transmission microscope. JEOL announced a new scanning microscope with Cs and Cc corrector, the JSM-7700. This instrument will be optimized for 5 kV performance and is expected to provide 0.6 nm resolution at 5 kV. Using the GB mode, we expect 0.7 nm at 1 kV.

There are two maxims of microscopy—if you look you're bound to see something, and not everything you see will be artifact. The major challenge of microscopy has always been specimen preparation…preserving the structure that you want to see and study in the microscope while preparing the sample. The introduction of artifact is always and underlying problem. The rapid increase in Focused Ion Beam (FIB) instrumentation is directly in response to the need to prepare samples in a controlled way, control not only of precise location but also precise control of preparation variables. JEOL introduced the JEM-9310 FIB to the US market to meet this market requirement. This low cost, high performance instrument offers TEM and SEM specimen preparation stages and a variety of etching gases and coating materials. JEOL also announced the sale and support of the Seiko FIB product line for manual or automated TEM specimen preparation. Both the JEOL and Seiko instruments are being sold in conjunction with the new STEM/TEM from JEOL, the JEM-2500SE, an extremely high performance, easy to use instrument for industrial or university applications.

The M&M meeting is one of the premier annual microscope meetings in the world. JEOL is proud to be a part of the microscopy community and will continue to supply the most advanced, state-of-the-art instruments to the scientific community. JEOL is committed to the entire instrument experience providing not only the best hardware and software but also the complete support required to keep the instruments operating at their peak specifications.

Thank you for being part of the JEOL family of users.

Reported by Dr. M Kersker, JEOL USA, INC.

JEOL Ltd. 1-2 Musashino 3-chome Akishima Tokyo 196-8558 Japan Sales Division ☎(042)528-3381 FAX(042)528-3386

http://www.jeol.co.jp/

ARGENTINA
COASIN S. A. C. I. yF.
Virrey del Pino 4071,
1430 Buenos Aires, Argentina
Telephone: 54-11-4552-3185
Facsimile: 54-11-4555-3321

AUSTRALIA & NEW ZEALAND
JEOL (AUSTRALASIA) Pty. Ltd.
Unit 9, 750-752 Pittwater Road,
Brookvale, N. S. W. 2100, Australia
Telephone: 61-2-9905-8255
Facsimile: 61-2-9905-8286

AUSTRIA
LABCO GmbH
Dr.-Tritremmel-Gasse 8,
A-3013 Pressbaum, Austria
Telephone: 43-2233-53838
Facsimile: 43-2233-53176

BANGLADESH
A.Q. CHOWDHURY & CO. Pvt. Ltd.
Baridhara Central Plaza 87, Suhrawardy Avenue
2nd Floor Baridhara,
Dhaka-12129 Bangradesh
Telephone: 880-2-9862272, 9894583
Facsimile: 880-2-988070

BELGIUM
JEOL (EUROPE) B. V.
Zaventem/Ikaros Business Park,
Ikaroslaan 7A, B-1930 Zaventem, Belgium
Telephone: 32-2-720-0560
Facsimile: 32-2-720-6134

BRAZIL
FUGIWARA ENTERPRISES
INSTRUMENTOS CIENTIFICOS LTDA.
Avenida Itaberaba,3563
02739-000 Sao Paulo, SPl Brazil
Telephone: 55-11-3983-8144
Facsimile: 55-11-3983-8140

CANADA
JEOL CANADA, INC.
(Represented by Soquelec, Ltd.)
5757 Cavendish Boulevard, Suite 540,
Montreal, Quebec H4W 2W8, Canada
Telephone: 1-514-482-6427
Facsimile: 1-514-482-1929

CHILE
TECSIS LTDA.
Avenida Holanda 1248,
Casilla 50/9 Correo 9, Providencia, Santiago, Chile
Telephone: 56-2-205-1313
Facsimile: 56-2-225-0759

CHINA
JEOL LTD., BEIJING OFFICE
Room No. B2101/2106,
Vantone New World Plaza,
No. 2 Fuwai Street, Xicheng District,
Beijing 100037, P. R. China
Telephone: 86-10-6804-6321/6322/6323
Facsimile: 86-10-6804-6324

JEOL LTD., SHANGHAI OFFICE
Sanhe Building 11F2, Yan Ping Road,
No. 121,Shanghai 200042, P.R. China
Telephone: 86-21-6246-2353
Facsimile: 86-21-6246-2836

JEOL LTD., GUANG ZHOU OFFICE
(South Power) World Trade Center Building
371-375, Huang Shi East-Road, Guang Zhou,
510095, P, R. China
Telephone: 86-20-8778-7848
Facsimile: 86-20-8778-4268

CYPRUS
MESLO LTD.
Scientific & Laboraty Division,
P. O. Box 27709, Nicosia Cyprus
Telephone: 357-2-666070
Facsimile: 357-2-660355

EGYPT
JEOL SERVICE BUREAU
3rd Fl. Nile Center Bldg.,
Nawal Street, Dokki, (Cairo), Egypt
Telephone: 20-2-335-7220
Facsimile: 20-2-338-4186

FRANCE
JEOL (EUROPE) S. A.
Espace Claude Monet,
1, Allee de Giverny 78290
Croissy-sur-Seine, France
Telephone: 33-13015-3737
Facsimile: 33-13015-3747

GERMANY
JEOL(GERMANY)GmbH
Oskar-Von-Miller-Strasse 1,
85386 Eching Germany
Telephone: 49-8165-77346
Facsimile: 49-8165-77512

GREAT BRITAIN & IRELAND
JEOL (U.K.) LTD.
JEOL House, Silver court, Watchmead, Welwyn
Garden City, Herts AL7 1LT., England
Telephone: 44-1707-377117
Facsimile: 44-1707-373254

GREECE
N. ASTERIADIS S. A.
56-58, S. Trikoupi Str. P.O.Box 26140
GR-10022 Athens, Greece
Telephone: 30-1-823-5383
Facsimile: 30-1-823-9567

HONG KONG
FARMING LTD.
Unit 1009, 10/F., MLC Millennia Plaza
663 King's Road, North Point, Hong Kong
Telephone: 852-2815-7299
Facsimile: 852-2581-4635

INDIA
Blue Star LTD. (HQ)
Analytical Instruments Department,
'Sahas'414/2 Veer Savarkar Marg,
Prabhadery Mumbai 400 025, India
Telephone: 91-22-5666-4065
Facsimile: 91-22-5666-4001

Blue Star LTD. (New Delhi)
Analytical Instruments Department,
E-44/12 Okhla Industrial Area,
Phase-11, New Delhi 110 020, India
Telephone: 91-11-5143-4000
Facsimile: 91-11-5149-4004

Blue Star LTD. (Calcutta)
Analytical Instruments Department,
7, Hare Street Calcutta 700 001, India
Telephone: 91-33-2248-0131
Facsimile: 91-33-2248-1599

Blue Star LTD. (Chennai)
Analytical Instruments Department, Lakshmi
Neela Rite Choice Chambers, 5, Bazullah Road,
3rd Floor T. Nagar Chennai 600 017, India
Telephone: 91-44-2815-8846
Facsimile: 91-44-2815-8015

INDONESIA
PT. TEKNOLABindo PENTA PERKASA
J1. Gading BukitRaya,
Komplek Gading Bukit Indah Blok I/11,
Kelapa Gading Jakarta 14240, Indonesia
Telephone: 62-21-45847057/58/59
Facsimile: 62-21)-45842729

IRAN
IMACO LTD.
No. 141 Felestin Ave.,
P. O. Box 13145-537, Tehran, Iran
Telephone: 98-21-6402191/6404148
Facsimile: 98-21-8978164

ITALY
JEOL (ITALIA) S.p.A.
Centro Direzionale Green Office Via Dei Tulipani,
1, 20090 Pieve, Emanuele (MI), Italy
Telephone: 39-2-9041431
Facsimile: 39-2-90414353

KOREA
JEOL KOREA LTD.
Sunmin Bldg. 6th F1.,218-16, Nonhyun-Dong,
Kangnam-Ku, Seoul, 135-010, Korea
Telephone: 82-2-511-5501
Facsimile: 82-2-511-2635

KUWAIT
YUSUF I. AL-GHANIM & CO. (YIACO)
P. O. Box 435, 13005 - Safat, Kuwait
Telephone: 965-4832600/4814358
Facsimile: 965-4844954/4833612

MALAYSIA
JEOL (MALAYSIA) SDN. BHD. (359011-M)
205, Block A, Mezzanine Floor,
Kelana Business Center97,
Jalan SS 7/2, Kelana Jaya,
47301 Petaling Jaya, Selangor, Malaysia
Telephone: 60-3-7492-7722
Facsimile: 60-3-7492-7723

MEXICO
JEOL DE MEXICO S.A. DE C.V.
Av. Amsterdam #46 DEPS. 402
Col. Hipodromo, 06100 Mexico D.F. Mexico
Telephone: 52-5-55-211-4511
Facsimile: 52-5-55-211-0720

PAKISTAN
ANALYTICAL MEASURING SYSTEM (PVT) LTD.
(AMS LTD.)
F-8/1-5, KDA Scheme No. 1,
Main Tipu Sultan Road,
P. O. Box 10604, Karachi-75350, Pakistan
Telephone: 92-21-4525185/4525186
Facsimile: 92-21-4525187/4536406

PANAMA
PROMED S.A.
Parque Industrial Costa del Este
Urbanizacion Costa del Este
Apartado 6281, Panama, Panama
Telephone: 507-269-0044
Facsimile: 507-263-5622

PHILIPPINES
PHILAB INDUSTRIES INC.
7487 Bagtikan Street, SAV Makati, 1203 Metro,
Manila Philippines
Telephone: 63-2-896-7218
Facsimile: 63-2-897-7732

PORTUGAL
LABOMETER-SOC TECNICA DE
EQUIPAMENTO DE LABORATARIO. LDA.
Rua Duque de Palmela, 30-1°,
G, 1200 Lisboa, Portugal
Telephone: 351-1-351-0180
Facsimile: 351-1-352-5066

SAUDI ARABIA
ABDULREHMAN ALGOSAIBI G. T.B.
Algosaibi Bldg., Airport Rd., P. O. Box 215,
Riyadh 11411, Saudi Arabia
Telephone: 966-1-479-3000
Facsimile: 966-1-477-1374

SCANDINAVIA
JEOL (SKANDINAVISKA) A.B.
Hammarbacken 6 A, Box 716
191 27 Sollentuna, Sweden
Telephone: 46-8-28-2800
Facsimile: 46-8-29-1647

SERVICE & INFORMATION OFFICE
JEOL NORWAY
Ole Deviks vei 28, N-0614 Oslo, Norway
Telephone: 47-2-2-64-7930
Facsimile: 47-2-2-65-0619

JEOL FINLAND
Ylakaupinkuja 2, FIN-02360 Espoo, Finland
Telephone: 358-9-8129-0350
Facsimile: 358-9-8129-0351

JEOL DENMARK
Naverland 2, DK-2600 Glostrup, Denmak
Telephone: 45-4345-3434
Facsimile: 45-4345-3433

SINGAPORE
JEOL ASIA PTE. LTD.
29 International Business Park,
#04-02A Acer Building,
Tower B Singapore 609923
Telephone: 65-6565-9989
Facsimile: 65-6565-7552

SOUTH AFRICA
ADI Scientific (Pty) Ltd.
109 Blandford Road, North Riding,Randburg
(PO box 71295 Bryanston 2021)
Republic of South Africa
Telephone: 27-11-462-1363
Facsimile: 27-11-462-1466

SPAIN
IZASA. S.A.
Aragoneses, 13,
28100 Alcobendas,
(Polígono Industrial) Madrid, Spain
Telephone: 34-91-663-0500
Facsimile: 34-91-663-0545

SWITZERLAND
JEOL(GERMANY)GmbH
Oskar-Von-Miller Strasse 1,
85386 Eching Germany
Telephone: 49-8165-77346
Facsimile: 49-8165-77512

TAIWAN
JIE DONG CO., LTD.
7F, 112, Chung Hsiao East Road, Section 1, Taipei,
Taiwan 10023, Republic of China
Telephone: 886-2-2395-2978
Facsimile: 886-2-2322-4655

JEOL TAIWAN SEMICONDUCTORS LTD.
11F, No. 346, Pei-Ta Road, Hsin-Chu City 300,
Taiwan Republic of China
Telephone: 886-3-523-8490
Facsimile: 886-2-523-8503

THAILAND
BECTHAI BANGKOK EQUIPMENT
& CHEMICAL CO., Ltd.
300 Phaholyothin Rd. Phayathai,
Bangkok 10400, Thailand
Telephone: 66-2-615-2929
Facsimile: 66-2-615-2350/2351

THE NETHERLANDS
JEOL (EUROPE) B.V.
Tupolevlaan 28-A, 1119 NZ Schiphol-Rijk,
The Netherlands
Telephone: 31-20-6533088
Facsimile: 31-20-6531328

TURKEY
TEKSER KOLL. STI.
Acibadem Cad. Erdem Sok, Baver Art, N° 6/1,
81010, Uskudar, Istanbul, Turkey
Telephone: 90-216-3274041
Facsimile: 90-216-3274046

UAE
BUSINESS COMMUNICATIONS LLC.
P. O. Box 2534, Abu Dhabi UAE
Telephone: 971-2-6348495
Facsimile: 971-2-6316465

USA
JEOL USA, INC.
11 Dearborn Road, Peabody, MA. 01960, U. S. A.
Telephone: 1-978-535-5900
Facsimile: 1-978-536-2205/2206

JEO USA, INC. WEST OFFICE
5653 Stoneridge Drive Suite
#110 Pleasanton, CA. 94588 U. S. A.
Tel: 1-925-737-1740
Fax: 1-925-737-1749

VENEZUELA
MITSUBISHI VENEZOLANA C. A.
Avenida Francisco de Mirande Los Palos Grandes,
Carecas, Venezuela
Telephone: 58-212-209-7402
Facsimile: 58-212-209-7496

(Ser. No. 120)

No. 01501K314C Printed in Japan, Kp